Clay minerals and continental-scale remagnetisation: a case study of South American Neoproterozoic carbonates

Ualisson Donardelli Bellon[1,2], Ricardo Ivan Ferreira Trindade[1], Wyn Williams[2], Douglas Galante[3], Lucy Gomes Sant'Anna[4], Thales Pescarini[1]

[1]University of São Paulo, Institute of Astronomy, Geophysics and Atmospheric Sciences (IAG), Department of Geophysics, São Paulo, 05360020, Brazil
[2]University of Edinburgh, School of Geosciences, Edinburgh, EH9 3FE, Scotland
[3]University of São Paulo, Institute of Geosciences, Department of Sedimentary and Environmental Geology, São Paulo, 05508080, Brazil
[4]Institute of Energy and Environment (IEE), São Paulo, 05508010, Brazil

Key Points:

- Remagnetised Neoproteorozoic carbonates of South America may not consistently display anomalous hysteresis parameters
- Synchrotron-based analysis revealed pseudo-single domain-sized magnetite spatially correlated with aluminosilicates (smectite-illite)
- The Late Cambrian Gondwana assembly thermally reset remanence in these carbonates, which was finally blocked during a sequential cooling

Corresponding author: Ualisson Donardelli Bellon, ualisson.bellon@usp.br

Corresponding author: Wyn Williams, wyn.williams@ed.ac.uk

Abstract

Carbonate rocks frequently undergo remagnetisation events, which can partially/completely erase their primary detrital remanence and introduce a secondary component through thermoviscous and/or chemical processes. Despite belonging to different basins hundreds of kilometres apart, the Neoproterozoic carbonate rocks of South America (over the Amazon and São Francisco cratons) exhibit a statistically indistinguishable single-polarity characteristic direction carried by monoclinic pyrrhotite and magnetite, with paleomagnetic poles far from an expected detrital remanence. We use a combination of classical rock magnetic properties and micro-to-nanoscale imaging/chemical analysis using synchrotron radiation to examine thin sections of these remagnetised carbonate rocks. Magnetic data shows that most of our samples failed to present anomalous hysteresis properties, usually referred to as part of the "fingerprints" of carbonate remagnetisation. Combining scanning electron microscopy-energy-dispersive X-ray spectroscopy (SEM-EDS), highly sensitive X-ray fluorescence (XRF), and X-ray absorption spectroscopy (XAS) revealed the presence of subhedral/anhedral magnetite, or spherical grains with a core-shell structure of magnetite surrounded by maghemite. These grains are within the pseudo-single domain size range (as well as most of the iron sulphides) and spatially associated with potassium-bearing aluminium silicates. Although fluid percolation and organic matter maturation might play an important role, smectite-illitisation seems a crucial factor controlling the growth of these phases. X-ray diffraction analysis identifies these silicates as predominantly highly crystalline illite, suggesting exposure to epizone temperatures. Therefore, we suggest that the remanence of these rocks should have been thermally reset during the final Gondwana assembly, and locked in a successive cooling event during the Early-Middle Ordovician.

Plain Language Summary

Carbonate rocks serve as important records of ancient climates and host magnetic minerals capable of documenting the evolution of Earth's magnetic field. Nevertheless, their initial magnetisation, acquired during sedimentation, is frequently supplanted by a secondary magnetisation, originating from various geological processes altering local thermochemical stability. For carbonate rocks, this remagnetisation process is often associated with a "magnetic fingerprint". In South America, carbonate rocks from different sedimentary basins (hundreds of kilometres apart) exhibit statistically similar magnetic components that deviate from their formation origin, indicating secondary processes. This multidisciplinary study integrates classic paleomagnetic analysis with micro-chemical and imaging analysis to comprehend the geological phenomena responsible for remagnetising such an extensive continental area. We demonstrate that not all remagnetised samples display the anticipated magnetic fingerprint. Highly detailed chemical analysis confirms the presence of nanoscopic magnetic minerals spatially correlated with clay minerals indicating that while organic matter transformation may play a significant role, clay mineral transformation is a key phenomenon governing remagnetisation in these rocks. However, our data also supports the notion that these rocks underwent heating during the final assembly of the ancient continental landmass, Gondwana, and a sequential cool-down event is suggested as locking their magnetisation in the state observed today.

1 Introduction

The natural remanent magnetisation (NRM) carried by magnetic minerals depends on the geological processes that result in rock formation and preservation, as well as the Earth's geomagnetic field intensity and direction (Butler, 1992). Because the magnetic mineralogy of carbonate rocks is influenced by the redox state (Pourbaix, 1974) and the chemical composition of seawater and pore water, valuable insights into the Earth's paleoenvironmental conditions can be acquired from them (Evans & Heller, 2003; Liu et al., 2012; Roberts et al., 2013). Carbonate sedimentation, including those primarily sourced from marine organisms (Grotzinger & James, 2000), allows for the correlation of paleomagnetic information in carbonate deposits with significant geological events that influenced the evolution of life (Trindade et al., 2003; Trindade & Macouin, 2007; Golovanova et al., 2023). However, the search for the primary detrital remanence of carbonate rocks often encounters single-polarity components that do not align with the corresponding age of the unit (R. D. Elmore et al., 2012). This secondary component may originate from numerous geological processes that occur below the Curie temperature (Jackson & Swanson-Hysell, 2012) of natural ferromagnetic phases and may alter the original remanence of carbonate rocks. For instance, any phenomenon able to change the preservation conditions of a rock might have the potential to cause alterations that lead to the acquisition of secondary components. We call remagnetisation the process of substituting a primary remanence with a secondary one (partially or entirely).

Remagnetisation might occur due to thermal or chemical phenomena. Thermal activation will partially (or entirely) overwrite a remanence by simply achieving the relaxation time of a population of grains at a given temperature. On the other hand, any transformation of a magnetic mineral below its Curie temperature may cause the development of a chemical remanent magnetisation (CRM) (Dunlop & Özdemir, 1997; Levi, 2007). CRMs might be approached and segmented into two subdivisions (Tauxe et al., 2018): grain growth remanent magnetisation (g-CRM), and oxidation and further reordering of magnetic moments, said to be acquiring an alteration chemical remanence (a-CRM). When nucleating from nanometric grain ranges, authigenic particles will experience a change in their thermal relaxation properties as they go from superparamagnetic (SP) to single-domain (SD) magnetic structures, yielding stable remanence records of the geomagnetic field (Dunlop & Özdemir, 1997). Depending on the local conditions, specific morphologies will arise and constrain the magnetic anisotropy properties of the particles.

Carbonate rocks make one of the most favourable examples of natural materials to study CRMs, because particular magnetic properties often arise in these rocks, resulting in what is usually called "magnetic fingerprints" of remagnetisation, observed in worldwide examples, such as (Jackson, 1990; Jackson & Swanson-Hysell, 2012; R. D. Elmore et al., 2012) single polarity components; an outstanding contribution of superparamagnetic particles; abnormal magnetic hysteresis ratios; and contradictory domain-state tests. Chemical remagnetisation of carbonate rocks might occur due to two main geological processes: sediment burial and fluid migration. During sediment burial, early diagenetic processes are strongly controlled by the redox conditions and the cellular respiration processes of microorganisms in the sedimentary column (Roberts, 2015), which might use iron oxides/hydroxides in the metabolic process together with organic matter (also causing reduction of ferric ions). Late diagenetic processes, such as clay-mineral transformations, release ions in the medium (including ferrous ions) that under the appropriate kinetic/thermodynamic conditions might lead to the growth of authigenic ferromagnetic phases (Hirt et al., 1993; Woods et al., 2002; Tohver et al., 2008). Fluid transport through the natural porosity of sedimentary rocks can induce mineral transformation, while hot basinal brines and hydrothermal associated with nearby magmatic activity/orogenies may trigger the dissolution of detrital phases and growth of others (McCabe et al., 1983; Miller & Kent, 1988; McCabe & Elmore, 1989; Jackson, 1990; Stamatakos et al., 1996; D'Agrella-Filho et al., 2000; Davidson et al., 2000; Trindade et al., 2004; Huang et al., 2017; Jiao et al., 2019; Dannemann et al., 2022; Xu et al., 2022). Finally, the maturation of organic matter and biodegradation of hydrocarbon in sedimentary basins might produce acidic solutions and disturb the local thermochemical equilibrium also contributing to the formation of new magnetic phases (Font et al., 2006; Aldana et al., 2011; Emmerton et al., 2013).

While we have identified various processes associated with remagnetisation, connecting these phenomena becomes a challenging endeavour, especially when observing remagnetisation on a continental scale. The Neoproterozoic cap carbonates of South America present a fascinating puzzle, as they span different geological basins (see Figure 1a), separated by vast distances and encompassing diverse cratonic regions. Remarkably, these regions exhibit a singular-polarity characteristic component, yielding almost identical paleomagnetic features (see Figure 1b). Previous studies (e.g., (D'Agrella-Filho et al., 2000; Trindade et al., 2004; Font et al., 2006)) have highlighted the magnetic similarities in these rocks, aligning with the anticipated fingerprints of chemical remagnetisation. Despite numerous proposed mechanisms to explain remanence resetting in these basins, the mystery persists regarding how specific geological events targeted these rocks across West Gondwana, resulting in such coherent and tightly clustered paleomagnetic directions. This paper embarks on a multidisciplinary study of these remagnetised carbonate rocks. Our approach combines bulk macroscopic measurements of their magnetic properties with synchrotron-based microscopic chemical and imaging analyses, aiming to understand the spatial relationships of remanence-bearing grains with surrounding minerals (especially clay minerals). Additionally, we revisit the magnetic signatures, questioning the reliability of the commonly invoked "fingerprints of remagnetisation."

Our primary objective is to establish a correlation between the observed magnetic properties in these rocks, the processes leading to chemical remanence acquisition, and the geological events responsible for inducing such transformations in West Gondwana. Through this exploration, we aim to shed light on the intricate connections between magnetic phenomena and the dynamic geological history of the region.

2 Geological setting and previous studies

Remagnetised carbonates are found throughout the whole of South America, extending from the Amazon craton towards the São Francisco-Congo craton (Font et al., 2012). We select three targets over three different basins for our study (Figure 2). Over the São Francisco craton (Figure 2a), we have sampled the cap carbonates of the Sete Lagoas Formation (Bambuí group, São Francisco basin) as well as the carbonates of the Salitre Formation (Irecê Basin). Although within the same craton, these formations are separated by hundreds of kilometres. The third target comprehends the carbonates of the Araras group, which extends through both an undeformed region of the Amazon craton (Figure 2b), but also over the deformed terrain of the Paraguay belt. The two formations studied here are the cap carbonates of the Mirassol d'Oeste Formation and an overlying unit, the Guia Formation (Figure 2e). In the following section, we summarise the geological setting of these units and discuss the results of previous studies.

2.1 The São Francisco and Irecê basins

The rocks of the Neoproterozoic São Francisco Basin (Figure 2a) can be divided into two groups: the Macaúbas at the base and the Bambuí, overlying it (Dardenne, 1978). The Bambuí Group includes a thick sequence of more than 1000 km of a siliciclastic carbonate succession in the southwest of the São Francisco Craton (Paula-Santos et al., 2015). Two large subgroups segment the Bambuí: a) a shallow basal marine stratum with two cycles of carbonate deposition and pelitic-psammitic sedimentation and; b) a superior alluvial stratum. Deformation in the Bambuí rocks progressively increases towards Neoproterozoic mobile belts (D'Agrella-Filho et al., 2000): the Brasília orogen on the east side and the Araçuaí orogen on the west side (Figure 2a), with two regions recognised as being free of deformation in the centre of the basin.

The age of the Bambuí has long been a matter of discussion. Early studies determined the maximum depositional ages of the Macaúbas as 900 Ma (Pedrosa-Soares et al., 2000). Direct dating ($^{207}Pb/^{206}Pb$) of the cap-carbonates from the lower portion of the Sete Lagoas Formation (the base of the Bambuí group) yielded ages of 740 $\mp$ 22 Ma (Babinski et al., 2007), interpreted as Sturtian cap carbonates. Later, rocks from the Sete Lagoas Formation were also dated by Rodrigues (2008): five grains from foliated argillaceous siltstones yielded ages around 610 Ma (U-Pb in zircon) and the youngest age found for a marble sample was

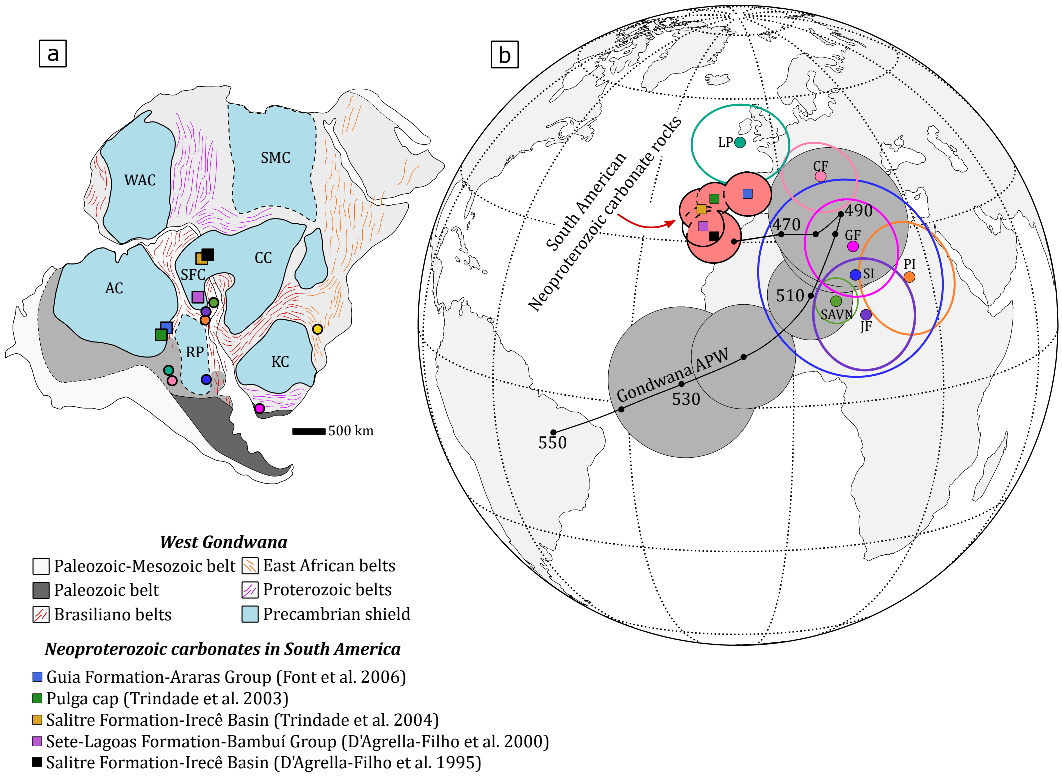

Figure 1. a) Tectonic context of the geological targets studied in this project. Spheres and squares show the geographic location of the palaeomagnetic poles from (b), modified from Alkmim et al. (2006). b) APW curve of West Gondwana considering South Africa in its current position (data from Torsvik (2012)), showing mean palaeomagnetic poles of millions of years old ages ($A95 < 20°$, grey circles). Poles represented by a sphere are Late Neoproterozoic/Early-Cambrian (check Table 1) and their respective $A95°$ interval, rotated to South Africa $(55.7°, -34.8°, 43.3°)$ when necessary. Squares are palaeomagnetic poles of remagnetised carbonates, centred at their $A95∘$ interval (pinkish). Confidence intervals of Neoproterozoic remagnetised poles from South America intersect themselves. AC: Amazon craton, WAC: West-African craton, CC: Congo Craton, SFC: São Francisco craton, RP: Rio dela Plata craton, KC: Kalahari craton, SMC: Sahara Meta craton.

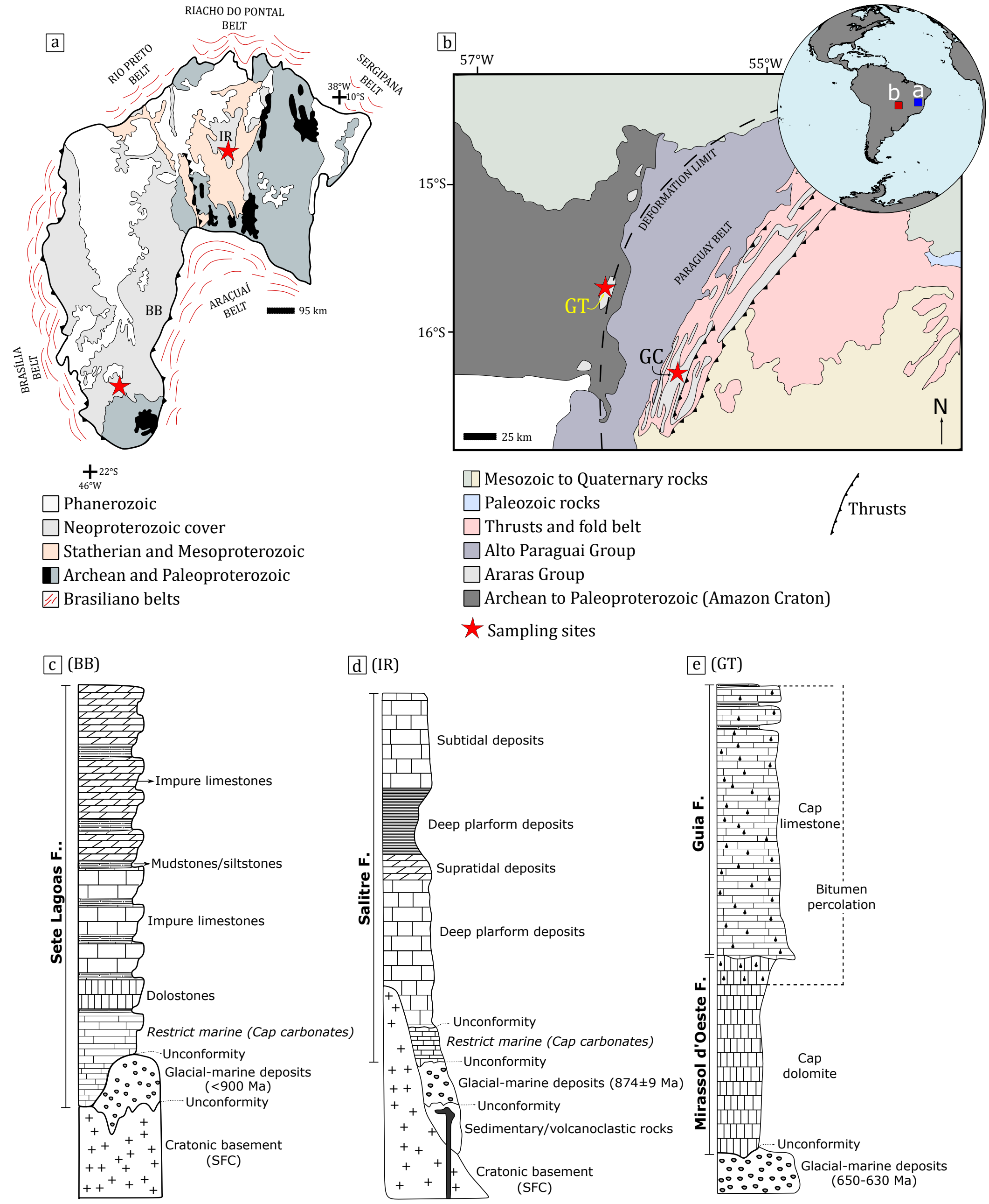

Figure 2. Simplified geological context of the studied units. a) São Francisco Craton, showing the basins of Irecê (BB) and São Francisco, where the Bambuí group lies (BB), surrounded by Neoproterozoic orogenies. Modified from Paula-Santos et al. (2015) b) Tectonic map of the southeast part of the Amazon Craton and the Paraguay belt, showing the distribution of the Araras Group in both terranes. Modified from Font et al. (2006) c, d, and e) are representative stratigraphic profiles of sections of the Bambuí, Irecê, and Araras group (over the Amazon Craton), modified from Guacaneme et al. (2017); Santana et al. (2021); Trindade et al. (2003).

609 Ma. More recently, Paula-Santos et al. (2015) provided new ages (U-Pb in zircon) for the Bambuí group. These authors reported maximum depositional ages, set by the youngest population of detrital grains, as 557 Ma, which would indicate that the uppermost portion of the Sete Lagoas Formation was not related to either the Sturtian or the Marinoan glacial events. D'Agrella-Filho et al. (2000) have performed a palaeomagnetic and Pb-isotopic study of the Sete Lagoas Formation, sampling rocks in what is said to be an undeformed area of the São Francisco basin. New experimental data of our work also belong to the base of the Sete Lagoas Formation. The authors reported that samples majorly showed features commonly associated with remagnetised carbonates, such as (i) wasp-waisted magnetic hysteresis, (ii) samples with abnormally high Bcr/Bc ratios, and (iii) contradictory Lowrie-Fuller and Cisowski tests. Lowrie tests in some samples indicated the presence of a hard component with blocking temperatures around 340°C and soft components with blocking temperatures around 500°C, associated with monoclinic pyrrhotite and magnetite (respectively). Like Paleozoic carbonates, spherical magnetite and other irregularly shaped magnetites were also reported, which were analysed through SEM-EDS data. Three major components were identified in their work (check their respective palaeomagnetic poles in Figure 1b): (i) a NW component (A) with negative inclination, yielding blocking temperatures between $150-275°$, (ii) a NE (B) component with positive inclination showing blocking temperatures between $300-400°$ and (iii) a third (C) component, similar to component B but showing higher blocking temperatures ($350-530°$). While component A was assumed to be the result of a thermoviscous component, B/C components were interpreted as the result of a more ancient geomagnetic field.

The age of B and C components was not believed to result from a depositional remanence, since their paleolatitudes were far from the environment of carbonate development (39-5°) (D'Agrella-Filho et al., 2000). Stable and reliable Pb/Pb ages (obtained from low-Pb and high-U samples, U/Pb¿1) from the undeformed area of the basin showed variable $^{207}Pb/^{206}Pb$ ages, one of the samples yielding a 520 ∓ 53 Ma age and $^{238}U/^{206}Pb$ age of 603 ∓ 80 Ma. Samples from the region affected by the orogenies also showed trustworthy Pb/Pb ages, but with much greater uncertainties, whereas $^{238}U/^{204}Pb$ x $^{206}Pb/^{204}Pb$ errochrons indicate a resetting of the isotopic system around 545 Ma. The authors use these data to suggest an extensive fluid percolation throughout the São Francisco Basin, which they interpreted to be constrained between 500-530 Ma by the palaeomagnetic poles calculated from the B/C components when these are compared with palaeomagnetic poles from the Gondwana APW (D'Agrella-Filho et al., 2000).

The Bebedouro and Salitre Formations are the equivalents of the Macaúbas and Bambuí in the Irecê basin, north of the Bambuí (in the São Francisco Craton, Figure 2a). The Bebedouro formation is a glacial/marine record that yields a wide range of ages for detrital zircons, the youngest around 875 Ma (Babinski et al., 2004; Figueiredo et al., 2009). The Salitre Formation comprises a carbonate deposit of a marine platform, with white dolostones and pink/red limestones rich in clay minerals, overlying diamictites and tillites. These carbonates have typical features of cap carbonates, such as columnar stromatolites (Misi & Kyle, 1994). Misi and Veizer (1998) suggested depositional ages around 600-670 Ma for preserved carbonate rocks of the Salitre Formation (derived from $^{87}Sr/^{86}Sr$ data compared with secular strontium isotopic curves of Neoproterozoic sea waters). More recently, Santana et al. (2021) reported that the maximum depositional age for deep ramp and subtidal to intertidal deposits of the Salitre Formation was around 670 Ma.

After previous studies of D'Agrella-Filho (1995), Trindade et al. (2004) performed geochronological (Pb-Pb) and palaeomagnetic studies in samples from the Salitre Formation. The samples from this work belong to the same formation as reported in their works. These rocks also showed the expected behaviour of remagnetised carbonate rocks. A similar multicomponent signature (to the Sete Lagoas samples) was also observed during the thermal demagnetisation of Salitre samples (Trindade et al., 2004). The calculated poles of component A (SaA) and component C (SaC) of the Salitre Formation are statistically indistin-

Table 1. Palaeomagnetic poles of remagnetised carbonates from South America, in comparison with other matching palaeomagnetic poles of similar age (same as in Figure 1. (p) – Primary magnetisation; (r) – remagnetisation; N – number of poles.

Source	Age (Ma)	PLAT	PLON	A95	Reference
BaC (r)	500-530?	30.2°	321.0°	3.8°	(D'Agrella-Filho et al., 2000)
SaC (r)	500-530?	33.0°	323.0°	4.0°	(Trindade et al., 2004)
Slt (r)	≈500?	27.5°	321.4°	4.9°	(D'Agrella-Filho, 1995)
GF (r)	≈520?	29.9°	332.6°	4.3°	(Font et al., 2006)
PcS (r)	≈520?	33.1°	326.6°	3.2°	(Trindade et al., 2003)
SAVN (p)	500	4.7°	333.2°	4.06°	(Temporim et al., 2021)
PI (r)	510-500	−0.8°	346.5°	10.2°	(D'Agrella-Filho & Pacca, 1986)
JF (r)	510-500	−0.6°	335.2°	10.0°	(D'Agrella-Filho et al., 2004)
SI (p)	≈520	5.9°	338.1°	18.1°	(Sánchez-Bettucci & Rapalini, 2002)
CF (p)	≈519	23.6°	346.5°	7.0°	(Franceschinis et al., 2019)
LP (p)	477-485	38.3°	340.4°	8.8°	(Piceda et al., 2018)
GF (p)	≈485	28.0°	14.0°	9.0°	(Bachtadse et al., 1987)

guishable from those from the same components (BaA and BaC) in the Bambuí formation (D'Agrella-Filho et al., 2000). Poles calculated with component B of both formations are also very close (although their confidence ellipses do not overlap, Figure 1b)). Regarding the isotopic dating, dark-grey carbonate samples of the middle-upper part of the Salitre Formation and stromatolite-bearing samples (cap carbonates) from a layer right above the diamictites of the Bebedouro formation were collected by Trindade et al. (2004) to perform Pb-Pb measurements. $^{207}Pb/^{206}Pb$ ages of the stromatolitic samples were calculated as 517 ∓ 27 Ma, but it decreases to 486 ∓ 28 Ma when considering all the Pb ratios together.

Since the samples of Salitre and Sete Lagoas are more than 600 km apart and show such similar palaeomagnetic and isotopic-Pb data, their main hypothesis of a remagnetisation throughout the carbonates of the São Francisco craton would be considering a percolation of basinal saline fluids around 520 Ma. Therefore, the magnetic remanence carried by B/C components of both basins would be carried by authigenic ferrimagnetic minerals that crystallised due to reactions triggered by the percolation of an orogenic fluid associated with the Brasiliano orogenies. Although the authors bring the discussion to highlight the trigger of remagnetisation in the carbonates of these basins, they do not argue about the actual mechanism related to the growth of the authigenic ferromagnetic grains (smectite-illitisation, biodegradation of hydrocarbon, and growth of ferrimagnetic phases, thermochemical oxidation, etc.), which is a role yet to be explored.

2.2 The Araras group

The Araras Group (Figure 2a) overlies the Puga Formation, a sequence of siltstones and diamictites sedimented in a glaciomarine environment (Alvarenga & Trompette, 1992). Post-glacial cap carbonates were followed by an extensive accumulation of bituminous lime mudstones and shales that represent deep platform deposits (Nogueira et al., 2003). The cap carbonates covering the Puga Formation are pinkish dolostones and cap cementstones (bituminous limestones with a high amount of terrigenous) (Trindade et al., 2003). Radiometric ages of the Araras Group are not available in the literature. Rocks of the Alto Paraguay Group (which includes mudstones, sandstones, and calcarenites) overlie the Araras Group, but their age is debatable (Rb-Sr, 569∓20 Ma) (Riccomini et al., 2007). Sedimentary rocks correlated to the rocks of the Araras Group are intruded, in the Paraguay belt, by a post-tectonic granite around 528 Ma (U-Pb in zircon) (Guimarães et al., 2017), which could mark a minimum depositional age. As discussed by (Nogueira & Riccomini, 2006), the presence of macrofossils (e.g. Cloudina, Gaucher et al. (2003)) in the Corumbá Group (which is toponomic related to the Araras Group) indicates a penecontemporary occurrence to the Ediacaran biota.

In the basal section of the Araras Group lies the dolomites of the Mirassol d'Oeste Formation and, overlying them, the limestones of the Guia Formation (Figure 2e). The Mirassol d'Oeste formation is composed of laminated pinkish-dolomitic mudstones with bioturbed structures, overlaid by greyish dolomites impregnated with hydrocarbon fluids and calcitic cementation (Font et al., 2006). The Guia Formation is composed of bituminous limestones associated with terrigenous grains. In the area over the Amazon Craton, the layers are sub-horizontal and undisturbed, while the area over the Paraguay Belt is intensely deformed. Trindade et al. (2003) performed palaeomagnetic studies on rocks from the Puga cap carbonates. From their studies, samples near the contact with the diamictites of the Puga Formation have shown a dual polarity component (A), that although similar to the current GAD yields high unblocking temperatures (ca. $520°C$) and positive reversal tests, indicating paleolatitudes around $22 + 6°$ and consequently suggesting its primary nature. Twenty meters above in the sedimentary column, after the transition with the Guia Formation, a single polarity component (B) with positive inclination steeply plunges to NE. Component B, when rotated from South America towards Africa plots near the Irecê and Bambuí poles (Figure 1b), which could indicate that these are also a result of a remagnetisation around the Middle-to-Late Cambrian. Samples from the Mirassol d'Oeste studied in this review, as a way of comparison with remagnetised units, belong to the basal stratum (the ones carrying detrital remanence) as well.

Font et al. (2005) further investigated the remanence carried by the dolostones of the Mirassol d'Oeste Formation. The response found in a new set of samples also showed a dual polarity behaviour that passed reversal tests, indicating a palaeolatitude of 22°. High unblocking temperatures/coercivities and IRMs (isothermal remanent magnetisation) that do not saturate up to 3 T indicated that haematite dominates magnetisation carried by Mirassol d'Oeste rocks studied in their work. In the work of Trindade et al. (2003), however, magnetite is clearly the main primary-remanence bearing mineral, which suggests that local heterogeneities in the sedimentary column with distinct sources should exist.

Although the upper section of the Mirassol d'Oeste has bitumen, the Guia Formation is the one where it strongly percolates. Font et al. (2006) have studied the carbonate rocks from the Guia Formation in two distinct terranes: in the Tercony Quarry at the Amazon Craton (where the outcrops lie undeformed) and in the Cáceres region at the Paraguay belt (where the samples are affected by the orogeny). Thermal demagnetisation of these samples resulted in a single polarity component that coherently matches other remagnetised Neoproterozoic rocks (Figure 1b). In samples from the Amazon craton, the component held by pyrrhotite is completely demagnetised around $320-360°C$, while a second step of decay occurs around $500°C$ in samples from the Cáceres region, indicating that magnetite and pyrrhotite yield the same direction. They reported a high contribution of SP particles in these samples, especially when compared with Mirassol d'Oeste samples. A higher amount of SP particles was also detected in the area affected by the Paraguay belt. Iron oxides and framboid structures enriched in sulphur were also spotted where bitumen is concentrated. This evidence was interpreted as the result of a growing chemical remanence, probably related to hydrocarbon maturation, leading to the formation of pyrrhotite. It is also suggested that smectite illitisation could be responsible for the presence of magnetite, a mechanism triggered by the folding of the part affected by the orogenic belt (Font et al., 2006). Nevertheless, this makes the Araras Group an interesting target for deeper studies on remagnetisation, since its base unit is not remagnetised while an upper unit is.

3 Methods

In our pursuit of comprehending the geological mechanisms responsible for remagnetizing basins dispersed over considerable distances, our objective is to conduct a meticulous and multidisciplinary investigation. If the magnetic properties of these rocks align with the anticipated magnetic fingerprints of remagnetised carbonates, we undertake a comprehensive analytical approach from macro to micro scales. In our methodological framework, depicted in Figure 3, we initiate the analysis by characterising the magnetic assemblages in our samples, sourced from locations previously explored in paleomagnetic studies (D'Agrella-Filho et al., 2000; Trindade et al., 2004; Font et al., 2006). Once we identify samples exhibiting the expected magnetic signatures of chemically remagnetised rocks, we progress to the compositional investigation.

We utilize X-ray diffractometry with a particular focus on clay content and conduct thermogravimetric analysis to refine our understanding of volatile components, including organic matter, within these rocks. Subsequently, with analytical findings in hand, we transition to a microscopic characterisation. This final phase involves the examination of thin sections from remagnetised units, employing synchrotron-based XRF and XAS data. This microscopic scrutiny enhances our comprehension, providing a nuanced perspective on the geological intricacies under investigation.

Because samples from the Guia Formation come from two distinct locations they were named correspondingly, Cáceres – GC in the deformed terrain, and Tangará (GT) over the Amazon craton (Figure 2b). Because the basal section of Mirassol d'Oeste (Figure 2e) formation was said to carry only a primary component, samples from the same sections studied by Trindade et al. (2003) were re-investigated, to check the occurrence of false positive "remagnetisation fingerprints". Samples from the Irecê basin (from the Salitre Formation) are identified as IR, and samples from the Bambuí (Sete Lagoas Formation) are identified as BB (Figure 2a).

3.1 Rock magnetism

Most of the magnetic carriers of the Neoproterozoic rocks used in this project were characterised more than fifteen years ago (D'Agrella-Filho et al., 2000; Font et al., 2006; Trindade et al., 2004). An updated experimental approach, mixing traditional and updated techniques, is the first step towards a better understanding of the magnetic assemblage in these carbonate rocks. The original set of samples are classical cylindrical palaeomagnetic samples. Initially, to characterise the remanence carriers, ARMs were induced in AF demagnetised samples using a Long Core SQUID magnetometer (2G Enterprises), imparting a DC field of $100\mu T$ and AF fields from 0-10 mT along the Z-axis.

Since the contribution of grains between SP and SD states may play an important role in the fingerprints of remagnetised carbonates, we intended to semi-quantified their presence by measuring the magnetic susceptibility (of the cylindrical specimens) in low and high frequencies as well as out-of-phase and in-phase magnetic susceptibility with an Agico Kappabridge MFK1 equipment. The magnetic susceptibility of each sample was measured five times in succession and sequentially calculating their arithmetic mean. These measurements were performed in a room with a controlled temperature (21°) on the same day (to avoid any instrumental disturbances). Frequency-dependent magnetic susceptibility is traditionally used to investigate the occurrence of superparamagnetic and stable single-domain grains (Hrouda et al. (2013)). The most common frequencies for these studies are 976 Hz (low frequency) and 15616 Hz (high frequency), which were used here to investigate the susceptibility at a low-intensity AC field of 200 Am^{-1}. The parameter χ_{FD} (Eq. 1) introduced by Dearing (1996) measures the percentage of susceptibility loss between low and high frequencies (related to the contributions of ultrafine ferromagnetic particles), in which χ_{LF} and χ_{HF} are the in-phase low and high frequencies, respectively. Hrouda (2011) introduced the χ_{FN} (Eq. 2) parameter, which despite representing the same interpretation of χ_{FD} has a decreased dependency on the operating frequency, allowing a more realistic approach. Finally, the

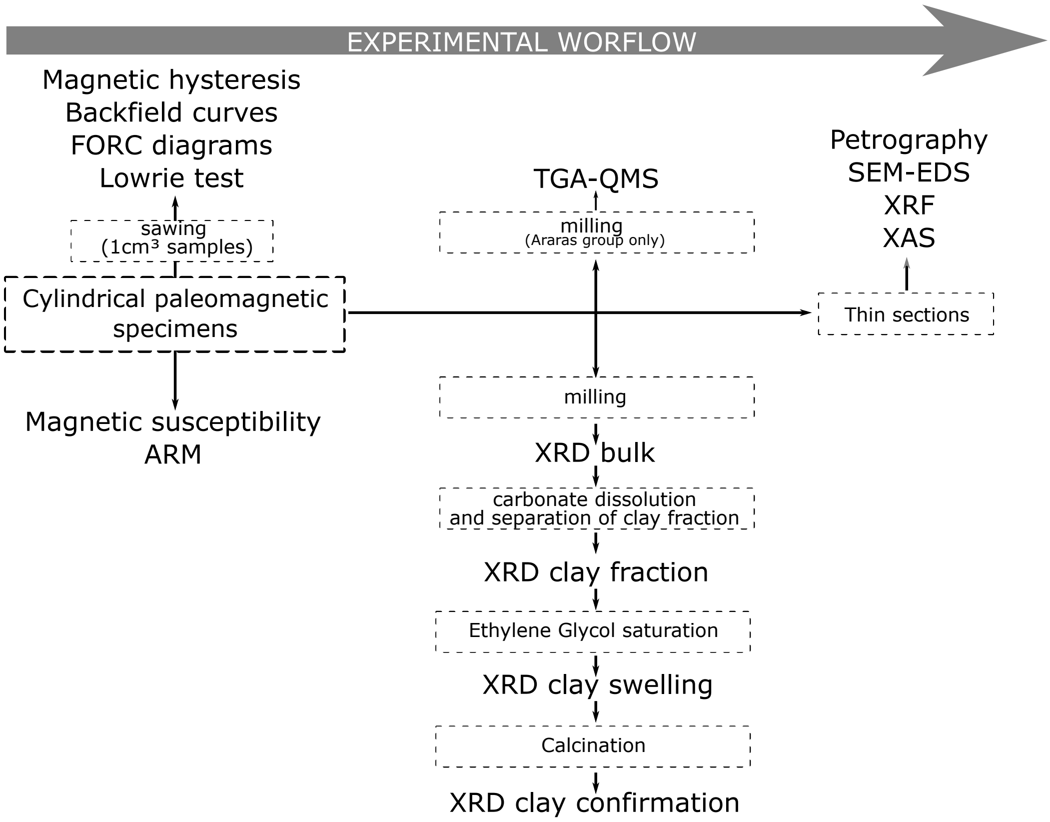

Figure 3. Experimental workflow, moving from macro to micro analysis. FORC: First Order Reversal Curves; ARM: anhysteretic remanent magnetisation; XRD: X-ray diffractometry; TGA-QMS: Thermogravimetric analysis coupled to a Quadrupole Mass Spectrometer; SEM-EDS: Scanning electron microscopy with energy dispersive X-ray spectroscopy; XRF: X-ray fluorescence; XAS: X-ray absorption spectroscopy.

low-frequency phase angle (δ_{LF}) related to the out-of-phase susceptibility is also an interesting tool used to calculate the contributions of the SP/SD threshold through the χ_{ON} parameter (Eq. 3). We make use of these parameters to verify the loss of susceptibilities in our samples.

$$\chi_{FD} = \frac{\chi_{LF} - \chi_{HF}}{\chi_{LF}} \cdot 10^2 \tag{1}$$

$$\chi_{FN} = \frac{\chi_{FD}}{ln(HF) - ln(LF)} \tag{2}$$

$$\chi_{FN} = 200 \cdot \pi^{-1} tan(\delta_{LF}) \tag{3}$$

Sequentially, the cylindrical samples were sawed to extract small fragments for measurements in a vibrating sample magnetometer (Princeton Measurements Corporation MicroMag, VSM Model 2900; noise level $2 \cdot 10^{-9} Am^2$). Magnetic hysteresis and backfield curves were performed for all of them. Samples that represent the overall behaviour of each population followed by the acquirement of first-order reversal curves (FORCs, Roberts et al. (2000)) to further investigate the domain state and magnetic interactions of these assemblages of particles. The use and processing of FORC (First-Order Reversal Curves) diagrams to investigate the magnetic domain (for rock/environmental magnetism and palaeomagnetism fields) regarding an assemblage of ferromagnetic particles in rocks have increased over the last two decades (Carvallo et al., 2004, 2006; Egli et al., 2010; Egli, 2013; Heslop, 2020; Lascu et al., 2018; Muxworthy & Dunlop, 2002; Pike et al., 2001; Roberts et al., 2000), including its use in carbonate geological materials (Abrajevitch & Kodama, 2009; Chang, 2013, 2014; Roberts et al., 2013). FORCs may offer a more robust approach than other techniques that infer magnetic domain, since the investigation occurs through scanning of different coercivities, almost as a map of the components that would form a magnetic hysteresis. There are distinct approaches to acquiring the data for FORC diagrams. As the distribution of the FORC is calculated through a mixed second derivative of the magnetisation by the reversal and applied fields (Roberts et al., 2000), any noise is strongly intensified. This can be problematic when dealing with carbonate rocks, mainly because data tends to be naturally noisy.

In our experiments, FORC measurements were carried out in cubic samples ($\approx 2cm^3$). For each sample, the routine involved acquiring 300 first-order reversal curves (N-FORcs) using the following parameters: (i) a discrete field sweep mode; (ii) an averaging time of 0.5 s; (iii) pauses of 1s at the saturation, calibration, and reversal fields; (iv) Bc_{min} =0 mT and Bc_{max} =150 mT; Bu_{min} =-80 mT and Bc_{max} =+80 mT; and a saturation field of 400 mT. Data were acquired in triplicates and further linearly combined to enhance signal/noise ratios, and finally processed through a Python-based statistical machine learning package (FORCsensei, Heslop (2020)). Preprocessing involved corrections of saturation slope (at 70%), drift measurements, and normalisation by mass. Even after stacking the data, its noisy nature requires a considerable amount of smoothing. For that, it was also assumed a symmetrical vertical and horizontal smoothing, limiting the maximum smoothing factor to 5.

Finally, Lowrie (1990)'s test was also carried out on representative samples by imparting three orthogonal IRM (through a 2G pulse magnetic field inducer, with distinct field intensities of 1.2T, 0.4T, and 0.12T) and further thermally demagnetising (100-700°C) the samples to estimate unblocking temperatures of the hard (1.2-0.4T), medium (0.4-0.12T) and soft ($< 0.12T$) magnetic carriers. The remaining remanence after each demagnetising step was measured.

3.2 X-ray diffractometry and crystallinity index

Authigenic growth of ferromagnetic phases due to smectite-illite transformations is among the common phenomena summoned for carbonate remagnetisation. As discussed by Huggett (2005), the illitisation of smectites vs depth is the most studied aspect of clay diagenesis. Smectites are a group of phyllosilicates (Kloprogge et al., 1999), which consist of layers of two-dimensional "sheets" formed by planes of oxygen atoms coordinated to Si, Al, Mg, and Fe. These minerals have a 2:1 structure layer, formed by two tetrahedral sheets with a single bound (on each side) of an octahedral sheet.

Illites are a clay mineral class that has non-expandable layers (Brigatti et al., 2013), being a common phyllosilicate. The illitisation of smectites, which starts around 70° and peaks around 120/130° (although the geothermal gradients of a basin might lead to earlier reactions), occurs if K^+ is available, following either of two reactions (Huggett, 2005):

$$(i)\ smectite + Al^{3+} + K^+ \rightarrow illite + Si^{4+} + Fe^{2+} + Na^+ + Mg^{2+}$$
$$(ii)\ smectite + K^+ \rightarrow illite + Si^{4+} + Fe^{2+} + Na^+ + Mg^{2+}$$

K-feldspar dissolution is the main source of K^+ inputs. The second (ii) reaction preserves aluminium but requires a partial dissolution of the smectites. These processes represent a continuous transformation that results in mixed layers of smectite-illite (I-Sm), in a way that illite is randomly interstratified between the expandable layers when the transformation is at the earlier stages of the reaction (Lanson et al., 2009). Because one of the possible mechanisms related to the growth of authigenic magnetite is a conversion of Fe-rich smectite to illite, selected samples were submitted to X-ray diffractometry (XRD) to identify their solid phases (especially to verify the presence of clay minerals). The selection criteria were to select the samples that showed, simultaneously: (i) the highest magnetic susceptibility, (ii) paramagnetic contribution to hysteresis larger than 80% (iii) a considerable loss in magnetic susceptibility for higher frequencies (greater than 10%).

Samples were manually crushed with agate mortar and pistil, then settled in a section to be further analysed in a Bruker diffractometer, from 2 to 99° with step sizes of 0.02° (2θ) using a copper source radiation (25 mA, 40 kV). Sequentially, the raw data were treated using the software HighScore Plus (Malvern Panalytical) by striping any K-Alpha2 $\mathring{A}$ contributions and quintic smoothing the product. Peaks were identified and matched to the solid phases by analysing both their position and their lattice spacing (d-spacing).

The series of crystalline arrangements and the progressive transformation of smectite to illite is a temperature-dependent process, so the crystallinity of illite increases with temperature increase. A common way to access palaeotemperatures in illite-bearing sedimentary rocks is to use the Kübler index (KI, (Kübler, 1964, 1967, 1968, 1990)). To calculate KI, the clay fraction ($< 2\mu m$) of the sedimentary rock is separated, and XRD data is collected using a $CuK\alpha$ radiation source, and the full width at half maximum (FWHM) of the 10° peak is calculated. This index is used to separate late-diagenetic (towards anchizone, very low grade/incipient metamorphism) and epizone (low greenschist facies), in a way that the smaller KI the higher the palaeotemperature (Jaboyedoff et al., 2001). XRD data of the remagnetised units in our work were further investigated to use the KI as a constraint for possible exposure to low-grade metamorphic conditions.

Powder samples were individually submitted to a weak acid solution (acetic acid 2 M + sodium acetate 1M [4:1], pH ≈ 4, as Strehlau et al. (2014)) in a Becker flask, and stirred at $40°C$ for an hour. After neutralising the solution, the thin fraction was separated through a decantation process, and the supernatant was transferred to a plate, so the clay minerals could settle as they dried. Platy clay minerals tend to orient themselves parallel to the glass slide during settling, which enhances the peak intensities of basal planes (Tohver et al., 2008). Finally, samples were submitted to sequential XRD acquisition procedure:

(i) ordinary data acquisition after drying the clay fraction, (ii) XRD after ethylene glycol impregnation, and (iii) after calcination at 550°C. Background removal was performed by adjusting a forward model, either with linear or logarithmic decaying curves to better describe the spectrum. Calculation of KI values was performed by optimising the parameters of a Gaussian distribution through a non-linear least squares fitting (Gauss-Newton method, Aster et al. (2013)) in a Python environment.

3.3 Micro-to-nanoscopic imaging/chemical analysis

Using the same criteria as those for XRD, thin sections of four samples were produced to perform an overall microscale analysis of their petrographic features (under natural and polarised light). Microscopic imaging was performed on the same thin sections (after carbon platting) study on the petrographic analysis. An electronic microscope (HELIOS 5 PFIB CXE DUALBEAM) is used to achieve visual analysis (on the secondary electrons, SE-mode) and to accomplish chemical mapping of microscopic regions through energy dispersive spectroscopy (EDS). Since the major interest is in the thin magnetic carriers of stable remanence, this section focuses on finding PSD-range iron oxides/sulphides in the remagnetised units, and their spatial correlation with other mineral constituents.

Synchrotron radiation is a powerful electromagnetic wave (Yamashita, 2003) and an important X-ray source that can help to understand the physical properties of materials at a nanoscopic scale, providing also (Duncan, 2018): a chemical profile with incomparable resolution, and measurements of geometric structures to thousands of nanometers with elemental sensitivity. For geological samples, it has potential use in matters such as X-ray absorption spectroscopy, X-ray diffraction, and X-ray fluorescence (Henderson et al., 1995). Since X-rays are ionising radiation, they can absorb energy and eject core electrons from atoms. Scanning the X-ray through a specific binding energy results in the detection of an abrupt increase in absorption (called rising absorption edge, sometimes preceded by a brief increase in absorption that is called a pre-edge), which will be specific to a determined core-electron binding energy (and therefore specific to an element) and named according to the quantum number of the excited electron (Penner-Hahn, 2003). X-ray absorption spectroscopy (XAS) comprises two segments: X-ray absorption near-edge structure (XANES), and ii) extended X-ray absorption fine structure. While EXAFS studies are more commonly applied to amorphous/unstructured materials providing information on the electronic structure of specific sites within materials, XANES gives relatively straightforward information about the oxidation state of the central absorbing atom (Ormerod, 2001). Besides, XANES is also sensitive to local coordination, chemical composition, and crystal structure (Zhu et al., 2021).

Since most studies of carbonate rocks are characterised by bulk measurements (mainly due to the low content of iron oxides and their nanoscopic size), this work explores synchrotron radiation for both XRF and XAS analysis to achieve in-situ high-sensitive characterisation of remagnetised samples (Sete Lagoas, Salitre, and Guia Formations). Because no significant magnetic distinction between GC and GT is observed, the following analyses were performed on a GC sample. Experiments were conducted in a Coherent X-ray Nanoprobe Beamline (CARNAÚBA, Oliveira et al. (2014)), at the Brazilian Synchrotron Facility (SIRIUS, Figure 4a) which yields a spectroscopic range of 2.05 to 15 keV energy (Tolentino, 2017). Data was acquired through an environmental in-air nanoprobe (tender-to-hard X-ray for sub-micro analysis, TARUMÃ, Figure 4b), where the thin sections were positioned (Figure 4c) to adjust the beam to selected regions (around 2 $\mathbf{mm^2}$). The samples are then raster-scanned to obtain two-dimensional data (Tolentino, 2021).

For XRF data, Gaussian distributions were adjusted to the log of peak intensity (y) vs energy (E), using mean distribution values μ to obtain a qualitative concentration of this element within an area. XAS data was collected in fluorescence mode around the Fe K-edge (activation energy, $E_0 \approx 7112$ eV), using metallic Fe-foils to calibrate the monochromator,

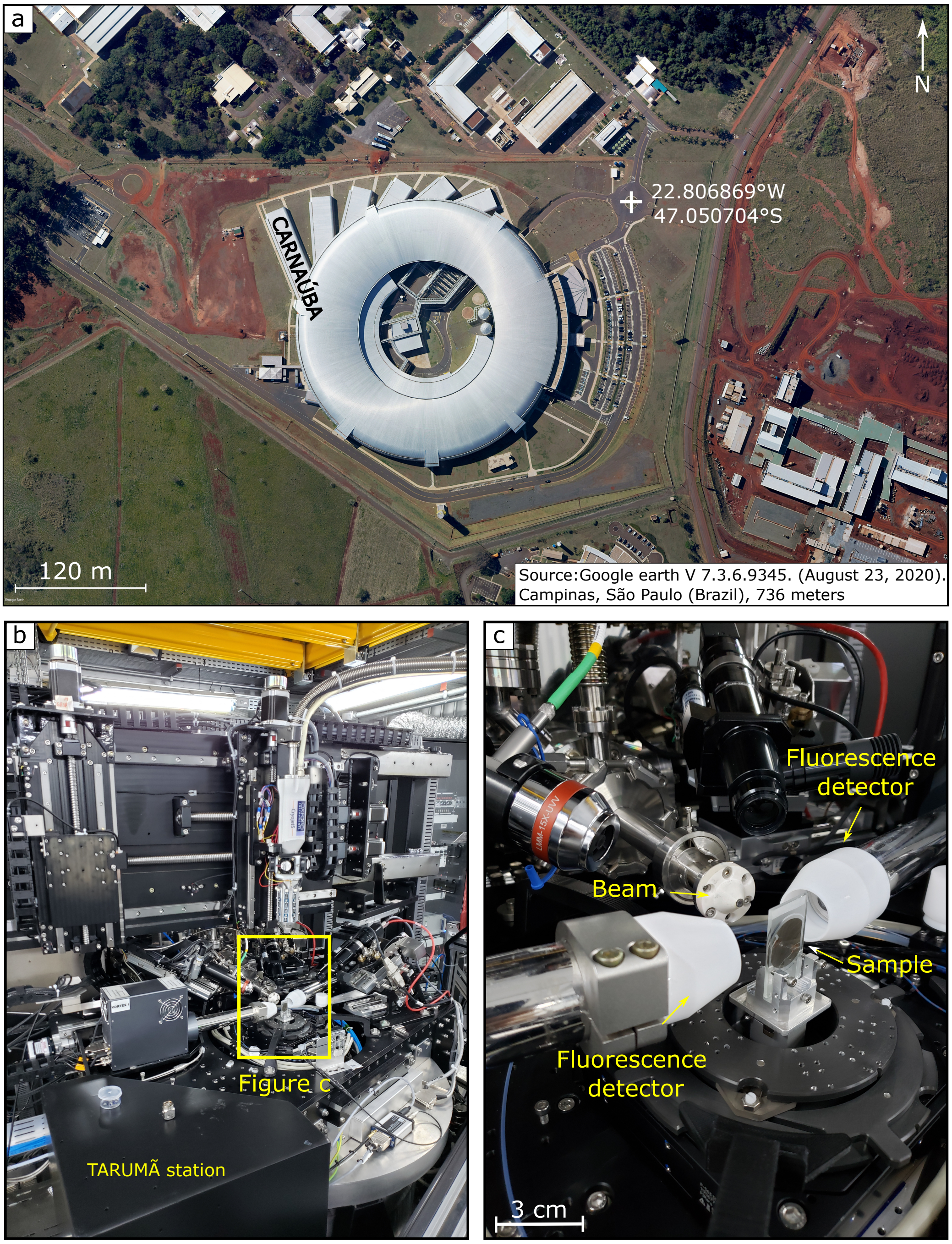

Figure 4. Experimental setup for highly detailed XRF and XAS analysis. a) SIRIUS, the Brazilian Synchrotron facility, and the CARNAÚBA beamline. (c) the TARUMÃ station (at the CARNAÚBA beamline), and focus on the sample holder region (b), showing fluorescence detectors and the position of the incoming synchrotron radiation beam.

performing three sequential scans in each sample to optimise the signal/noise ratio. The normalisation procedure applied in this work is similar to those applied in specialised software (Ravel & Newville, 2005). XAS data of αFe_2O_3, γFe_2O_3 and Fe_3O_4 were compiled from Piquer et al. (2014), while FeS_2 data was retrieved from Ravel (2013) , used as comparisons against our experiments.

3.4 Thermogravimetric analysis coupled to a Quadrupole Mass Spectrometer (TGA-QMS)

To better correlate the presence of hydrocarbon and sulphur in samples of the Mirassol d'Oeste and Guia Formation (Check Figure 2e for clarity), thermogravimetric analysis coupled to a Quadrupole Mass Spectrometer (TGA-QMS) was performed under constant synthetic air flow (40m/min) on samples from the Guia Formation over the Amazon craton (GT) and its underlying bitumen-enriched dolostones from the Mirassol d'Oeste ($MO_{transition}$, as well as bitumen-poor samples from the dolostones immediately above the diamictites of the Puga formation (MO_{base}). We intend to understand the differences in the amount of organic matter (CO_2) and sulphur content (SO_2, SO_3), by checking the mass loss as temperature increases.

4 Results

4.1 Rock magnetism

4.1.1 Frequency dependent magnetic susceptibility

Samples from the three studied basins showed magnetic susceptibility loss from low to high frequencies. The displacement in the susceptibility distribution is better observed in the respective boxplots of each group (Figure 5). The calculated large χ_{FD} values for most of the samples are considerably large, although some of them (mostly for the Irecê samples, IR) are below 5% (Figure 5h). Samples from the Araras Group had the most expressive loss of susceptibility, which is evident in the χ_{FN} values of Guia Formation (Figure 5i,j).

Two GT and GC samples have shown extreme values of susceptibility loss (Figure 5i,j). Because χ_{FN} and χ_{ON} parameters should be equivalent, we would have expected a linear trend. Such anomalous responses in GT and GC samples are present in distinct frequencies since they show a linear tendency when comparing χ_{FN} and χ_{ON} parameters. As discussed by Hrouda et al. (2013), diamagnetic materials, such as calcite, tend to increase δ_{LF} and result in large χ_{ON} values. Yet, χ_{FN} and χ_{ON} values are coherent, so linear regression through least squares fit for all the groups shows determination coefficients $R^2 > 0.79$. The higher dispersion, observed when comparing χ_{FN} and χ_{ON} for the Irecê (IR) samples is more evident, which could be the result of paramagnetic phases decreasing δ_{LF} or susceptibility measurements that are close to the minimum experimental.

Remagnetised carbonate rocks usually show χ_{FD} greater than 5% (Font et al., 2006; Jackson & Sun, 1992), and such has been interpreted as a result of an important contribution of superparamagnetic grains. χ_{FN} values of remagnetised units indeed show an important loss of magnetic susceptibility. However, the Mirassol d'Oeste basal samples (which are our control test) yield a considerable loss of susceptibility ($> 5\%$), showing a comparable behaviour to the IR samples.

4.1.2 ARMs, Magnetic hysteresis and backfield curves parameters

Apart from a few samples, the general behaviour of ARM curves (*Supplementary file*, Figure S1) is coherent within the same unit. Some samples of the Bambuí and Irecê units seem to be far from reaching saturation at 100 mT. In Bambuí samples, the slope of magnetisation curves is shallower compared to those of Irecê, indicating the presence of more

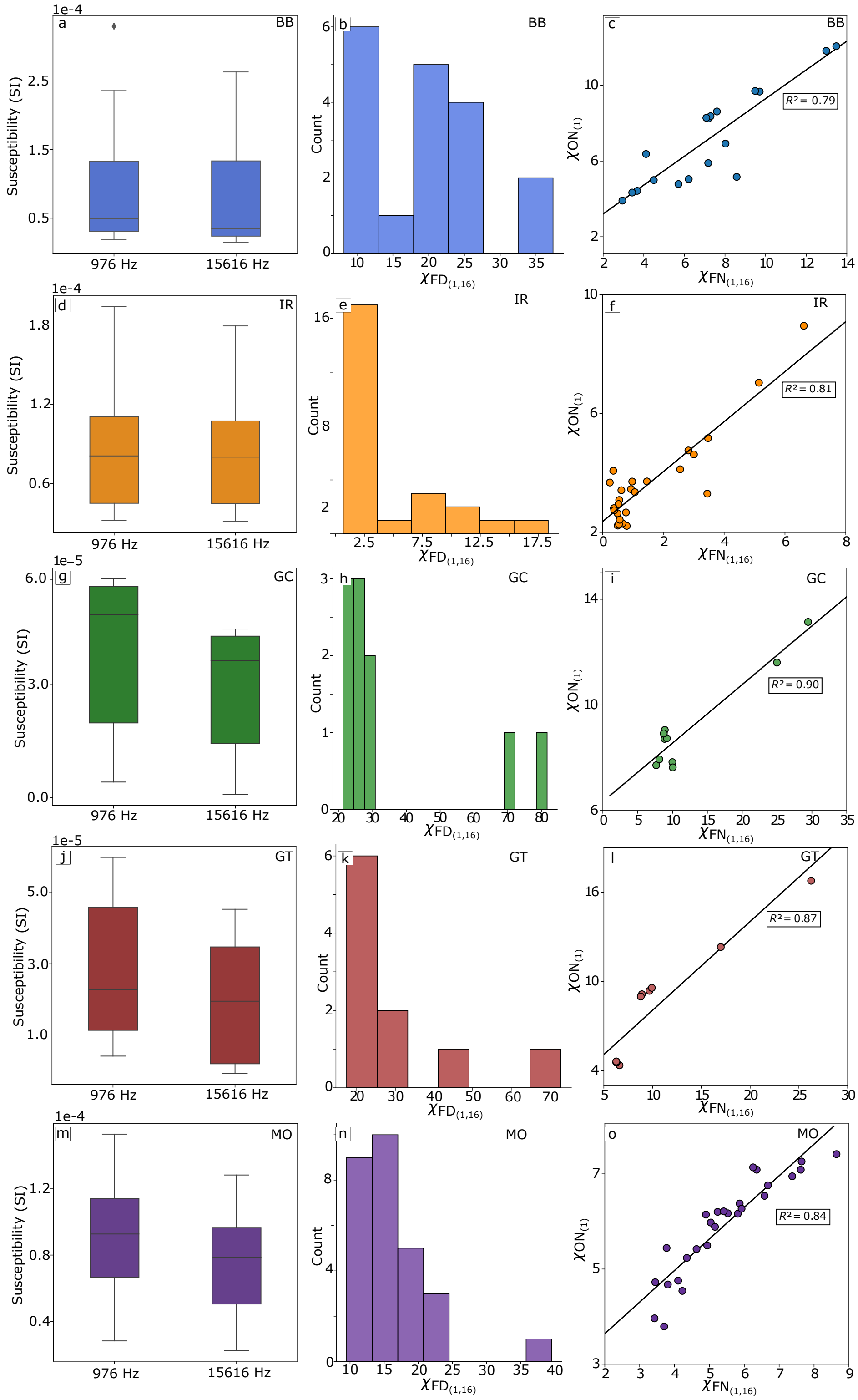

Figure 5. Frequency-dependent magnetic susceptibility of samples from the Bambuí (BB) and Irecê basin (IR), as well as from the Araras group: Guia Formation (GC, GC) and Mirassol d'Oeste formation (MO). χ_{FD},χ_{FN} and χ_{ON} follow Eq. 1, Eq. 2, and Eq. 3, respectively. The subscript number in front of the susceptibility parameters indicates an approximation of the experimental frequencies in kHz. Diamonds are outliers in the boxplot distribution.

coercive phases in the second ones. However, another behaviour can also be observed in other samples from the same units, which are very similar to those of the Guia Formation, where most of the magnetisation is acquired up to 70 mT. In the Araras Group, samples from Guia Formation and Mirassol d'Oeste seem near to reaching saturation at 100 mT. Regardless, the slope of Mirassol d'Oeste samples is steeper, indicating a larger contribution of low coercivity minerals. The gradient of the ARMs acquisition curves of all units shows that most of the magnetisation is achieved at coercivities below 20 mT, which could be typically explained by the presence of magnetite. Coincidentally, these samples (BB, IR, GC, and GT) also show coincident peaks of coercivity around 40 mT, which is absent in the dolomites of the Mirassol d'Oeste Formation. Such behaviour could be related to the significant presence of more than one remanence-bearing mineral in the remagnetised units.

The uncorrected hysteresis analysis reveals a significant involvement of paramagnetic materials in the examined samples (Figure 6 b, c, d, and e). This is evident, with over 75% of the samples demonstrating a paramagnetic contribution of approximately 80% at the maximum applied field. Furthermore, upon analysing the gradient of an irreversible loop, the presence of a linear component in magnetisation (attributed to the paramagnetic component) is observed, resulting in a positive basal displacement of the gradients ((U. Bellon et al., 2023)). Notably, this paramagnetic contribution can entirely surpass the ferromagnetic contribution, reaching values as high as 99% of the sample saturation magnetisation in some instances. This is an important observation because it points towards a significant input of iron-bearing silicates in these carbonate rocks. Some examples of minerals associated with paramagnetic behaviour that could be accessory phases in carbonates are kaolinite $(Al_2(Si_2O_5)(OH)_4)$, a silicate that might have small amounts of transitional elements, such as Fe, Mn, and V which might lead to paramagnetic behaviour (Schreiner, 2002); chlorites $(Mg, Al, Fe)_{12}[(Si, Al)_8O_{20}](OH)_{16}$ (Martín-Hernández & Hirt, 2003), a group of micaceous phyllosilicates; and more interestingly, Fe-rich smectites (Callaway & McAtee, 1985) and (iii) illites (Potter et al., 2004).

When corrected from the paramagnetic/diamagnetic contribution, distorted hysteresis loops are more clearly observed for the remagnetised carbonates. Saturation is not achieved in fields below 100 mT for most of the samples. Bambuí samples have commonly a wasp-waisted (constricted middles) hysteresis loop (Figure 6b), which is indicative of mixing populations of magnetic carriers with very distinct coercivities, or the combination of superparamagnetic and single domain behaviours in the same sample (Tauxe et al., 1996). Hysteresis from Irecê samples, however, look more like potbellies (wider middles and curved shoulders, Figure 6c). While this behaviour is more common in magnetic assemblages where the population of SP grains is $< 30nm$, wasp-waisted hysteresis caused by a mixture with SP grains is not common to thresholds smaller than 8 nm (Tauxe et al., 1996). Whereas the signature of the Bambuí samples is compatible with the presence of magnetite, coercivities as large as those in some of Irecê samples indicate the presence of minerals with larger coercivities but are not excluded, however, the presence of magnetite as well. Samples from the Guia (Figure 6d) and Mirassol d'Oeste (Figure 6e) formations have similar magnetic hysteresis but distorted loops frequently appear for the Guia samples. There is no significant difference between the deformed and undeformed terranes (GC and GT samples, respectively). Potbellies are absent in this group, but wasp-waisted hysteresis frequently occurs.

One of the ways to interpret the results of magnetic hysteresis and backfield data as bulk indicative of the magnetic domain state. As there are other methodologies to infer domain state (as FORC diagrams, which will be further discussed), remagnetised carbonates are known to follow a trend in Day plot (Day et al., 1977). Therefore, we still believe it is a valid discussion comparing our signatures against these trends in such a diagram. Parry (1982), as discussed by (Jackson, 1990), showed that mixtures of PSD + MD or SD + MD magnetite follow a power law that relates magnetisation and coercivity as:

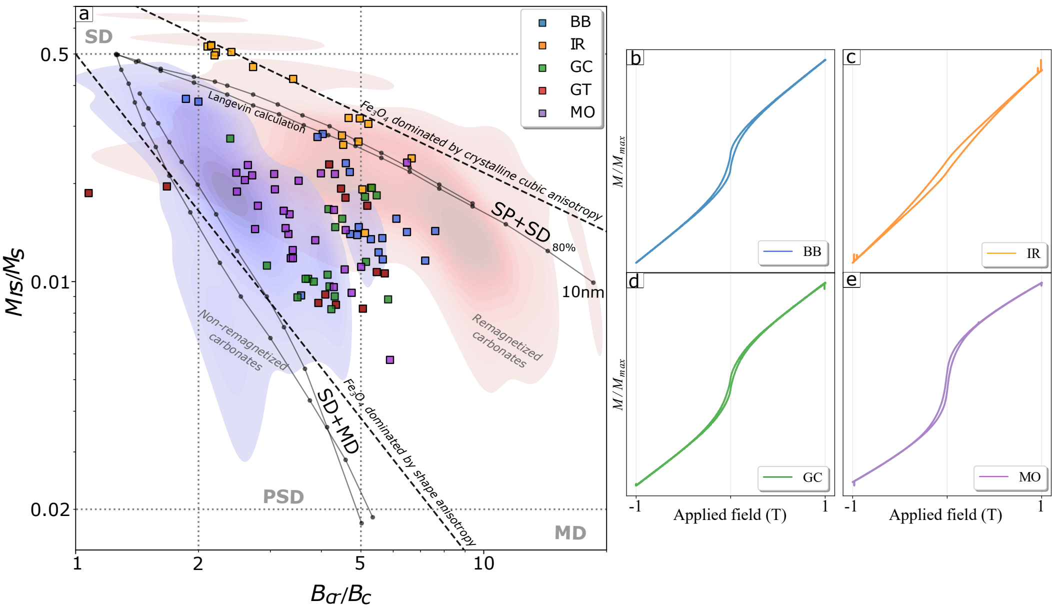

Figure 6. a) Bilogarithmic Day plot compiling data from magnetic hysteresis and backfield curves from the analysed samples. Solid black lines are the mixtures of multidomain (MD) + single-domain (SD), or a mixture between single domain (SD) and superparamagnetic population of magnetite (following Dunlop (2002)). Solid grey lines are the theoretical trends followed by a single-sized population of magnetite controlled by shape anisotropy (intercept at 0.5 in the Mrs/Ms-axis) and controlled by crystalline cubic anisotropy (intercept at 0.89 in the Mrs/Ms-axis) (Parry, 1982; Jackson, 1990). The blue and red contours represent density frequencies of non-remagnetised/remagnetised carbonates, respectively (data manually acquired from Jackson and Swanson-Hysell (2012)). Plots on the right are representative magnetic hysteresis of each studied unit. Remagnetised carbonates yielded distorted loops, for which Bambuí (b) and Guia samples (d) are mostly wasp-waisted and Irecê samples are potbellies (c). Mirassol d'Oeste samples (e) are ordinary low coercivity loops expected for magnetite-bearing rocks.

$$\frac{M_{rs}}{M_s} = c \cdot \left(\frac{B_{cr}}{B_c}\right)^m \tag{4}$$

If shape anisotropy is dominant in the particles that compose the sample, and if the particles are normally single-sized, the trend produced by Eq. 4 will follow a line defined by $c = 0.5$ and $m = -1.6$ (Jackson, 1990; Parry, 1982). In the bilogarithmic Day plot of Jackson and Swanson-Hysell (2012), when the Bcr/Bc ratio approaches unity, the trend related to remagnetised Appalachian carbonates reaches a shallower slope $m = -0.6$ and a higher intercept ($c = 0.86$). Such a ratio coincides with the expected magnetocrystalline cubic anisotropy of SD particles (Wohlfarth & Tonge, 1957). However, as previously discussed, the hypothesis of magnetocrystalline cubic anisotropy being responsible for the abnormal hysteresis ratios originates directly from the intercept value of the power law-trend-line in the Day plot. Therefore, a stronger influence of particles dominated by magnetocrystalline anisotropy could not necessarily be a fingerprint of remagnetised carbonate rocks (as discussed by Jackson and Swanson-Hysell (2012)). Samples from the Bambuí group and Araras group mostly plot far from the single-sized shape-controlled anisotropy but do not follow the North American carbonate trend as well (Figure 6a), which is considered to be a "false negative" to magnetic fingerprinting, in other words: samples are palaeomagnetically remagnetised but their bulk hysteresis properties do not follow the expected fingerprint. Most of the Irecê samples, in turn, plot right under this trend and seem to follow a trend.

Domain states have a size/shape-constrain dependence. Superparamagnetic threshold (ds) and the critical single-domain size (d_0) vary for different materials and even change depending on the shape of the same material (Butler & Banerjee, 1975). For equidimensional grains, at 20°C, of (i) magnetite, ds are usually between 0.025 and 0.030 µm and d_0 = 0.05- 0.06 µm; (ii) for haematite, ds are similar to those in magnetite, but d_0 might reach dimensions of up to 15 μm, while (iii) pyrrhotite have a critical single domain size at 1.6 μm (Dunlop & Özdemir, 1997). Most of the magnetic particles in rocks are, however, not entirely described by MD or SD theory, exhibiting a non-uniform magnetic state classified as PSD (Nagy, 2017). Most of the analysed data fall within the PSD field, although some of them could be explained by the non-linear mixing theory from (Dunlop, 2002), especially the samples from the Mirassol d'Oeste formation.

U. Bellon et al. (2023) employed an unmixing method to discern susceptibility components within distorted hysteresis loops from both the Salitre and Sete Lagoas Formations. Despite the inherent limitations of any parametric unmixing method, which relies solely on the model's capacity to explain a given phenomenon, the researchers demonstrated that pot-bellies and wasp-waisted features in BB and IR samples could arise without necessitating a substantial contribution from SP particles. Instead, these features were attributed to the presence of different coercivity components, corresponding to distinct minerals. Given that paleomagnetic data already indicate the presence of both monoclinic pyrrhotite and PSD magnetite in the remagnetised units, their alignment in the Day plot posed challenges in connecting them to their respective domain states. Nevertheless, it was noted that mixing scenarios involving SP + SD, PSD + SP, and similar combinations could generate a variety of distributions below the 0.5 Mrs/Ms threshold, as discussed by (Dunlop, 2002). Consequently, the mixture of distinct magnetic populations in remagnetised carbonates could exhibit considerable dispersion.

4.1.3 FORC diagrams

Most of the Bambuí samples (Figure 7a') comprise an important contribution in the coercivity axis (Bc), with little contribution to the interaction axis (Bu), typical of non-interactive SD particles(Roberts et al., 2000; Roberts, 2022). Central-ridge contribution is also commonly related to the presence of biogenic magnetite, like magnetotactic bacterial magnetite in pelagic sediments (Roberts, 2011), whose sharpness is associated with little magnetostatic interactions. Ultrafine authigenic magnetic particles may also contribute to the central ridge response, but this contribution depends on how dispersed the matrix of the particles is (Egli et al., 2010). Geiss et al. (2008) also argued that highly dispersed pedogenic SD magnetite contributed to a lack of magnetostatic interactions. The centre of the distribution in (Figure 7a') is near the origin of Bc and spreads towards higher field values, which probably suggests the presence of an assemblage of particles with a variety of coercivities. This could be explained by a range of SD/vortex-state particles of magnetite and pyrrhotite sparsely distributed within the carbonate matrix.

As previously shown by the hysteresis curves, Irecê samples contain a set of variable coercivity ranges. For most of them, FORC diagrams are extremely noisy, even after linearly combining multiple stacks of the same samples. The FORC below resembles potbelly-like loops (Figure 7b). The effects of smoothing and artefacts generated through the processing are recognised as medium-intensity contributions far from both the central ridge and the origin of the Bu-axis (Figure 7b'). However, the main distribution is centred along the coercivity axis, which is similar to the Bambuí samples.

Guia Formation samples from both Tangará and Cáceres regions bear very similar hysteresis/backfield parameters. As expected, FORC diagrams also show no clear signs of magnetic differentiation of both terranes. The main response is usually asymmetric, with distributions centred in the Bc-axis, with small spreading towards the interaction axis, a product attributed to the PSD state. Increasing grain size within the PSD threshold results in a decrease of coercivity and in progressive diverging towards the Bu-origin and becoming more MD-like (Roberts et al., 2000, 2014). However, some samples have only a major distribution along the coercivity axis, similar to what is observed in the Bambuí-samples. Very few samples of the Guia Formation (both from Tangará and Cáceres regions) showed an important diamagnetic contribution, since the majority of them bear an important amount of clays. Even in these samples, the ferromagnetic contribution is distinguishable (Figure 7c), but diamagnetic correction results in diagonal positive/negative intercalation of artefacts (Figure 7c'). Nevertheless, the major contribution to the coercivity axis is visible, a probable result of non-interactive single-domain grains.

FORC diagrams of the non-remagnetised unit of the Araras Group (Mirassol d'Oeste) often show a PSD-like behaviour, which is similar to the major response of the Guia Formation samples, and diagonal artefacts might appear as a response from paramagnetic corrections. However, a few of them show (besides the PSD behaviour), an important contribution in the Bu-axis near the origin, indicating that MD particles might be contributing to their spectrum as well (Figure 7d').

In a broad context, the remagnetised carbonates under investigation exhibit similar features in their FORC diagrams. The prominent central ridge not only strongly suggests the presence of stable SD/PSD grains across varying grain sizes but also hints at the potential existence of superparamagnetic grains, as indicated by the eventual extension towards zero along the Bc-axis. While FORC diagrams serve as invaluable tools, it's important to note that they represent the response of the entire assembly of ferromagnetic particles within the rocks. In cases involving samples with magnetic mixtures, discerning the individual contributions of each component to the overall spectrum poses a challenging task. While procedures for unmixing FORC components are available in the literature (Harrison et al., 2018), their effective application necessitates well-defined assemblages, a characteristic not commonly observed in these remagnetised carbonates.

4.1.4 Lowrie test

For the Lowrie test (Figure 8), medium and hard-coercivity components of the BB-2 (Figure 8a) sample show blocking temperatures near $350°C$ and a residual (intensity $< 10\%$) component that is completely decayed at $450°C$, which is indicative of the presence of pyrrhotite and a smaller amount of magnetite, while the soft fraction smoothly decays up to $550°C$ (typical of MD-magnetite). In a few other samples (e.g., BB-16, Figure 8b), pyrrhotite seems

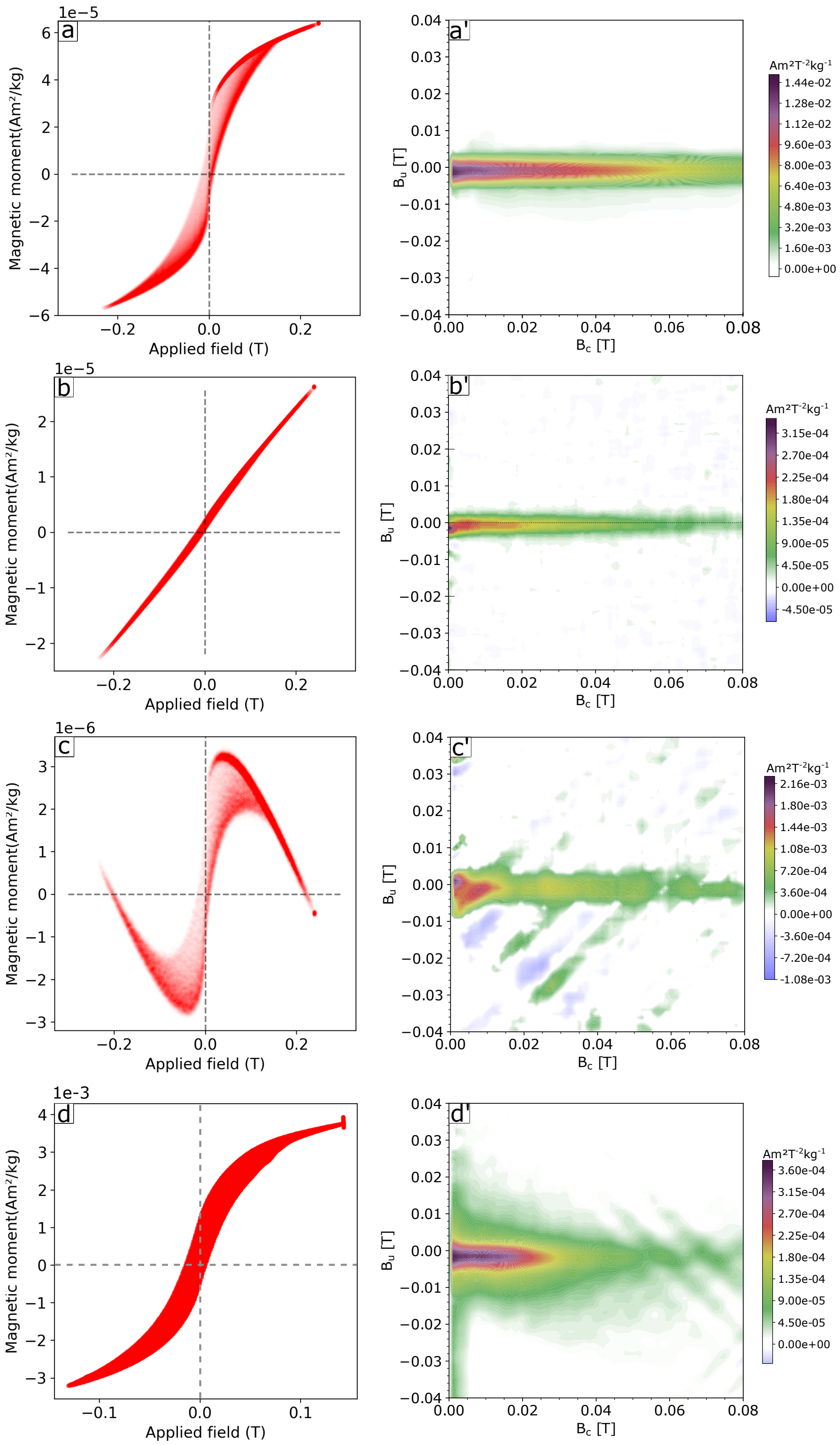

Figure 7. First-order reversal curves (FORC) of representative samples of both remagnetised (a,b, and c) units and non-remagnetised units (d). These FORCs are linear combinations (stacks) of sequential acquisition, to improve the signal/noise ratio. The respective FORC diagrams (a',b',c' and d') were processed through the FORCsensei package and optimised to a smoothing factor of 5.

not to be present as the three components smoothly decay to zero between 500/550°C. Irecê samples that yielded magnetic hysteresis with coercivities larger than 100 mT showed all three components completely decaying at 700°C (indicative of haematite), with no hints of the presence of magnetite or pyrrhotite (e.g., IR-6, Figure 8d). These samples are, however, much less common than those with a coercivity of remanence smaller than 100 mT (e.g., IR-11, Figure 8c), which have shown two components: one around 350°C (pyrrhotite) and another one that slowly completely demagnetises around 500°C (magnetite). The soft component of the IR-11 sample should also be associated with magnetite. These samples are more similar to the signatures observed in the Bambuí samples.

Sample GT-11 (Figure 8e) shows a slower decay of the hard component up to 250°C, from which the decay is steeper up to 350°C, further smoothly demagnetising until 550°C. In this case, the smaller decay temperatures could be associated with maghemite and/or pyrrhotite, while the higher blocking temperature (together with soft and medium components) represents magnetite. For the GC-2 sample (Figure 8f), hard and medium components slowly decay to 400°C, but only completely demagnetise at 500°C (together with the soft component that linearly demagnetises up to such temperature). The latter behaviour is probably related to maghemite/oxidised magnetite (lower blocking temperature) and magnetite (higher blocking temperature).

Medium and hard components of the MO-2 sample (Figure 8g) quickly decay right from 100°C up to 150°C before linearly decreasing up to 580°C. That quick decay could indicate the presence of a higher coercivity mineral (such as goethite). Although there is a component of the soft fraction that demagnetises at 350°C (MO-2 sample, Figure 8c) it differs from Bambuí and Irecê samples in terms of coercivity (since in those the pyrrhotite component is held by medium and high coercivity components). Most of the samples are, however, dominated by magnetite, showing a behaviour more similar to those from the MO-22 sample (Figure 8h), with medium and hard components smoothly demagnetising until 580°C and a soft component linearly demagnetising up to 450°C, from which it slowly demagnetises up to 550°C.

The strong indication of the presence of magnetite and pyrrhotite in remagnetised samples comes from the thermal decomposition of their artificial remanence, as suggested in the bulk magnetic measurements. Additionally, the agreement between the Lowrie test and the previously published NRM demagnetisation data for these units (refer to Section 2) further supports this, where the stable B and C components are associated with monoclinic pyrrhotite and magnetite, respectively. However, the observed varied behaviours within the same units indicate compositional variability within the samples. This variability may explain the dispersion of magnetic ratios within the Day plot (see Figure 6). Moreover, the soft components linked to magnetite may also be associated with coarser grain sizes, potentially originating from a detrital source. This explanation could also be valid for samples containing haematite, as illustrated in Figure 8d.

4.2 XRD

Samples from the Bambuí (Figure 9a) are essentially composed of calcite, but the diffraction patterns also indicate the presence of quartz (SiO_2), chlorite, and possibly feldspars (both K-feldspar and plagioclase), and a minor presence of dolomite. The mineralogical composition of the analysed samples from the Irecê basin (Figure 9b) is very similar to the Bambuí. However, the presence of dolomite and K-feldspar is strongly marked. Data from the Guia Formation (Figure 9c) is different (in some aspects) depending on the different locations since most of the diffraction data from the Cáceres region is related to dolomite and from Tangará it is related to calcite. Samples from the lowermost stratum of the Araras Group, the Mirassol d'Oeste formation (Figure 9d), are almost monomineralic (in terms of major constituents) and composed of dolomite and calcite. The presence of chlorite, however, will be further investigated using ethylene glycol, since smectites have a similar d-spacing

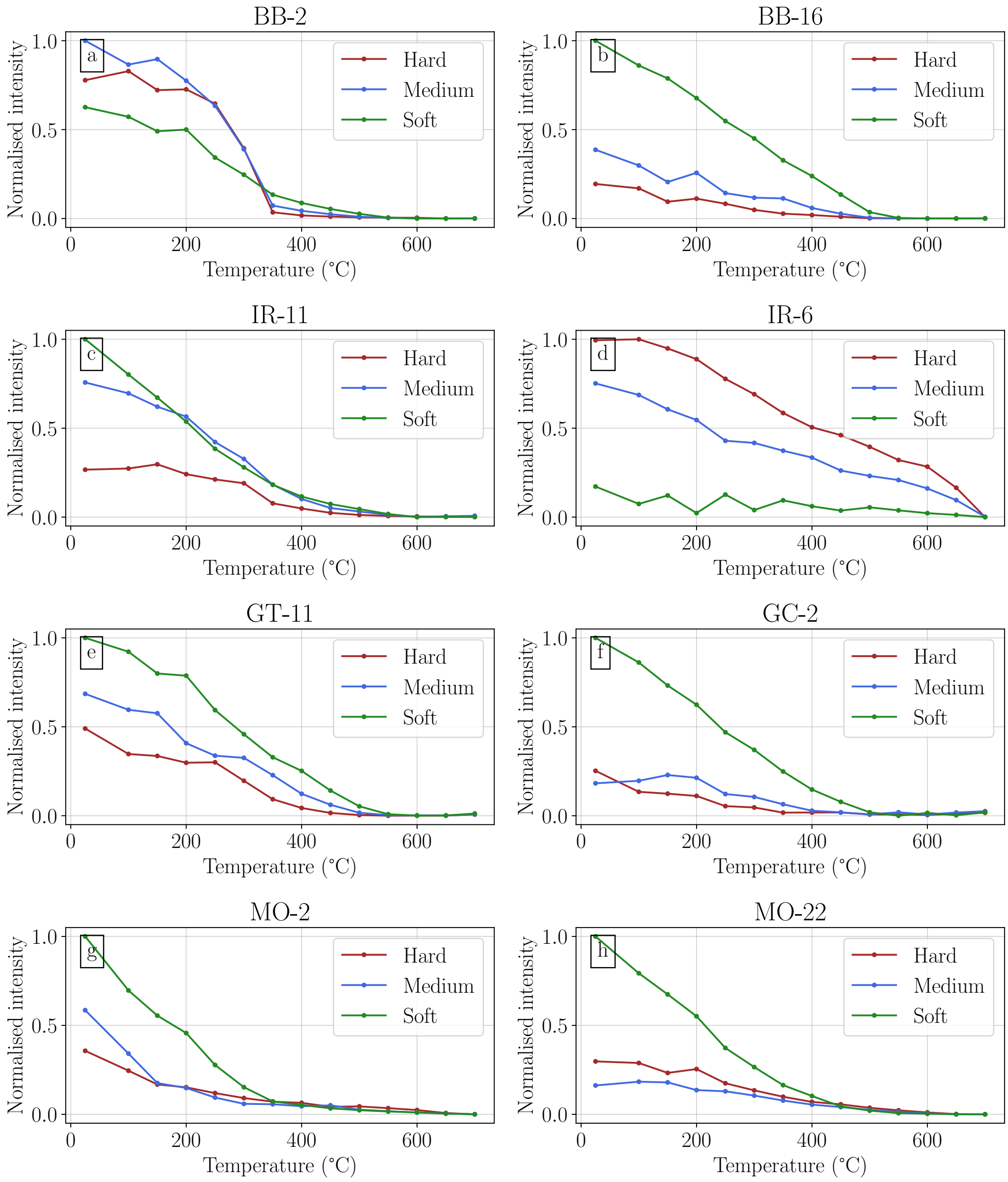

Figure 8. Lowrie (1990) test: an IRM is imparted in three orthogonal directions at three different intensities (1.2 T, 0.4 T, and 0.12 T), followed by thermal demagnetisation.

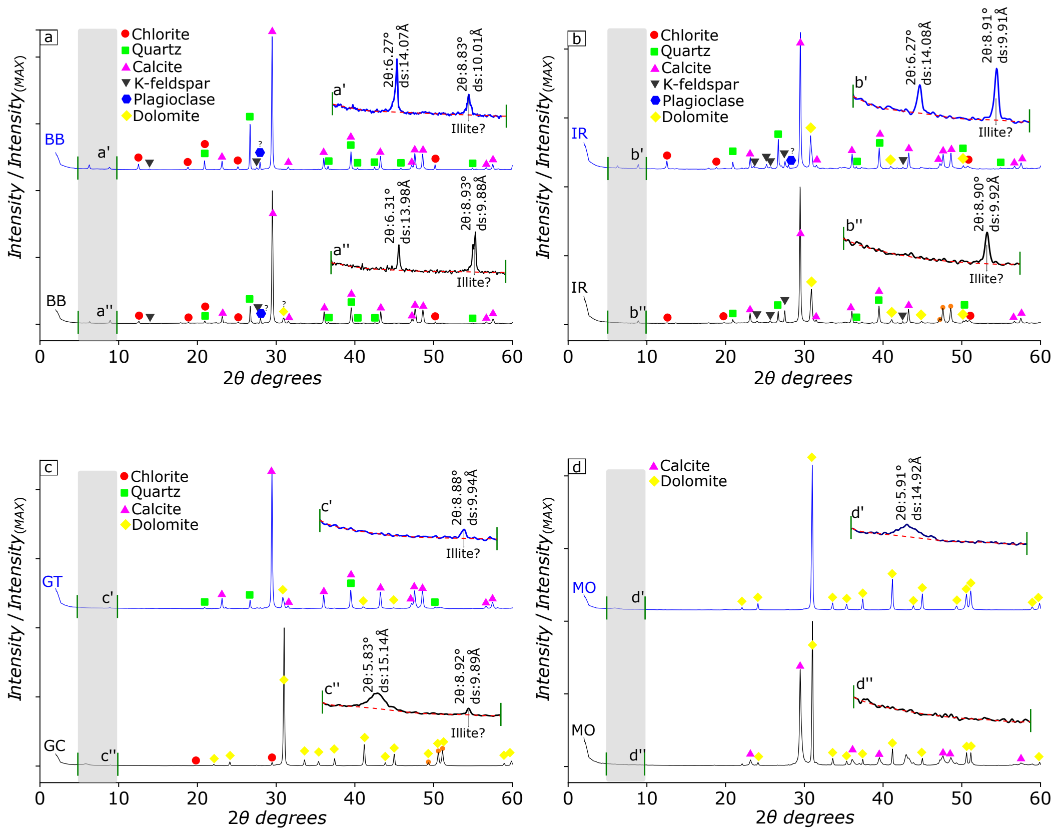

Figure 9. XRD diffractograms of samples from the Bambuí (a), Irecê (b), Guia (c), and Mirassol d'Oeste formation (d). Diffractograms are coloured following the sample names (two per unit). The shaded grey marks the expanded areas between $4 - 10°$ (2θ) shown in the upper right of each diffractogram (e.g., a' and a" are the expanded areas for BB-6 and BB-12 samples, respectively) to highlight the occurrence or lack of the $10\mathring{A}$ peak of illite around $8.9°$ (2θ).

($14\mathring{A}$) compared to chlorite, which might vary due to liquid-phase adsorption ($9.6 - 21.4\mathring{A}$) (Tucker, 2001), and also because if illite is authigenic the transformation may not have been complete, and some residual smectite may remain (either isolated or intercalated with illite layers).

A common behaviour for Bambuí, Irecê, and Guia Formation samples is the occurrence of a peak around $8.9°$ (2θ). These peaks have a very small intensity compared to the major constituents of the samples but are distinct from the background signal (Figure 9). Lattice spacing values of such peaks are near $10\mathring{A}$, which is an indication of the presence of illite-like clay minerals (Patarachao, 2019; Tohver et al., 2006). Interestingly, none of the samples from the Mirassol d'Oeste formation showed the presence of such a peak, indicating its absence or only a trace amount concentration. Regarding remagnetisation due to clay diagenesis, Font et al. (2006) had already suggested that Guia limestones remagnetisation could have an important role in the formation of authigenic magnetite. Now, our data supports such observation by showing the lack of detectable amounts of illite in the Mirassol d'Oeste formation. Besides, the role of Fe-rich smectite-illite transformation and the growth of authigenic magnetite had not been discussed yet for the Bambuí and Irecê basins as well.

After separation of the clay fraction, both samples of the Sete Lagoas and Salitre Formation optimisation returned a good fitting of Gaussian curves within the peak signatures of illite

($\approx$ 9), yielding quite similar KI indexes of 0.14° and 0.13° (Figure 10a,b). These values indicate a high crystalline index, coherent with low greenschist metamorphic facies (epizone) (Mählmann & Frey, 2012). Although deformation is recognised in the borders of the Bambuí group as a consequence of the Araçuaí and Brasília belts (Moreira et al., 2020), the area from which samples studied here were collected are derived from the stable cratonic region (Chemale et al., 1993).

The results reported here indicate that even if the area was not disturbed tectonically, they could have been exposed to temperatures as high as 350°, which is the limit of the the epizone. These are conditions far apart from diagenetic environments, and if the correlation between remagnetisation and illite generation is confirmed, it indeed points to the remanence of Bambuí rocks as non-diagenetic. Smectite-illitisation requires not only temperature but an input of K^+. The dissolution of K-feldspars in these rocks can serve as an in-situ potassium source for illitisation. However, hydrothermal percolating fluids can also work as triggers for illitisation. In the Salitre Formation, $\delta^{13}C$ and $\delta^{18}O$ data have been interpreted as indicatives of the percolation of external fluids of a hydrothermal nature (Couto, 2020). Ethylene glycol treatment for the BB sample induces a slight increase in the FWHM but causes a considerable displacement after calcinating at 550° (*Supplementary file*, Figure S2a). Ethylene glycol penetrates the interlayer spaces of smectite leading to the formation of a two-layer structure (Szczerba et al., 2014). This indicates that not very significant I-Sm structure persists in the Bambuí-sample. That is supported by a crystalline index, pointing out an ordered sequence mostly composed of illite layers (Lanson et al., 2009). For the IR sample, the illite peak suffers almost neglectful changes, indicating a purer illite content. Besides illite, XRD data (bulk samples) indicate peaks at 6.27° for the Sete Lagoas and Salitre Formations. If these were related to smectite, it would be contradictory to find such crystalline illites. However, none of their peaks (of BB and IR samples) swelled to 17 Å when using ethylene glycol treatment, as would be expected if these peaks were attributed to smectite (Szczerba et al., 2014), instead, they are here interpreted as chlorite peaks.

For the Guia Formation, the results are distinct for the two terranes: those over the Amazon Craton (GT) yielded a KI value of 0.25° (Figure 10b), while the sample over the Paraguay belt (GC, Figure 10d) yielded a much higher index 0.11°. While GT samples indicate transitional conditions from mid-to-high anchizone, representing incipient metamorphic conditions, GC is located at similar conditions to the Salitre and Sete Lagoas Formations. These results are coherent with illite crystalline indexes for the transitional region of the Amazon Craton to the Cáceres region (Alvarenga, 1990). The behaviour after ethylene glycol saturation for the GT illite peaks indicates an I-Sm structure (*Supplementary file*, Figure S2c) while the GC sample is more similar to Bambuí, suffering no considerable changes. Unfortunately, the previously observed 15.14$\mathring{A}$ peak (Figure 9c) was not further detected after carbonate dissolution.

Not only the presence of illite in all remagnetised units is a piece of important information for gathering a strongly based hypothesis for the process responsible for remagnetizing carbonate units throughout the west Gondwana, but its crystallinity also offers hints on the palaeotemperature conditions these rocks were submitted. Mainly because these rocks bear distinct magnetic minerals with statistically indistinguishable paleomagnetic directions, but because temperatures found in the anchi/epizone kinetically favour the formation of monoclinic pyrrhotite (present at the Salitre, Sete Lagoas and Guia Formation).

4.3 Microscopic data

4.3.1 Petrography

Petrographic observations in this study are used to support bulk characterisation of XRD data. They are specially important to select the regions where SEM-EDS and micro-XRF/XAS were further analysed.

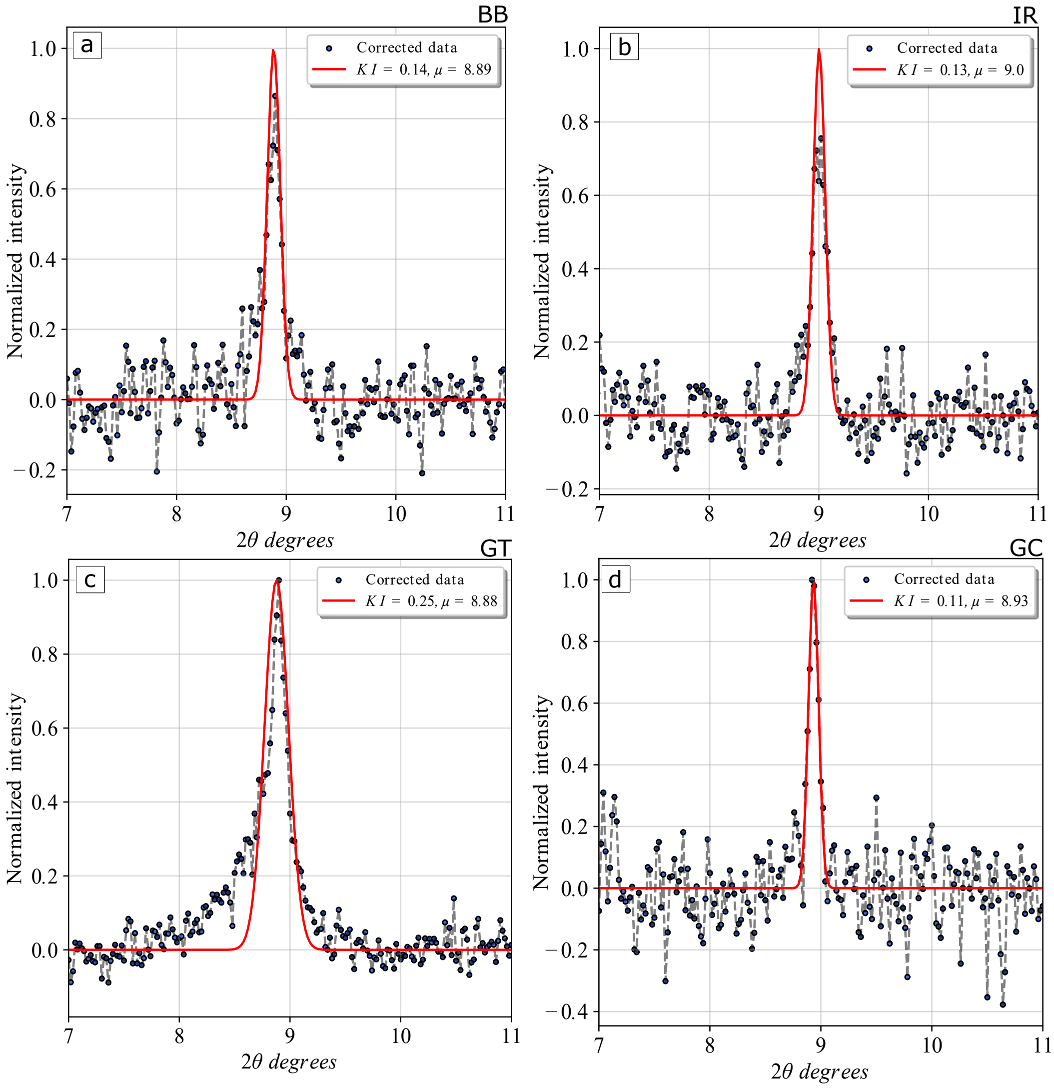

Figure 10. XRD experiments after carbonate dissolution of samples from Sete Lagoas (a), Salitre (b), and Guia Formations (c,d). Corrected data refers to XRD background subtraction. Fitting of Gaussian components at the illite peaks ($\approx 9^{\circ}$) was performed to sequentially calculate the Kübler index ($2\sqrt{2ln2} \cdot \sigma$), where σ is the dispersion around the mean.

Bambuí samples are essentially argillaceous micritic limestones (Figure 11a). There is no direct evidence of microfossil or bioturbation features. Embedded in the matrix, there is a considerable amount of clay minerals, whereas detrital grains include very thin particles (anhedral ones, $< 0.075mm$) of orthoclase and quartz. The latter, although rare, exhibits undulose extinction. Dolomite eventually appears as euhedral grains ($< 0.075mm$), which indicates localised dolomitisation. Calcite veins (0.1-0.25 mm of thickness) crosscut the micritic matrix (Figure 11b), showing discrete signs of border dissolution. Opaque minerals are mostly randomly distributed throughout the matrix, the subhedral grains varying in size from 0.05-0.075 mm and anhedral (more rounded ones) reaching up to 0.30 mm. However, thin ($< 0.1mm$) euhedral grains occur within calcite veins (sometimes recognised as magnetite due to their characteristic cubic habit) which might indicate their contemporaneity.

Irecê samples are even more enriched in clay minerals, these differ from the Bambuí samples in the level of opacity, sometimes showing green/brownish colours (Figure 11c), possible evidence of their incipient chloritisation. They are argillaceous dolomitic limestones, with portions enriched in micrite and other portions enriched in intraclasts. These intraclasts are euhedral to subhedral grains of dolomite (0.1-0.15 mm) (Figure 11d), with interference colours distinct from the calcite forming the matrix. Although thin ($< 0.075mm$) subhedral grains occur, opaque more constantly appear as anhedral ($\approx 0.25mm$) particles, very often associated with clay minerals.

As previously discussed, Guia samples have suffered percolation of hydrocarbon fluids. These are observed as strips, irregularly percolating through the micritic matrix (Figure 11e) in Cáceres samples (GC), whereas it follows the parallel planes in Tangará samples (GT). These limestones are also enriched in clay minerals, most mixed with micrite. Euhedral dolomite grains are, however, present in the samples as well (up to 0.1 mm). Anhedral grains of orthoclase (0.1-0.2 mm) and quartz (0.1-0.15) are found frequently in contact with hydrocarbon, both yielding strong undulose extinction. Opaque grains are widely spread through the matrix, more frequently euhedral in a cubic habit (0.05-0.1mm). Rocks from the Mirassol d'Oeste formation are dolomitic limestones, with a considerable amount of clay content (such as the remagnetised units described above). Large anhedral crystals of calcite (0.25-0.75mm) are randomly located in the matrix (Figure 11f), with no evidence to help understand whether they have grown during diagenesis or were deposited together with the matrix. Quartz grains also occur with a considerable frequency, with a range of sizes (0.1-0.50mm), marked by an undulose extinction. Anhedral opaque grains ($\approx 0.1mm$) are rarely present, with no clear association with other minerals in rock fabric.

Calcitic veins percolating the samples of the Bambuí are important evidence of the transport of fluids in a sin/post-cementation scenario. These fluids, either intrabasinal or allochthonous, could disturb local thermochemical stability and induce the transformation of iron-bearing minerals (which might explain the presence of opaque minerals within the veins). Regions of well-formed dolomite grains in the micritic matrix of Irecê samples are a probable result of dolomitisation. Dolomitisation might occur in both solid (late-diagenetic/post-sedimentary) or untied limestones (early diagenetic/sin-sedimentary), achieved only by the presence of a solvent adding Mg-ions to the rock (Haldar & Tišljar, 2014). As most of the rock is dominated by micrite, the dolomites in the Irecê are probably a result of a post-sedimentary fluid percolation.

These pieces of evidence of fluid percolation are important for considering the illitisation of smectite as a central hypothesis in the remagnetisation of these carbonates. Firstly, because micropetrographic observation confirms an important presence of clay minerals within the matrix of these carbonates, and secondly, because illitisation itself requires an input of K^+ that could be carried by it. Detrital feldspar is in thermodynamic disequilibrium with meteoric waters, undergoing thorough dissolution processes in all diagenetic regimes, including when entering in contact with acid waters charged with CO_2, or organic acids derived from biodegradation of oil (Morad, 1978). Nevertheless, the same is relevant for the samples of Guia formation, where hydrocarbon percolates through the rock. Although

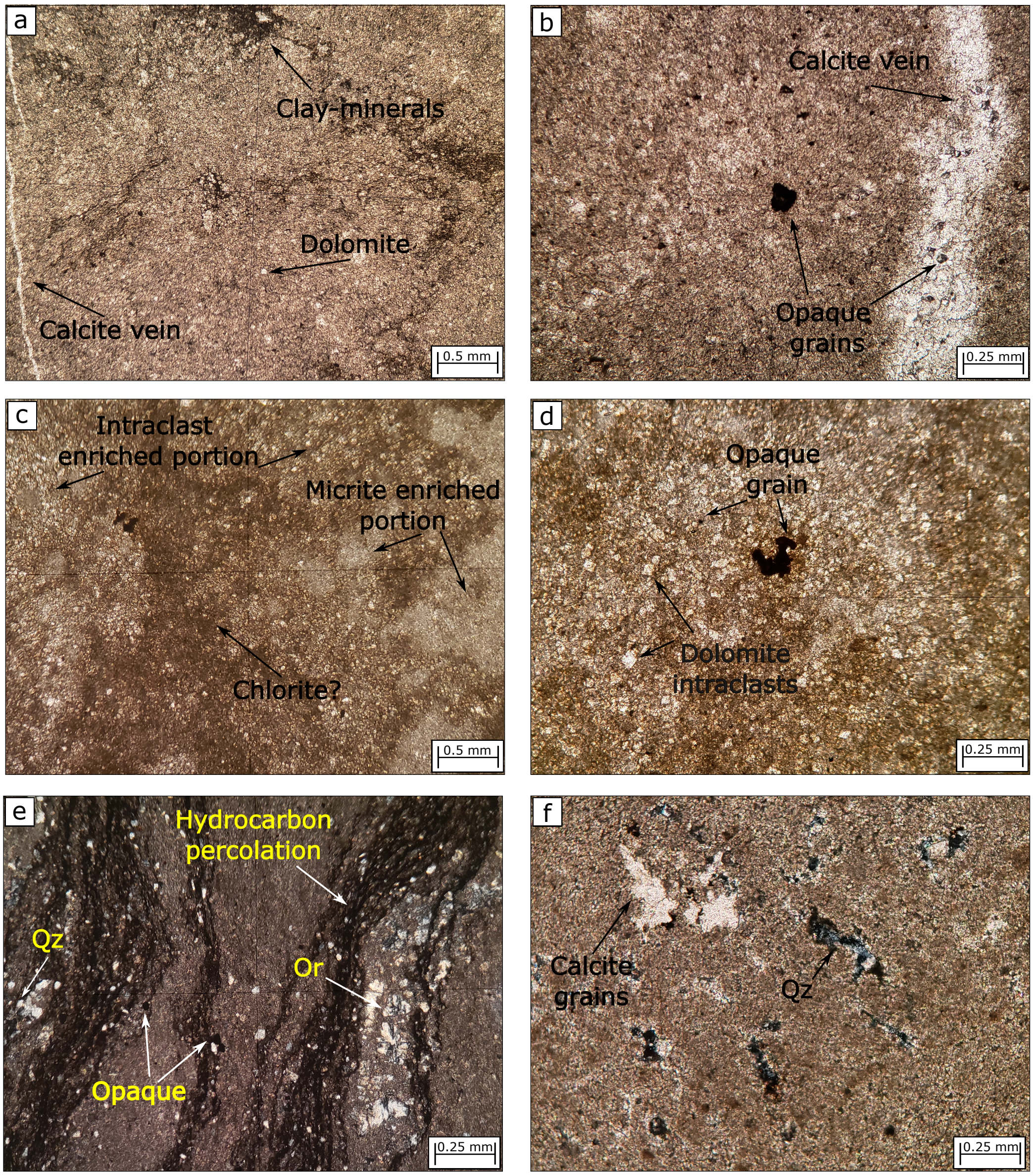

Figure 11. Thin sections (30μm of thickness) of carbonate rocks under polarised light. Sete Lagoas (a, b), Salitre (c,d), Guia Formation (e) and Mirassol d'Oeste formation (f). All these samples are enriched in clay content, which confirms the previous observation of important paramagnetic contribution to magnetic hysteresis and, also, the XRD data.

there are clear signs of fluid percolation in the Mirassol d'Oeste samples and they are also enriched in clay content, their texture is more "homogeneous" compared to the examples of the Guia Formation that were investigated. A commentary is also necessary on the opaque minerals observed in thin sections, since if these are ferromagnetic phases (l.s.) they would be in the MD range. Most of these anhedral grains are probably from a detrital origin, while more euhedral ones could have resulted from sin/post-diagenetic processes.

4.3.2 Scanning electron microscopy with energy dispersive X-ray spectroscopy (SEM-EDS

A first and textural observation is the lack of microporosities, which might indeed indicate a high degree of compaction (as suggested by their tenacity, previously observed in sample preparation methods) and partial recrystallisation reached in low-grade metamorphic conditions. Iron-bearing minerals are distributed throughout the thin sections, dispersed within the matrix. The largest concentrations of iron are in single-elementary regions (with the exception of oxygen), indicating these are dominant phases as iron oxides. There are large anhedral (probably MD) grains, spread in the carbonate matrix. Confirming petrographic observations, most of the carbonate material in all the studied samples is calcite. Dolomite is more frequent in samples of the Salitre Formation. A large amount of aluminosilicates is present in the three remagnetised units. Based on petrographic and XRD data, one can assume these to be smectite, illite, chlorite, or K-feldspar. Therefore, it is possible to segment the occurrence of these aluminosilicates based on the presence of Al, Si, Mg, Fe, and K: (R_i) regions with the presence of both Si, Al, Fe (or Si and Al only) and depleted in Mg and K (Figure 12a,c); (R_{ii}) regions with the presence of Si, Al, Mg, Fe but depleted of K (Figure 12b); and (R_{iii}) regions gathering Si, Al, K but depleted of Mg and Fe (Figure 12b). Both chlorite and smectites are aluminosilicates that may contain Fe and Mg in their structure, so regions (R_i) and (R_{ii}) could correspond to such phases. In contrast, K-feldspar and illite chemical signatures would match region (R_{iii}), but I-Sm structures could show all these elements in their spectrum (depending on the degree of illitisation).

Observations show a strong spatial correlation between aluminosilicates and iron oxides and sulphides. In examples like in Figure 12b, the proximity of clays and iron oxides could even be a direct proxy for the crystallisation of magnetic minerals due to smectite illitisation. The texture of the iron oxide particles is usually rounded, with some examples of subhedral habits, and diameters smaller than 1000 nm. Iron sulphides usually occur as small isolated particles (not larger than $2\mu m$), especially in the Bambuí (*Supplementary $file$*, Figure S3a) and Irecê (*Supplementary $file$*, Figure S3a) samples. Framboids frequently occur in the Guia Formation, as euhedral cubic crystals ($<$ 1000 nm) in between clay layers (*Supplementary $file$*, Figure S3c). In the last case, percolating hydrocarbon might trigger smectite-illitisation by carrying K^+ from dissolved K-feldspars, and with strong inputs of hydrogen sulphide within and the releasing as Fe^{2+} from clay-transformation, the nucleation of pyrite and its framboid aggregation will occur.

4.4 Synchrotron X-ray fluorescence (XRF) and X-ray absorption spectroscopy (XAS)

For all the studied samples, calcium, iron, and potassium characterised the main constituents of the regional XRF spectrum (*Supplementary $file$*, Figure S4d). Dark regions within the maps are composed of elements invisible to the detectors (*Supplementary $file$*, Figure S4a,b,c). In this case, this element is most likely silicon, since (i) its emission energies ($K\alpha \approx 1739.98ev$) are below the spectroscopic range of the CARNAÚBA; (ii) the thin sections are attached to a silica plate (of 1 cm^2); and (iii) the high-energy X-ray beam penetration depth completely trespass the 30 μm thickness of the samples, which also differs this data from other analytic methodologies, like ordinary EDS, since it receives signal not only from superficial particles but also for those in depth.

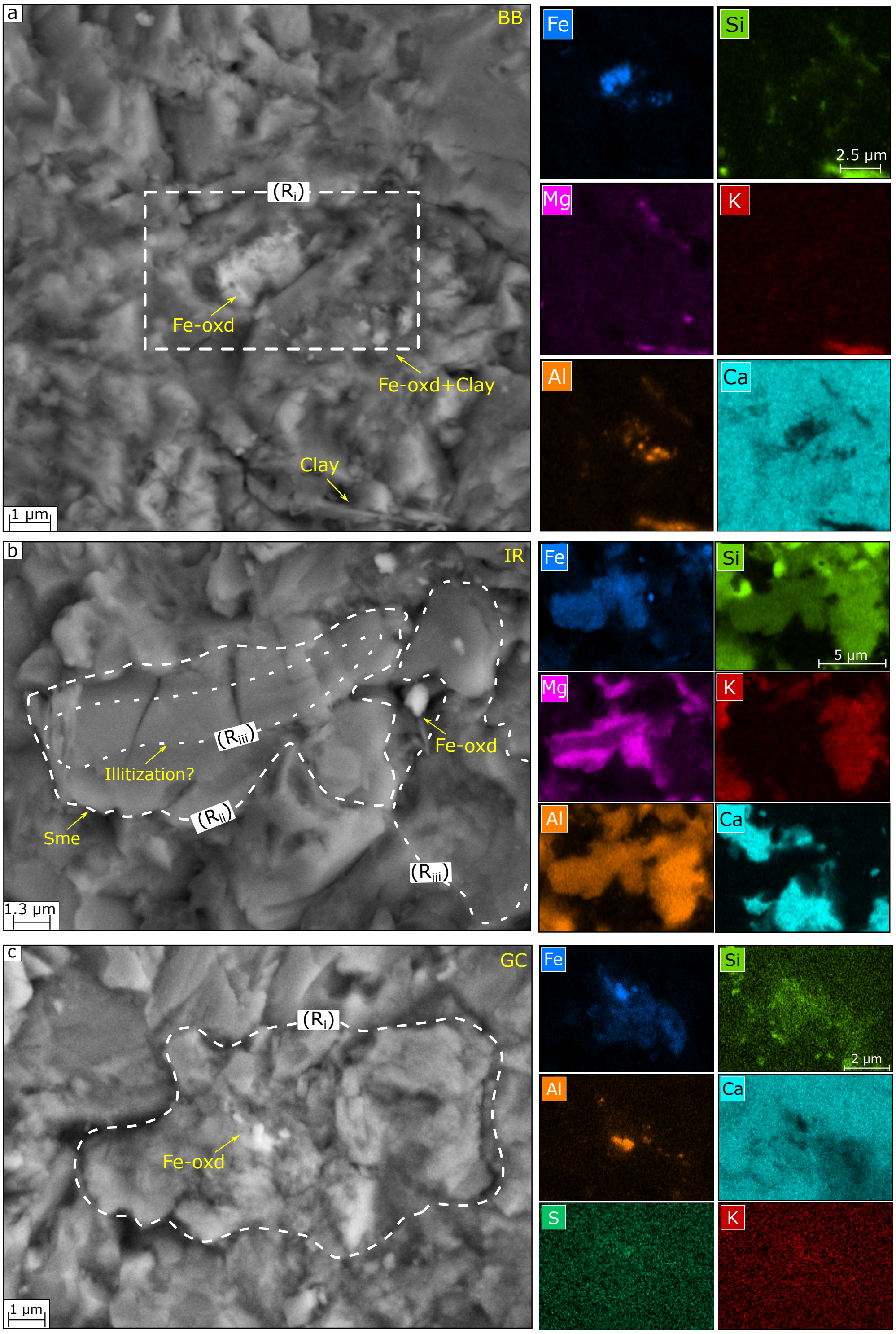

Figure 12. SEM (SE-mode) images showing the occurrences of iron oxides (Fe-oxd) near aluminosilicates in samples of the Bambuí (a) and Irecê basin (b), as well as in Guia Formation (c). The right-column images are EDS chemical maps with the same target in the left column. R_i, R_{ii}, and R_{iii} highlight the chemically different occurrences of the aluminosilicates (smectite, illite, chlorite) and/or K-feldspar (check SEM section for clarity).Sme: smectite.

Besides the importance of detecting "iron islands" as a marker of the presence of possible ferromagnetic grains (previously detected through the magnetic mineralogy experiments), most of the potassium is spatially correlated to these occurrences as well. Comparing this data to previous XRD and petrographic data, potassium should be related either to the clay minerals from the rock matrix or to K-feldspar. Once again, these are both important correlations to associate the remagnetisation of these units to smectite-illitisation, even if paired with mechanisms (such as hydrocarbon percolation, in the case of Guia samples).

Following the XAS data, for the Bambuí example (Figure 13a), a rounded particle in focus is shown to decrease iron concentration from the centre towards the border. Its pre-edge region in XAS (Figure 13a'), also present in the other samples evaluated through XAS analysis, arises from $1s \rightarrow 3d$ transitions present in K-edges of first-row transition metals (Penner-Hahn, 2003; Shulman et al., 1976). The rising-edge region does not entirely match the spectrum of bulk phases of magnetite, maghemite, or haematite. Energy shifts of the absorption threshold occur due to the distinct Fe-O bond lengths, so local geometry influences the chemical sensitivity of XANES (Piquer et al., 2014). For this specific particle, the rising edge and central peak more strongly match with maghemite. Since iron seems to diminish from the centre towards the border (Figure 13a), this might indicate a core-shell structure, where a preserved magnetite is surrounded by a maghemite rim. This particle would then be within the theoretical PSD range of magnetite, while its morphology would point towards a diagenetic origin. This is also evidence of an isolated ultrafine particle in the rock matrix, that would contribute to a central ridge in FORC diagrams. And more importantly, it is a direct observation of a magnetic mineral within the stable PSD range (Nagy, 2017), capable of maintaining a very stable remanence and a probable product of alteration chemical remanence (a-CRM) after an in-situ crystallisation.

For the example shown for the Irecê sample (Figure 13b), subhedral and irregularly shaped particles of around 1000 nm yield a XANES spectrum whose rising edge and central peak match with magnetite. These nanoscopic particles are dispersed within an iron-bearing net, possibly iron-bearing silicates. The narrow peak (Figure 13b') is a common "white-line" feature, which indicates an intense absorption in the near-edge (Penner-Hahn, 2003). These are interesting results that demonstrate that even if haematite or pyrrhotite may give important contributions to the remanence of these rocks, very thin magnetite particles are present in the Salitre rocks as well. In this case, we interpret this as a probable growth chemical remanence (g-CRM), due to it's chemical purity. Yet again, these ranges are still within the stable range of PSD grains and are mostly the ones bearing a stable remanence.

For the Guia sample, although iron oxides are more common, we show an example of a globular-shaped particle (Figure 13c) yielding an XAS spectrum matching with pyrite (FeS_2) (Figure 13c'). Right ahead of the pre-edge region, there is an increase of energy before the main peak, which has also been detected in the nanoparticulate phases of FeS (Matamoros-Veloza, 2018). Nevertheless, the match between the reference material and the data supports the interpretation of such a particle as a pyrite framboid as their presence is common in sedimentary systems with hydrocarbon (Machel, 2001).

Collaboratively, the utilisation of highly precise XRF and XAS data forms a potent tool for investigating remanence-bearing minerals in weakly magnetic rocks. In addition to identifying grains falling within the vortex state dimensions for magnetite, as observed by Nagy et al. (2019) (Nagy, Williams, Tauxe, & Muxworthy, 2019), our analysis reveals even smaller mono-elementary regions enriched in iron dispersed throughout the samples (as in Figure 13b). While the morphology of these smaller grains is challenging to discern due to experimental constraints, they likely signify even smaller particles within the thin section, approaching the limits of PSD with SD states. In the case of remagnetised carbonates, this innovative approach provides a new means of confirming the presence of clay minerals surrounding authigenic ferromagnetic minerals and verifying their respective phases.

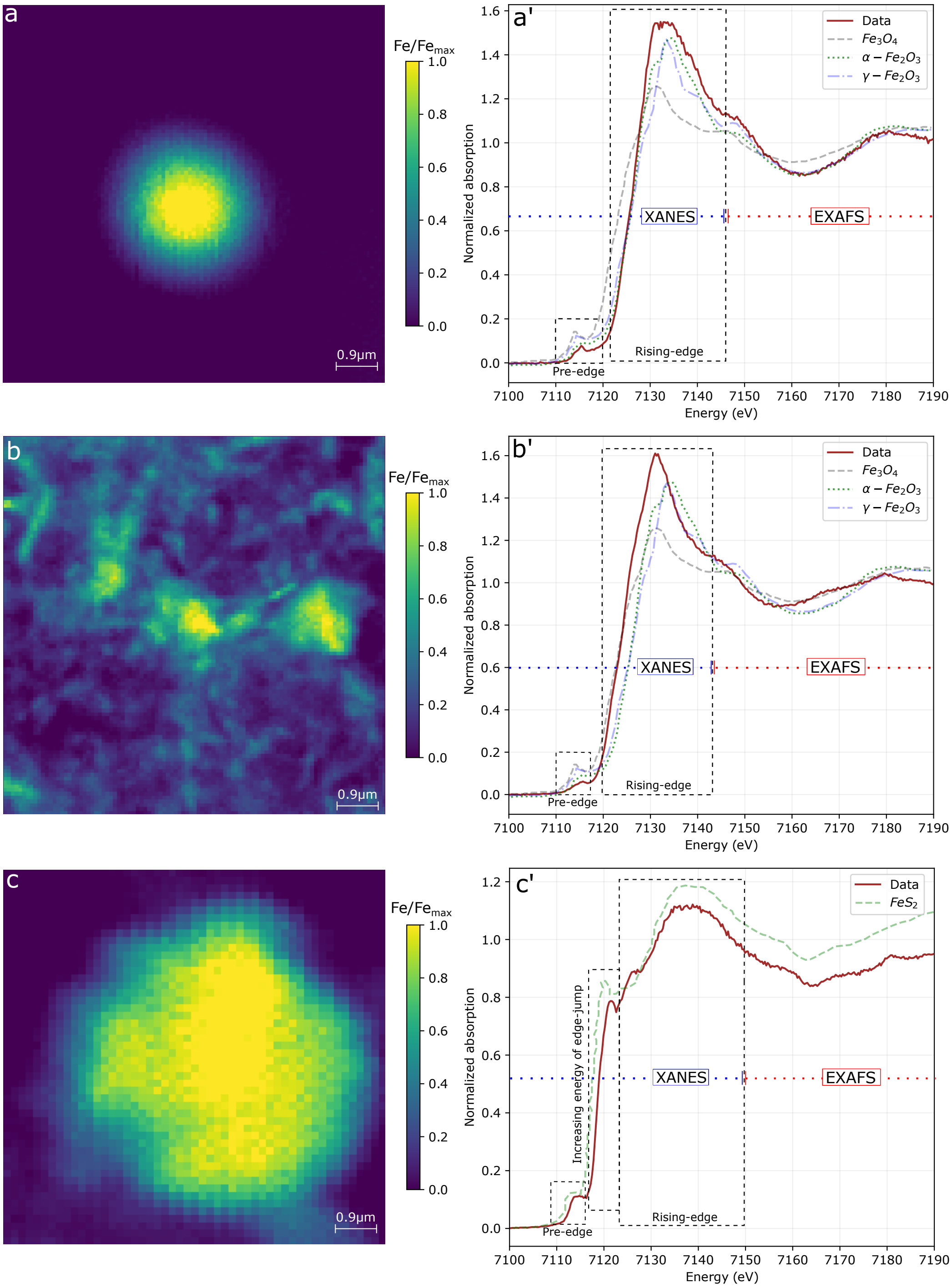

Figure 13. Compositional maps of Fe ($K\alpha \approx 6400eV$) for the Bambuí, Irecê, and Guia samples (a,b and c, respectively). Normalised XAS spectrum collected in fluorescence mode around the iron activation energy ($E_0 \approx 7112eV$) are shown in the right column (a',b' and c'), and compared to data extracted from literature: for magnetite, maghemite, and haematite from Piquer et al. (2014); and pyrite from Ravel (2013).

4.5 TGA-QMS

The examination of samples from the Araras Group adds a layer of intricacy to our understanding, introducing complexity arising from the interplay of hydrocarbon percolation. This process opens avenues for crystallisation through organic biodegradation processes (Emmerton et al., 2013). Notably, the Mirassol d'Oeste samples exhibit a consistent presence of stable detrital remanent magnetisation (DRM) components (Trindade et al., 2003; Font et al., 2005) while the overlying Guia formation bears only a secondary remagnetised component. In addition, Mirassol d'Oeste samples offer evidence of some degree of hydrocarbon percolation Júnior et al. (2016). It is important, therefore, to discern the extent of organic matter and hydrocarbon content within them. Our exploration extends to a TGA-QMS analysis, aiming to not only verify the presence but also quantify the pivotal amount of volatile components (such as CO_2, SO_2, SO_3, and H_2O) in these samples.

H_2O is lost throughout the whole range of the analysed temperatures ($30 - 600°C$) for all of the samples, following a linear trend, which is attributed to the loss of structural water (OH) from clay minerals. The most important mass loss event is related to CO_2 release, which occurs in a similar range for samples enriched in bitumen (Figure 14',c') with two major peaks, one at 50°C and the other at $\approx 550°C$. This is a common range for bitumen decomposition with peak liberation of CO_2 (Zhao et al., 2012) at $550°C$. Thermal decomposition of calcite starts only around $700°C$ (Karunadasa et al., 2019) while dolomite decomposition occurs between $700°C - 750°C$ (Gunasekaran & Anbalagan, 2007). Therefore, the CO_2 loss we show for these samples is related to none of these processes. More importantly, TGA-QMS analysis indicates that bitumen is also present at the base of the Mirassol d'Oeste formation, which was also previously reported by the work of Júnior et al. (2016). However, when looking at the ion current normalised by the individual mass of the samples (CO_2/mass at the CO_2's major peak), $MO_{transition}$ and GT samples have twice the mass of bitumen of MO_{base}. Nevertheless, this confirms that bitumen percolation was not so efficient in the base of the Mirassol d'Oeste formation, and that is probably why detrital remanence was preserved.

SO_3 emissions were not detected in the TGA-QMS analysis, but SO_2 is detectable in the GT and $MO_{transition}$ samples (Figure 14b',c'). For GT samples, SO_2 emissions occur between $420-540°C$, while $MO_{transition}$ samples are between $\approx 400-430°C$. We interpret these as related to pyrite. In atmospheres containing high amounts of O_2 in temperatures $< 800K$, pyrite will directly oxidise, but in a low-content O_2 atmosphere (or higher temperatures) it will be oxidised firstly to a mineral of the troilite group (pyrrhotite or troilite, (G. Hu et al., 2006)). Between $400 - 600°C$ (in atmospheric air) pyrite will decompose to form FeS and S, so S further combines with oxygen to form SO_2, and FeS will sequentially react with oxygen gas to form iron sulphate (Zunino & Scrivener, 2022). TGA analysis performed during the combustion of pyrite-bearing shales reported SO_2 emissions between $400-430°C$ (Labus, 2020). The grain size of pyrite particles can also influence the range of SO_2 emissions because the thermal decomposition will strongly influence the kinetic phenomena. Emissions of fine particles ($< 45\mu m$) should start around $320°C$, stopping around $540°C$, while larger particles' ($< 200\mu m$) emissions begin around $450°C$ (stopping around $550°C$, (Zumaquero et al., 2021). Pyrrhotite decomposition in GT samples should be contained within the higher temperature SO_2 emissions, but since these are too restricted in $MO_{transition}$ samples they are probably not in the detection range.

5 Discussion

5.1 Remagnetisation fingerprints (?) of South American Neoproterozoic carbonates

Classical paleomagnetic/paleointensity techniques apply magnetic measurements to infer the composition, size distribution and remanence of macroscopic (bulk) samples. There are

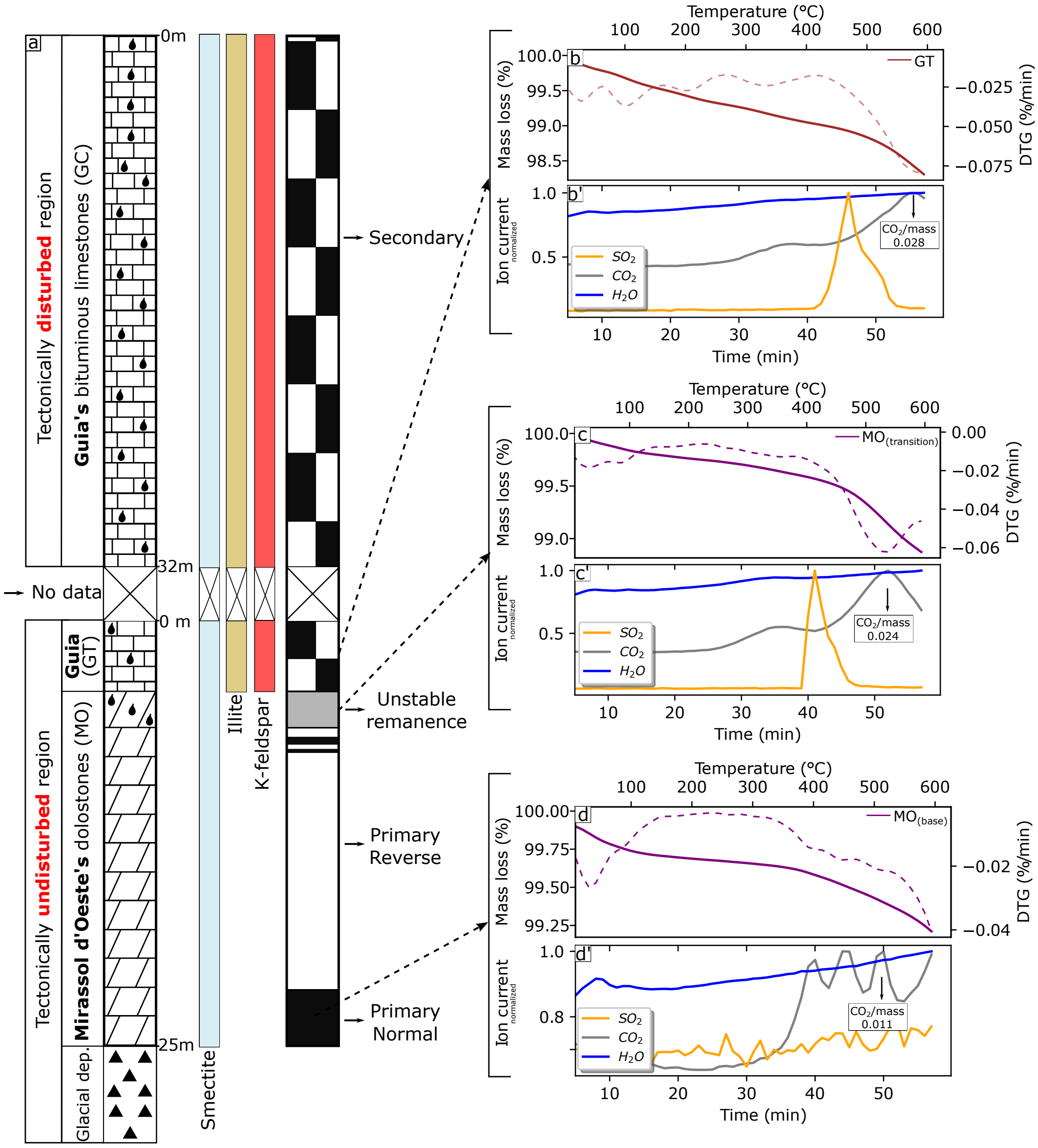

Figure 14. a) Stratigraphic profiles of the Araras Group over the deformed (Paraguay belt) and underformed regions (Amazon craton), modified from Trindade et al. (2003); Font et al. (2006). Blue, ocher and red bars indicate where the presence of smectite, illite and K-feldspar (respectively) was detected through either DRX, petrography, or SEM analysis. The polarity chart shows that Guia Formation only yields a remagnetised component, while percolation of bitumen in the upper section of the Mirassol d'Oeste formation ($MO_{transition}$) has completely erased stable remanence. In the right column, thermogravimetric analysis coupled to a Quadrupole Mass Spectrometer (TGA-QMS) shows the mass loss (%) of the basal stratum of b) Mirassol d'Oeste (MO_{base}), its bitumen-enriched portion c) ($MO_{transition}$) and the overlying d) Guia Formation (GT). Normalised ion current flow (b',c', d') allows the detection the volatilised emissions throughout the heating process.

many advantages to using bulk samples, which include: (i) avoiding heterogeneous characteristics that might not be representative of the larger sample; and (ii) data acquisition techniques that are relatively fast, simple, sensitive to even trace amounts of magnetic minerals, and representative of the overall behaviour of an assemblage of grains. Nevertheless, this approach may mask important magnetic phenomena or lead to erroneous interpretations due to the ambiguity of the techniques.

Distortion in hysteresis, IRM and ARM curves is very often present in natural samples, often due to the effect of a mixture of grains with different magnetic properties, which commonly rely on unmixing techniques to better understand their component characteristics (U. Bellon et al., 2023; Egli, 2003; Maxbauer et al., 2016). Populations of grains with different magnetic properties might arise either for groups of particles with different compositions or for particles with the same composition but in a distinctly different domain state. When we consider any geological event triggering the growth of new magnetic grains, it is expected that some grains will grow beyond their blocking volume (VB) where their magnetic state is stable, and so produce a stable growth-chemical remanence, whilst another population of grains within the sample might still not have grown beyond the superparamagnetic (SP) threshold, where the grains are not capable of holding a magnetic recording. It is very logical, therefore, to find an important contribution of SP particles in remagnetised carbonates that often contain significant quantities of SP particles, and so it is important to correctly identify and quantify such SP particles within the total population of magnetic grains.

SP particles can strongly influence magnetic hysteresis (Tauxe et al., 1996) and low/high-frequency susceptibility (Hrouda et al., 2013). However, their quantification is likely problematic for both of the techniques. Mixtures of distinct coercivity components can also cause both potbelly and wasp-waisted hysteresis (U. Bellon et al., 2023; Tauxe et al., 1996), and, but there are many possible mineral alteration pathways by which a remagnetised carbonate could create more than one magnetic mineral in sufficient quantity to influence the samples' bulk magnetic properties. When we observe hysteresis parameters in the Day plot (Figure 6) compared to other compiled remagnetised carbonates, our data do not necessarily match with the "remagnetised fingerprint", even though they are distorted hysteresis loops. What all of the studied samples have in common are properties that match with the PSD state.

The PSD state describes a great variety of magnetic structures limited between the SD and MD states. It can also be broadly defined in terms of single and multi-vortex states often characterised by magnetisation helicity within a grain. From a uniform SD state, the magnetic domain states evolve from a flowering state to a single-vortex (SV) and further on to a multi-vortex (MV) state, after which it becomes energetically favourable to form large uniformly magnetised regions separated by domain walls in what is known as multidomain (MD) states (Nagy, Williams, Tauxe, & Muxworthy, 2019). A long-held premise of palaeomagnetism is that SD grains contain stable remanences on the scale of billions of years (Butler, 1992). However Nagy (2017) have shown, through micromagnetic models, that there is an unstable magnetic zone (UMZ) whose grain size range approaches 50% of the SD size range. Within the vortex state, there are many possible domain configurations, the main ones are described as hard-aligned SV (HSV) and easy-aligned SV (ESV) states. Although the ESV magnetic structure can yield stabilities exceeding that of SD (Nagy, Williams, Tauxe, Muxworthy, & Ferreira, 2019), HSV states are often unstable, even at room temperature (Nagy, 2017). For equidimensional octahedral grains of magnetite, the UMZ occurs for grains sizes of 84-100 nm, but this range will vary with both mineralogy and morphology (Wang, 2022; Nagy, Williams, Tauxe, Muxworthy, & Ferreira, 2019).

Particles within the UMZ will suffer not only a decrease in thermal stability, but other magnetic properties will change as well. For instance, coercivity is largely reduced and the magnetic susceptibility can be as high as those of SP particles (Wang, 2022; Nagy, Williams, Tauxe, Muxworthy, & Ferreira, 2019). These results might have a profound implication for the interpretation of bulk magnetic properties of remagnetised carbonates since the effects of distorted hysteresis loops and the frequency-dependent susceptibility of grains within the UMZ could be erroneously interpreted as the result of SP grains. Because the UMZ can occupy a large range of sizes between the SD and ESV states, a significant amount of authigenically grown grains could be magnetically unstable. In addition, chemical alteration processes (like maghemitisation) that create a core-shell structure within the magnetic particle will reduce the dimension of fine-grained parent particles as the daughter phases grow, thereby moving the parent phase to within the UMZ zone (Ge et al., 2021). That could be the case for grains as those observed for the Bambuí sample (Figure 13b).

For samples containing multiple types of magnetic minerals, more reliable methods, such as FORC diagrams, are available for inferring domain states. In our investigations, remagnetised carbonates exhibit FORCs indicating a central ridge, attributed to non-interacting single domain/PSD grains (Roberts, 2022). This interpretation is supported by our direct microscopic observations (Figures 12, 13). The frequent distribution towards zero coercivity suggests the likely presence of SP particles. However, the significance of these contributions to the bulk properties of rocks remains open for discussion. Frequency-dependent susceptibility may not be sensitive enough to characterise them accurately (as it is observed in the dispersion of χ_{ON}/χ_{FN} parameters of Figure 5) and is subject to uncertainties in samples with multiple magnetic minerals.

Despite potential reasons linking specific properties of remagnetised carbonate rocks, false negatives might persist. In cases where carbonate rocks only carry secondary components, anomalous properties may not be observed and they might be very similar to primary remanence-bearing rocks (such as in MO samples), as seen in most of our studied remagnetised samples. Nonetheless, combining magnetic properties with other analytical techniques (e.g., high-resolution chemical/mineralogical studies, as demonstrated in our study) can clarify remagnetisation mechanisms and link them to significant geological phenomena in sedimentary basins.

5.2 West Gondwana large scale remagnetisation

Despite employing a multidisciplinary approach to comprehend the characteristics of these rocks, determining the primary trigger for remagnetisation remains a complex task. The remagnetisation event's nature must align with a process capable of impacting vast expanses of land. While fluid percolation seems enticing for such phenomena, it necessitates the carbonate sequences to possess homogeneous porosity and permeability to enable the remagnetisation of entire intracratonic basins within a short time frame. Further, although orogenic fluid percolation may still play a significant role in initiating remagnetisation, the fact that these basins share a remarkably similar mineralogical composition prompts consideration of mineral transformation, specifically smectite illitisation, as a key candidate in this discussion. Regardless, we also must take into account the geotectonic scenario, the final amalgamation of the Gondwana and the Brasiliano orogenies happening throughout the supercontinent (Figure 1a).

Our interpretation considers a diagenetic evolution of these sedimentary basins and sequentially discusses the implications of each particular phenomenon to the growth and preservation of the remanence.

K-feldspars have been detected in all the remagnetised units, either through XRD or through petrographic observation. Likewise, smectite and illite were also present in amounts to overcome diamagnetic (calcite/dolomite) and ferromagnetic signatures in these rocks. Glacial melting is the probably responsible source for the large influx of terrigenous materials in these cap carbonates. K^+ will also be available in the pore waters. Early diagenetic reactions will mobilise ions of sulphur, where nanoprecursors (mackinawite) will likely form, which are known precursors of other iron sulphides (Rickard, 1995). With an increase in temperature, the medium tends to become more reductive and pH values stabilise around slightly acid/to basic conditions (considering an evolution to normal geothermal trend on a sedimentary basin). Any metastable iron-hydroxide of detrital origin tends to be consumed by iron-reducing bacteria (rather than metastable phases, Phillips et al. (1993)) so only the most stable phases of iron oxides are preserved in the sedimentary column. The presence of a minimum amount of $S2-$ in the medium from the consumption of mackinawite and the availability of Fe^{2+} will lead to pyrite nucleation, since its formation is kinetically hindered in such conditions (Rickard & Luther, 2007). When reaching a temperature around 70°C, smectite-illitisation begins (Huggett, 2005) and Fe^{2+} ions are released into the system. In such conditions, authigenic magnetite has the thermodynamic/kinetic conditions to grow and main chemical stability (Pourbaix, 1974). As the intensive conditions (pressure and depth) increase up to the peak of the illitisation reaction (120°), a g-CRM is slowly acquired as the magnetite particles reach their blocking volume in a sin-diagenetic period.

As suggested by: i) their degree of compaction (enough to make any macro-to-nanoporosities be hardly detected); ii) the presence of incipient chloritisation, and iii) the illite KI values (which indicates epizone temperatures), the rocks studied here must have reached low greenschist facies (around 300°). As the diagenetic nature of the processes slowly transitioned towards the incipient metamorphism (anchizone) towards higher temperatures, magnetite still has the thermodynamic conditions to keep its growing process. But after 180°, monoclinic pyrrhotite growth is kinetically (Lennie et al., 1995) and is thermodynamic favoured (Ning et al., 2015) under very similar pH/Eh conditions as those of magnetite. Likewise, if sulphur and iron are in micromolar concentrations, pyrite thermodynamic stability will collapse and its partial/total dissolution will provide the ions so monoclinic pyrrhotite (as well as magnetite, Brothers et al. (1996)) can grow and eventually achieve a g-CRM.

Aubourg et al. (2019) explored the occurrence of magnetite and monoclinic pyrrhotite in clay-rich rocks, specifically shales and slates. The primary objective was to discern the coexistence patterns of these minerals under different temperature conditions, utilising magnetic remanence analysis. Their findings indicated that magnetite and SP-pyrrhotite were simultaneously present within the temperature range of $77 - 128°$. Additionally, at temperatures ranging from $300 - 350°$, MD magnetite coexisted with SD pyrrhotite, while temperatures exceeding 347° exclusively revealed the presence of pyrrhotite. The study suggests that the formation of pyrrhotite may occur at the expense of magnetite and can function as a temperature indicator. It also proposes that rocks of this nature, when subjected to metamorphic conditions, would record the magnetic field due to subsequent denudation processes and cooling down, essentially exhibiting a thermoremanent magnetisation (TRM). However, our samples presented some distinctive characteristics. Petrographic observation and the illite crystallinity index both indicated incipient metamorphic conditions extending well beyond 128° but limited to low greenschist. Furthermore, the palaeomagnetic components obtained from the thermal demagnetisation of the Sete Lagoas, Salitre, and Guia formations (Figure 15a) displayed unique demagnetisation behaviours attributed to both PSD/SD monoclinic pyrrhotite and magnetite, resulting in statistically indistinguishable directions (Figure 15a').

Because the detrital sources in the carbonatic matrix are not homogeneously distributed, different sectors of a macro/micro-region can be influenced by the influx of Fe^{2+}/or S^{2-} (from smectite-illitisation and/or sulphide dissolution) and therefore favour the growth of either one of these ferrimagnetic minerals. If considering pyrite as a source for monoclinic pyrrhotite growth (or even an early formed hexagonal pyrrhotite), its (FeS_2) previous formation rates and distribution (during a previous early diagenetic stage) might harshly vary with small distances because of local homogeneities and the formation/concentration of metastable phases (Rickard & Luther, 2007). A new CRM registered by these ferromagnetic particles could completely overcome a DRM/pDRM in terms of intensity (Kars et al., 2012), explaining why only the remagnetisation component is observed in these rocks.

Although the hypothesis seems to explain the formation of these ferromagnetic grains without the necessity of summoning a problematic process such as orogenic fluid percolation, it does not explain why their characteristic remanence bearing a single polarity produces paleomagnetic poles with such restricted confidence ellipses (Figure 1b) far from the syndiagenetic their ages. Instead, what we further discuss here is not the generation of these particles, but a thermal phenomenon able to lock their remanence in a very effective way.

Palaeotemperature data calculated from the illite crystallinity index (KI) can be paired with the previously published paleomagnetic data (thermal demagnetisation) to propose a thermoviscous component for the remanence observed in these Neoproterozoic carbonates. When looking upon the lower-range blocking temperatures of the components yielded by magnetite (Figure 15a), i.e.: i) $340-360°$ for the Sete Lagoas (BB) samples; ii) $300-340°$ for the Salitre (IR) samples, and iii) 300° for the GC samples, the directional similarity (site means) is noticed as medium-to-high inclination vector with an NNE trend (Figure 15'), which is further confirmed by their paleomagnetic pole positions (Figure 1b).

Since these units held crystallinity indexes indicating an epizone environment, let us consider its lower boundary (300°C) as the peak temperature to which these rocks were submitted. Following Neél theory (Néel, 1955), it is possible to attend that a remanence carrying grain (in these case particles that originally carried a g-CRM) when laboratory heated to an unblocking temperature T_1 along a relaxation time τ_1 would lose its remanence acquired at a given geological time (τ_2) at a T_2 temperature (Pullaiah et al., 1975):

$$\frac{T_2 \cdot l\ n\,(C \cdot \tau_2)}{M_{s[T_2]} \cdot H_{c[T_2]}} = \frac{T_1 \cdot ln\,(C \cdot \tau_1)}{M_{s[T_1]} \cdot H_{c[T_1]}} \tag{5}$$

Ms[T] is intrinsically related to the remanence carrying phases, for magnetite (for example) it is $Ms = M_{s[293K]} - ((T_C - T)/(T_C - 293K))^{0.43}$ (Dunlop & Özdemir, 1997). The microcoercivity of the same magnetic mineral is also temperature-dependent and arises mainly from shape anisotropy and/or magnetocrystalline anisotropy. Microcoercivity arising from shape anisotropy is (i) $H_{c[T]} = \Delta_{N(demagnetizing\ factor)} \cdot M_{s[T]}$, while magnetocrystalline effects are (ii) $Hc_{[T]} = K_{1[T]}/8 \cdot Ms_{[T]} \equiv {Ms_{[T]}}^{7.5}$ (Nagata, 1961; Stacey & Banerjee, 1974; Pullaiah et al., 1975) in which $K_{1[T]}$ is the first anisotropy constant. Because at NTP conditions the shape anisotropy controls the magnetisation in magnetite grains at least 10% elongated, $Hc_{s.anisotropy\ [T]} \equiv Ms_{[T]}$.

By following Pullaiah's approach (Eq. 5), the correspondent viscous relaxation curves (Figure 15b) are calculated, making it clear that if these rocks were exposed to an environmental temperature of 300° for a short period (< 10 years) it would be enough to completely relax their remanence. If we consider a continental context in which the basins were kept warm under low greenschist metamorphic conditions, their remanence would be constantly reset until a temperature-decreasing scenario.

A g-CRM remanence component carried by monoclinic pyrrhotite (which is even statistically similar to that of magnetite) would be easily erased since their blocking temperatures do not surpass 300°. After a temperature drop, these authigenic grains would block their directions again. Similarly, to magnetite, pyrrhotite viscous decay becomes steeper near its Tc (Dunlop et al., 2000), and since none of the samples of the Bambuí, Irecê or Araras' pyrrhotite components showed blocking temperatures smaller than 250° (D'Agrella-Filho et al., 2000; Font et al., 2006; Trindade et al., 2004), the blocking of directions along the environment heat dissipation (even at slow cooling rates) would rapidly occur. There is only a small difference between the characteristic remanence yielded by the pyrrhotite and magnetite components in these rocks, the first one yielding mean site directions with much lower precision parameter (k) and larger confidence ellipses (α95) than the second one.

The paleomagnetic register of pyrrhotite-bearing rocks exposed to metamorphic conditions can officially register the magnetic field as they cool down, but such efficiency of polarity recording is strictly connected to cooling rates (Rochette et al., 1992). In fact, the sequence of thermomagnetic experiments developed by Crouzet et al. (2001) for multipolarity-bearing remagnetised carbonates of the Western Alps confirms that single-domain pyrrhotite can sequentially register pTRMs during slow cooling.

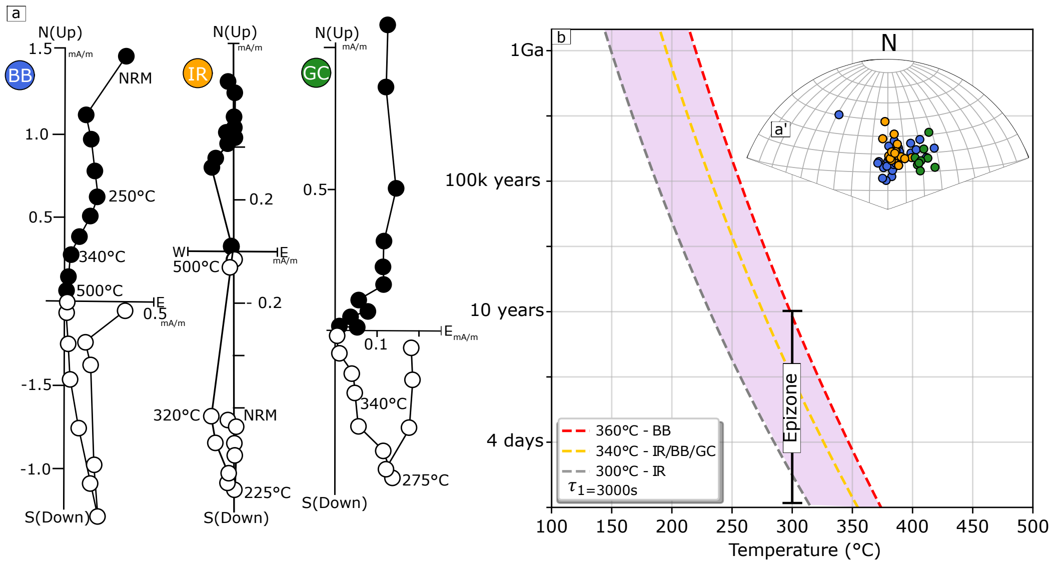

Figure 15. a) Zjiderveld diagrams of thermally demagnetised samples from the Sete Lagoas (BB, D'Agrella-Filho et al. (2000)), Salitre (IR, Trindade et al. (2004)) and Guia in the Cáceres region (GC, Font et al. (2006)). a') Blue, orange and green circles represent site mean directions of the BB, IR and GC units (respectively). b) Pullaiah's nomogram (Pullaiah et al., 1975) for magnetite. Viscous relaxation curves are calculated (Eq. 5) using the blocking temperatures marked with dashed lines. Epizone's lower boundary is where relaxation curves are intercepted by the 300° isotherm.

Distinguishing from remagnetised rocks bearing multipolarity components, Bambuí, Irecê and Guia samples yield only a single polarity component related to pyrrhotite (as well as for magnetite). A thermoviscous overprint of (what originally could be a g-CRM) caused by a heating event and a succeeding cooling could explain the contemporaneity of such components and the large-scale remagnetisation event affecting the whole of Gondwana. The temperature increase from deep diagenetic conditions, up to the anchizone and further to the epizone favours the conditions for monoclinic pyrrhotite to authigenically form.

The most obvious candidates to elevate the temperatures up to low greenschist metamorphic conditions are the collision events of the Brasiliano (Panafrican) orogenies, which culminated in the amalgamation of different terranes to the Amazon and São Francisco Craton during the Late Precambrian – Early Paleozoic (Almeida et al., 1973; Mohriak & Fainstein, 2012). Peak metamorphic conditions related to the closing of the Clymene Ocean and bending of the Paraguay belt event (the portion between the southeast margin of the Amazon craton and the São Francisco Craton to the East, Figure 2b) has yielded a weighted mean age of ca. 528 $\mp$ 36 Ma ($^{40}Ar/^{39}Ar$) (Tohver et al., 2010). Such an event could easily remagnetize the portion of the Guia Formation over the Cáceres region (GT) samples, and offer a diffusion heat source for the nearby areas, where such formation lies undeformed over the Amazon Craton (GT) region that did not reach high KU values such as those over the Paraguay belt. As for the São Francisco Craton, the east bordering Araçuaí belt (Figure 2a) comprises a long magmatic history (630- 480 Ma, Tedeschi (2016); Pedrosa-Soares (2020)), with metamorphic peaks around 580 Ma (Pedrosa-soares, 2007). The Araçuaí belt history yields a characteristic slow cooling of the middle crust, resulting in temperatures of 500°C around 510-500 Ma (Vauchez et al., 2019). The effect of such a high-temperature regime on the nearby orogenic region could explain the epizone conditions described by the illite-crystallinity calculations in both Bambuí and Irecê. Other researchers have already reported carbonates from the

Bambuí as overprinted by a greenschist metamorphism (Caby & Costa Campos Neto, 2022; Misi et al., 2014), including the presence of metamorphic chlorite.

Even so, the fact these distinct units from basins separated hundreds of kilometres apart bear statistically indistinguishable paleomagnetic directions not only requires their contemporaneous heating but a sequential cooling with a very restricted span of time. Early 2000's paleomagnetic works of Trindade et al. (2004) and D'Agrella-Filho et al. (2000) positioned the paleomagnetic poles of these remagnetised rocks around the 520 Ma interval in the Gondwana APW curve. However, when plotted along Gondwana's mean paleomagnetic poles APW curve (Figure 1b) of Torsvik (2012), the directions seem closer to the 460-470 Ma interval. The high-quality poles of West Gondwana, e.g., SAVN (Araçuaí orogen in Brazil, 500 Ma) and CF (Pampia terrane in Argentina, 519 Ma) are far from remagnetised carbonates grouping (Table 1).

Therefore, the blocking of remanent magnetisation in these carbonates could be linked to the Early- to Middle-Ordovician period. The Late-Cambrian/Early Paleozoic marks the termination of Gondwana's assembly and the orogenic collapse of Neoproterozoic belts (e.g., the Araçuaí-Ribeira in the Brazilian Atlantic coast, Alkmim et al. (2006); Pedrosa-Soares et al. (2001); Wiedemann et al. (2002) and the Damara orogen (Southwest Africa, Goscombe et al. (2018)). Although there is a considerable amount of post-collisional magmatism related to this period, the end of the main orogenic activity should lead to the relaxation of the upwardly compressed isotherms (Fonseca et al., 2021). A Paleozoic cooling event is registered in most parts of the West Gondwana. Earliest zircon's AHe and ZHe ages of apatite and zircon crystals from the Neoproterozoic Dom Feliciano belt (South Brazil) show a spread of ages from 472 to 26 Ma, the Ordovician ages implying an exhumation of the crystalline basement. In the Brasília belt, apatite fission track ages (AFT, Fonseca et al. (2020)) indicate a fast increase of cooling ages around 480 Ma, which indicates the exhumation of the basement as well. Reported AFT ages in the São Francisco Craton (Fonseca et al., 2021) show that Early Paleozoic cooling ages quickly increase towards the Devonian, which could be the result of an interplay of interplate tectonics readjustments and erosional process (that could have been enhanced by Late Ordovician glaciation, Torsvik and Cocks (2013)).

If the remanence observed in these units is related to the Paleozoic cooling event, that also explains why only a single polarity would be observed for magnetite/pyrrhotite (components B/C, Figure 15a), even considering such a large continental area), since the Amazon and São Francisco cratons would be in the southern hemisphere (Merdith et al., 2021) in such period, and so these components could be related to the Moyero superchron (Pavlov & Gallet, 2005). Still, considering to prove the Paleozoic cooling event as the thermal blocking mechanism responsible for freezing the remanence of authigenic minerals in carbonate rocks must be further tested. An important step would be applying numerical geodynamical simulations that would allow us to study the heat dissipation of the lithospheric mantle after major collisional events in a supercontinent since surface processes (such as denudation) can be intimately related to mantle dynamics (Braun, 2010; Sacek, 2014).

5.3 Hydrocarbon percolation in carbonates of the Araras group

Even after accounting for the remanence exhibited by rocks in the Guia Formation, whether from the deformed (GC) or undeformed (GT) terrain, which was also preserved during the Paleozoic cooling event, three questions regarding the carbonates of the Araras group arise: a) If we consider smectite-illitisation as a significant process for releasing Fe^{2+} and thereby facilitating the formation of authigenic ferrimagnetic minerals, why did smectite not undergo conversion to illite in the Mirassol d'Oeste (the underlying stratum to Guia formation)? b) What role does hydrocarbon percolation play within this geological unit? c) The majority of dolostones in the Mirassol d'Oeste exhibit only primary remanence. How is it then that only the limestones in the Guia Formation underwent remagnetisation, while the bitumen-enriched upper section of the Mirassol d'Oeste did not experience this phenomenon?

Hydrocarbon strongly percolates in the Guia Formation, mostly occupying the S_0 structure or occurring as a forceful percolation that sections the stratigraphic layers, which suggests a post-diagenetic age for such fluids. Although the hydrocarbon should have originally migrated to the rocks of the Araras group, Júnior et al. (2016) has suggested that the alteration of these fluids to bitumen has happened in situ (indigenous origin). Mid-chain monomethyl alkanes analysed from gas chromatography in a sample from the Guia Formation are commonly reported in mid-to-late Proterozoic oil and their source rocks (Júnior et al., 2016). Hydrocarbon occurrence often accompanies the development of authigenic ferromagnetic phases, as observed in various studies (Benthien & Elmore, 1987; R. Elmore et al., 1987; McCabe et al., 1987; Font et al., 2006; Aldana et al., 2011; Costanzo-Álvarez et al., 2019; J. Hu et al., 2023). Hydrocarbon biodegradation, a significant contributor to ion exchange and a potential catalyst for acquiring chemical remanent magnetisation is intricately tied to bacterial activity. Efficiency in hydrocarbon biodegradation within bacterial environments is subject to various environmental factors, including compositional variations within hydrocarbon fluids, levels of oxygen availability, availability of nitrogen, phosphorus, and carbon, salinity impacting metabolic processes related to hydrocarbons, pressure modulating reaction rates, water activity linked to rock permeability and porosity, and pH levels exerting a strong influence on the overall process (Leahy & Colwell, 1990). Finally, the temperature plays a crucial role in creating a suitable environment for the development of bacterial colonies in this context. Besides the effects of biodegradation, the maturation of organic matter within the carbonates (especially the hydrocarbon) could also induce the formation of authigenic magnetic minerals (Fruit et al., 1995; Banerjee et al., 1997). Certainly, the observed effects significantly influence the production of magnetic grains in the Araras group. It's important to note that the processes of smectite illitisation and organic matter maturation may not be entirely separate; there could be an overlap. This is because clays with a high organic matter content may play a connecting role, potentially facilitating the interaction between smectite illitisation and organic matter maturation processes (Kennedy et al., 2002; R. D. Elmore et al., 2012).

While Font et al. (2005) describes the DRM of Mirassol d'Oeste dolostones as held by specular haematite, the data reported by Trindade et al. (2003) show mainly magnetite blocking temperatures for such primary remanence. Magnetic experiments from this work for MO samples agree with Trindade et al. (2003)'s data, indicating there must be a stratigraphic variability in the basal stratum of the Mirassol d'Oeste formation. As for the Guia Formation, the deformed region over the Paraguay belt was reported to have remanence held by both monoclinic pyrrhotite and magnetite, while remanence in the undeformed region over the Amazon craton would be held by pyrrhotite only (Font et al., 2006). Yet, the results shown here indicate that even if stable remanence is not carried by magnetite in GT samples, it is still present in these rocks.

Our TGA-QMS analysis provided insights into the percolation of organic matter within the Araras group samples. This was achieved by correlating the release of volatile phases, specifically CO_2 and SO_2, with an increase in temperature. In our interpretation, the releases of CO_2 and SO_2 correspond to the decomposition of bitumen and pyrite, as explained in more detail in the results section. Our analysis aligns well with the observation of a significant amount of bitumen, comparable to the Guia formation, particularly within the upper portion of the Mirassol d'Oeste formation (referred to as $MO_{transition}$, see Figure 14c'). This corresponds to a point where stable remanence completely disappears, as illustrated in Figure 14a. It's worth noting that hydrogen sulphide, a common sulphur compound in petroleum (Shi & Wu, 2021), can lead to the dissolution of iron oxides/hydroxides and sulphides upon contact. As suggested by Font et al. (2006), this phenomenon is likely responsible for the disappearance of the primary direction in the upper section of the Mirassol d'Oeste formation, as hydrocarbon does not strongly percolate at the base of these cap carbonates (see emission in Figure 14d').

If the biodegradation/transformation of hydrocarbons alone were the sole factor responsible for the pyrrhotite/magnetite crystallisation in the Guia Formation, one would expect the transition from Mirassol d'Oeste to the Guia Formation to exhibit stable remanence comparable to GT samples. This anticipation arises from the pervasive evidence of hydrocarbon percolation in the upper section of Mirassol d'Oeste. The mechanism involves the dissolution of detrital ferromagnetic phases by H_2S, liberating iron, which then binds to sulphur to crystallise pyrite due to the required minimal sulphur content for its formation (Rickard & Luther, 2007). Similarly, the biodegradation of organic matter results in the reduction of iron facilitated by sulphate-reducing bacteria, leading to the formation of metastable mackinawite. This metastable form can subsequently transform into nanoscopic crystals of pyrite (Duverger et al., 2020). Moreover, with increasing temperature, there is the potential for pyrrhotite/magnetite to crystallise at the top of the Mirassol d'Oeste formation. However, the observed stable remanence in GT samples suggests that factors beyond hydrocarbon biodegradation contribute to the unique crystallisation patterns in the Guia Formation.

KI values of rocks of Guia Formation rocks over the Amazon craton are slightly greater than those over the Paraguay belt, indicating that GT samples (and consequently MO samples) could have reached anchizones' temperatures, meaning that the necessary temperature ($70-120°C$) to convert smectite to illite was achieved. Still, significant K^+ mineral sources were not found in analysed MO samples, either through petrographic or XRD data. Illitisation of smectite requires potassium inputs (Huggett, 2005), which is probably delivered by orthoclase dissolution in the Guia Formation, and the lack of sources of such element could inhibit the driving mechanism of pyrrhotite and magnetite authigenic formation in MO samples. With the increase of temperature towards anchizone conditions, smectite-illitisation delivers more Fe^{2+} in the medium and the thermodynamic conditions necessary to monoclinic pyrrhotite arise. In both the deformed and undeformed regions, magnetite and pyrrhotite can nucleate. However, over the non-deformed region, the remanence is held only by pyrrhotite (although magnetite is also detected in such samples). We speculate this could be related to the higher temperatures achieved in the Paraguay belt region, which favours multiple mechanisms (including clay transformation and organic matter maturation reactions) to be paired and, consequently, a larger volume of magnetite particles would eventually reach the blocking volumes to bear, together with pyrrhotite, a stable remanence (GC samples).

6 Conclusion

In this manuscript, we have assessed the remagnetisation of Neoproterozoic carbonate rocks in South America, employing paleomagnetic analyses alongside macro/microchemical and imaging approaches. In this context, we scrutinise not only the extensive remagnetisation influencing intracratonic basins throughout West Gondwana, elucidating the geological phenomena underpinning it, but also appraise how the magnetic characteristics align with anticipated magnetic "fingerprints" associated with carbonate remagnetisation.

Except for samples from the Irecê basin, the hysteresis parameters in our study deviated from the globally observed cluster of remagnetised rocks. Instead, they closely aligned with non-remagnetised carbonate units around the pseudo-single domain area. This discrepancy leads to a "false negative" scenario for the identified fingerprint. In simpler terms, these carbonate rocks only reveal a secondary component and do not exhibit the expected behaviour. Taking a broader perspective, the unusual Hcr/Hc ratios in remagnetised carbonates typically correspond to mixtures of SD+SP particles. Despite our efforts to quantify the SP contribution through susceptibility loss in frequency-dependent measurements, which indicates a susceptibility loss of over 5% in most samples from remagnetised units (attributed to remagnetised carbonates), we cannot solely attribute this behaviour to SP particles due to the limitations of our method. Additionally, samples from our control unit, the base of the Mirassol d'Oeste (non-remagnetised), show a susceptibility loss comparable to that of the Bambuí em Irecê formation, highlighting another challenge to the original fingerprint assumptions. On the other hand, FORC diagrams reveal a predominant distribution along the coercivity axis, indicating a broad spectrum of non-interacting single-domain/pseudo-single-domain grains. For instance, FORC distributions frequently reach zero coercivities, potentially providing more concrete evidence of SP particles in these rocks. In contrast, the non-remagnetised unit demonstrates a much larger contribution to the interaction axis rather than the coercivity axis. Nevertheless, our thermal experiments, specifically the Lowrie test, support the earlier paleomagnetic interpretation that monoclinic pyrrhotite and magnetite are the primary magnetic carriers in these rocks remagnetised rocks. Consequently, samples comprising an assemblage of more than one magnetic mineral will exhibit the collective properties of these magnetic carriers, making it challenging for their position on the Day plot diagram to carry a clear genetic connotation regarding the origin of their remanence (whether primary or secondary).

Proposing mechanisms like orogenic fluid percolation to explain remagnetisation would necessitate a textural homogeneity, specifically in terms of porosity and permeability. This homogeneity would be required to account for the simultaneous remagnetisation of basins separated by significant distances. While fluid percolation can indeed induce changes in the redox/pH state of the environment and prompt alterations, if the rocks lack a uniform fabric, these changes should be localised along the pathways of fluid percolation. Instead, we posit that the development of secondary magnetic minerals in these rocks is intricately linked to temperature increases and the smectite-illite transformation that releases Fe^{2+} into the medium. This released iron can then nucleate to generate magnetite and/or react with sulphur from the dissolution of other sulphides (e.g., pyrite), leading to the generation of monoclinic pyrrhotite as temperatures rise. XRD analysis, supported by petrographic/microscopic data, confirms the presence of both smectite and highly crystalline illite, along with mineral sources of K^+ (orthoclase) necessary for the reaction to occur. In all the examined samples, we observe a spatial correlation of aluminosilicates with iron oxides/sulphides through micro-XRF. Significantly, XAS analysis allows us to confirm the presence of irregularly shaped grains of pure magnetite and core-shell structures of maghemite-magnetite within the aluminosilicates, both with coherent dimensions of PSD grains. Specifically in the Guia formation (where bitumen is abundant), the generation of these authigenic phases is believed to be an interplay between organic matter maturation/biodegradation and smectite-illitisation.

Henceforth, we recommend that researchers investigating carbonate sedimentary systems with high detrital content from a palaeomagnetic standpoint should examine both the presence and composition of clay minerals. Additionally, they should explore the spatial relationship between these clay minerals and potential carriers of remanence, as clay transformation may play a significant constraint on magnetic mineral authigenesis.

While the processes we discuss here are linked to those initially capable of generating minerals under their respective Curie temperatures and consequently imparting chemical remanent magnetisation, our proposition suggests that the current remanence of these basins results from thermoremanent magnetisation. A crucial observation supporting this interpretation is the statistically similar directions exhibited by both pyrrhotite and magnetite components in all these basins. This implies a rapid blocking process capable of influencing a continental area. Analysis of the thermal demagnetisation data of these samples leads us to infer that only a few thousand years of exposure to temperatures above $300°C$ would suffice to thermally relax the magnetisation of both pyrrhotite and magnetite. The crystalline index of illite in these samples, along with petrographic observations and previous data, confirms that these samples likely experienced temperatures equivalent to low-greenschist grades. We propose that such heat must have been generated during the final amalgamation of Gondwana. As the heat propagation progressively increases, it unblocks the remanence of these ferrimagnetic phases, prompting a constant reset of the remanence. In conclusion, sequential cooling after the Brasiliano orogeny relaxes the isotherms previously shifted upwards due to the collision. Consequently, this process locks in the remanences on these basins across the continent, elucidating their similar single-polarity remanences. These remanences reflect poles falling close to the Early-Middle Ordovician medium poles of the Gondwana apparent polar wander path.

Open Research Section

The experimental data reported in this research is stored at Zenodo (U. D. Bellon et al., 2023) and can be publicly accessed at https://doi.org/10.5281/zenodo.10283417.

Acknowledgments

Magnetic experiments were performed at the USPMag lab at the Instituto de Astronomia, Geofísica e Ciências Atmosféricas (IAG) of the Universidade de São Paulo (USP). X-ray diffraction data were collected at the Institute of Energy and Environment (IEE) of the University of São Paulo. Special recognition to Dra. Cilene de Medeiro and Dra. Ingrid Barcelos, for the assistance provided when collecting SEM-EDS data at the Microscopic Sample Laboratory, at the Brazilian Synchrotron Light Laboratory (LNLS). Experiments performed at the CARNAUBA beamline (LNLS) are related to proposal 20220316. This work is funded by the São Paulo Research Foundation (FAPESP), grants 21/00861-2, 22/14100-6 and 16/06114-6. The opinions, hypotheses, and conclusions or recommendations expressed in this material are the responsibility of the authors and do not necessarily reflect the views of FAPESP. W.W. would like to acknowledge support from the Natural Environmental Research Council through grants NE/V001233/1 and NE/S011978/1.

References

Abrajevitch, A., & Kodama, K. (2009). Biochemical vs. detrital mechanism of remanence acquisition in marine carbonates: A lesson from the k–t boundary interval. *Earth Planet. Sci. Lett*, *286*(1–2), 269–277,. doi: 10.1016/j.epsl.2009.06.035.

Aldana, M., Costanzo-Álvarez, V., Gómez, L., González, C., Díaz, M., Silva, P., & Rada, M. (2011). Identification of magnetic minerals related to hydrocarbon authigenesis in venezuelan oil fields using an alternative decomposition of isothermal remanence curves. *Studia Geophysica et Geodaetica*, *55*, 343–358. doi: 10.1007/s11200-011-0019-0

Alkmim, F., Marshak, S., Pedrosa-Soares, A., Peres, G., Cruz, S., & Whittington, A. (2006). Kinematic evolution of the araçuaí-west congo orogen in brazil and africa: Nutcracker tectonics during the neoproterozoic assembly of gondwana. *Precambrian Res*, *149*(1–2), 43–64,. Retrieved from `https://doi.org/10.1016/j.precamres.2006.06.007.` doi: 10.1016/j.precamres.2006.06.007.

Almeida, F., Amaral, G., Cordani, U., & Kawashita, K. (1973). The precambrian evolution of the south america cratonic margin south of the amazon river. In *The ocean basins and margins* (p. 411–446). New York: Plenum Publishing.

Alvarenga, C. (1990). Phénomènes sédimentaires, structuraux et circulation de fluides développés à la transition chaicirc;ne-craton. exemple de la chaîne paraguay d'âge protérozoïque supérieur, mato grosso, brésil. In *Univ.* Aix-Marseille III.

Alvarenga, C., & Trompette, R. (1992). Glacially influenced sedimentation in the later proterozoic of the paraguay belt (mato grosso, brazil. *Palaeogeogr. Palaeoclimatol. Palaeoecol*, *92*(1–2), 85–105,. doi: 10.1016/0031-0182(92)90136-S.

Aster, R., Borchers, B., & Thurber, C. (2013). Nonlinear regression. In *Parameter estimation and inverse problems* (p. 217–238). Elsevier.

Aubourg, C., Jackson, M., Ducoux, M., & Mansour, M. (2019). Magnetite-out and pyrrhotite-in temperatures in shales and slates. *Terra Nova*, *31*(6), 534-539. Retrieved from `https://onlinelibrary.wiley.com/doi/abs/10.1111/ter.12424` doi: https://doi.org/10.1111/ter.12424

Babinski, M., Liu, D., Trindade, R., Neves, B., & Santos, R. (2004). *U–pb shrimp ages of detrital zircons from the bebedouro formation, northeast brazil: constraints on sediment provenance and depositional age of neoproterozoic glacial rocks of the são francisco craton.*

Babinski, M., Vieira, L., & Trindade, R. (2007). Direct dating of the sete lagoas cap carbonate (bambuí group, brazil) and implications for the neoproterozoic glacial events. *Terra Nov*, *19*(6), 401–406,. doi: 10.1111/j.1365-3121.2007.00764.x.

Bachtadse, V., Voo, R., & Hälbich, I. (1987). Paleomagnetism of the western cape fold belt, south africa, and its bearing on the paleozoic apparent polar wander path for gondwana. *Earth Planet. Sci. Lett*, *84*(4), 487–499,. doi: 10.1016/0012-821X(87)90013-6.

Banerjee, S., Elmore, R. D., & Engel, M. H. (1997). Chemical remagnetization and burial diagenesis: Testing the hypothesis in the pennsylvanian belden formation, colorado. *Journal of Geophysical Research: Solid Earth*, *102*(B11), 24825-24842. Retrieved from `https://agupubs.onlinelibrary.wiley.com/doi/abs/10.1029/97JB01893` doi: https://doi.org/10.1029/97JB01893

Bellon, U., Trindade, R., & Williams, W. (2023). Unmixing of magnetic hysteresis loops through a modified gamma-cauchy exponential model. *Geochemistry, Geophys. Geosystems*, *24*, 1–21,. doi: 10.1029/2023GC011048.

Bellon, U. D., Williams, W., Trindade, R., Galante, D., Sant'Anna, L., & Pescarini, T. (2023). Magnetic properties and chemical analysis of remagnetised carbonates of south america [dataset]. *Zenodo*. Retrieved from `https://doi.org/10.5281/zenodo.10283417` doi: 10.5281/zenodo.10283417

Benthien, R., & Elmore, R. (1987). Origin of magnetization in the phosphoria formation at sheep mountain, wyoming: a possible relationship with hydrocarbons. *Geophysical Research Letters*, *14*(4), 323–326. Retrieved from `https://doi.org/10.1029/GL014i004p00323` doi: 10.1029/GL014i004p00323

Braun, J. (2010). The many surface expressions of mantle dynamics. *Nat. Geosci*, *3*(12), 825–833,. doi: 10.1038/ngeo1020.

Brigatti, M. F., Galán, E., & Theng, B. K. G. (2013). Structure and Mineralogy of Clay Minerals. In *Developments in clay science* (Vol. 5, pp. 21–81). Retrieved from `https://linkinghub.elsevier.com/retrieve/pii/B978008098258800002X` doi: 10.1016/B978-0-08-098258-8.00002-X

Brothers, L., Engel, M., & Elmore, R. (1996). The late diagenetic conversion of pyrite to magnetite by organically complexed ferric iron. *Chemical Geology*, *130*(1), 1-14. Retrieved from `https://www.sciencedirect.com/science/article/pii/0009254196000071` doi: https://doi.org/10.1016/0009-2541(96)00007-1

Butler, R. (1992). *Paleomagnetism: magnetic domains to geologic terranes, no.*

Butler, R., & Banerjee, S. (1975). Theoretical single-domain grain size range in magnetite and titanomagnetite [[Online].]. *J. Geophys. Res. Oct*, *80*(29). Retrieved from `http://pilotscholars.up.edu/env_facpubs/17.` (Available:)

Caby, R., & Costa Campos Neto, M. (2022). Basement domes in a greenschist facies context: Tectono-metamorphic evolution of the southern quadrilátero ferrífero, southeast brazil. *Tectonophysics*, *828*(February), 229280,. (p.) doi: 10.1016/j.tecto.2022.229280.

Callaway, W., & McAtee, J. (1985). Magnetic susceptibilities of representative smectites. *Am. Mineral*, *70*(9–10), 996–1003,.

Carvallo, C., Muxworthy, A., & Dunlop, D. (2006). First-order reversal curve (forc) diagrams of magnetic mixtures: Micromagnetic models and measurements. *Phys. Earth Planet. Inter*, *154*(3–4), 308–322,. doi: 10.1016/j.pepi.2005.06.017.

Carvallo, C., Özdemir, O., & Dunlop, D. (2004). First-order reversal curve (forc) diagrams of elongated single-domain grains at high and low temperatures. *J. Geophys. Res.*

Solid Earth, *109*(4). doi: 10.1029/2003JB002539.

Chang, L. (2013). Low-temperature magnetic properties of pelagic carbonates: Oxidation of biogenic magnetite and identification of magnetosome chains. *J. Geophys. Res. Solid Earth*, *118*(12), 6049–6065,. doi: 10.1002/2013JB010381.

Chang, L. (2014). Magnetic detection and characterization of biogenic magnetic minerals: A comparison of ferromagnetic resonance and first-order reversal curve diagrams. *J. Geophys. Res. Solid Earth*, *119*(8), 6136–6158,. doi: 10.1002/2014JB011213.

Chemale, J., Alkmin, F., & Endo, I. (1993). Late proterozoic tectonism in the interior of the são francisco craton. In tion & H. Dispersal (Eds.), *Gondwana eight —assembly evolu* (p. 29–42). Balkema, Rotterdam.

Costanzo-Álvarez, V., Rapalini, A., Aldana, M., Díaz, M., Kietzmann, D., & Iglesia-Llanos, M. (2019). A combined rock-magnetic and epr study about the effects of hydrocarbon-related diagenesis on the magnetic signature of oil shales (vaca muerta formation, southwestern argentina. *Journal of Petroleum Science and Engineering*, *173*(September 2018), 861–879. Retrieved from `https://doi.org/10.1016/j.petrol.2018.10.082` doi: 10.1016/j.petrol.2018.10.082

Couto, D. (2020). Mineralogy composition and texture indicative of fluid-assisted remobilization in carbonate units of the irecê basin, brazil. *J. South Am. Earth Sci*, *110*, 103346,. doi: 10.1016/j.jsames.2021.103346.

Crouzet, C., Rochette, P., & Ménard, G. (2001, 06). Experimental evaluation of thermal recording of successive polarities during uplift of metasediments. *Geophysical Journal International*, *145*(3), 771-785. Retrieved from `https://doi.org/10.1046/j.0956-540x.2001.01423.x` doi: 10.1046/j.0956-540x.2001.01423.x

Dannemann, S., Appel, E., Rösler, W., Neumann, U., Liebke, U., & Nag, D. (2022). Palaeomagnetic indication for india–asia collision at 12°n and maximum 810 km greater india extent in the western suture zone. *Geophysical Journal International*, *229*, 1193–1211. Retrieved from `https://doi.org/10.1093/gji/ggab528` doi: 10.1093/gji/ggab528

Dardenne, M. (1978). Síntese sobre a estratigrafia do grupo bambuí no brasil central. In *Anais do xxx congresso brasileiro de geologia* (p. 597–610).

Davidson, M., Egger, J., Elmore, R., Engel, M., Woods, S., & Abraham, M. (2000). Orogenic fluids and secondary magnetizations : testing the relationship in the south wales coalfield foreland basin. *Journal of Geochemical Exploration*, *70*, 581–584.

Day, R., Fuller, M., & Schmidt. (1977). Hysteresis properties of titanomagnetites: grain-size and compositional dependence. *Physics of the Earth and Planetary Interiors*, *13*, 260–267. doi: https://doi.org/10.1016/0031-9201(77)90108-X

Dearing, J. (1996). Frequency-dependent susceptibility measurements of environmental materials. *Geophys. J. Int*, *124*(1), 228–240,. doi: 10.1111/j.1365-246X.1996.tb06366.x.

Duncan, D. (2018). Synchrotron-based spectroscopy in on-surface polymerization of covalent networks. In *Encyclopedia of interfacial chemistry* (p. 436–445). Surface Science and Electrochemistry, Elsevier.

Dunlop, D. (2002). Theory and application of the day plot (m rs / m s versus h cr / h c) 1. theoretical curves and tests using titanomagnetite data. *J. Geophys. Res*, *107*(B3). (p. 2056,) doi: 10.1029/2001JB000486.

Dunlop, D., & Özdemir, O. (1997). *Rock magnetism: Fundamentals and frontiers* (1st ed.). Cambridge: Cambridge University Press.

Dunlop, D., Özdemir, O., Clark, D., & Schmidt, P. (2000). Time–temperature relations for the remagnetization of pyrrhotite (fe7s8) and their use in estimating paleotemperatures. *Earth Planet. Sci. Lett*, *176*(1), 107–116,. doi: 10.1016/S0012-821X(99)00309-X.

Duverger, A., Berg, J., Busigny, V., Guyot, F., Bernard, S., & Miot, J. (2020). Mechanisms of pyrite formation promoted by sulfate-reducing bacteria in pure culture. *Front. Earth Sci*, *8*(November), 1–15,. doi: 10.3389/feart.2020.588310.

D'Agrella-Filho, M. (1995). Paleomagnetism of carbonatic sedimentary sequences of the salitre formation, chapada diamantina—bahia. In *4th in. cong* (p. 262–265). Sociedade

Brasileira de Geofísica.
D'Agrella-Filho, M., Babinski, M., Trindade, R., Schmus, W., & Ernesto, M. (2000). Simultaneous remagnetization and u–pb isotope resetting in neoproterozoic carbonates of the são francisco craton, brazil. *Precambrian Res*, *99*(3–4), 179–196,. doi: 10.1016/S0301-9268(99)00059-5.
D'Agrella-Filho, M., Irene, M., Raposo, B., & Egydio-silva, M. (2004). Paleomagnetic study of the juiz de fora complex, se brazil: Implications for gondwana. *Gondwana Res*, *7*(I), 103–113,.
D'Agrella-Filho, M., & Pacca, I. (1986). Paleomagnetism of metamorphic rocks from the piquete region-ribeira valley, southeastern brazil. *Rev. Bras. Geociências*, *4*, 79–84,.
Egli, R. (2003). Analysis of the field dependence of remanent magnetization curves. *J. Geophys. Res. Solid Earth*, *108*(B2), 1–25,. doi: 10.1029/2002jb002023.
Egli, R. (2013). Variforc: An optimized protocol for calculating non-regular first-order reversal curve (forc) diagrams. *Glob. Planet. Change*, *110*, 302–320,. Retrieved from `https://doi.org/10.1016/j.gloplacha.2013.08.003.` doi: 10.1016/j.gloplacha.2013.08.003.
Egli, R., Chen, A., Winklhofer, M., Kodama, K., & Horng, C.-S. (2010). Detection of noninteracting single domain particles using first-order reversal curve diagrams. *Geochemistry, Geophys. Geosystems*, *11*(1), – ,. doi: 10.1029/2009GC002916.
Elmore, R., Engel, M., Crawford, L., Nick, K., Imbus, S., & Sofer, Z. (1987). Evidence for a relationship between hydrocarbons and authigenic magnetite. *Nature*, *325*(6103), 428–430. Retrieved from `https://doi.org/10.1038/325428a0` doi: 10.1038/325428a0
Elmore, R. D., Muxworthy, A. R., & Aldana, M. (2012). Remagnetization and chemical alteration of sedimentary rocks. *Geological Society of London*, *371*, 1–21.
Emmerton, S., Muxworthy, A., Sephton, M., Aldana, M., Costanzo-Alvarez, V., Bayona, G., & Williams, W. (2013). Correlating biodegradation to magnetization in oil bearing sedimentary rocks. *Geochimica et Cosmochimica Acta*, *112*, 146–165. Retrieved from `https://doi.org/10.1016/j.gca.2013.03.008` doi: 10.1016/j.gca.2013.03.008
Evans, M. E., & Heller, F. (2003). *Environmental Magnetism: Principles and Applications of Enviromagnetic*. Academic Press. doi: 10.1007/978-1-4020-4423-6_95
Figueiredo, F., Almeida, R., Tohver, E., Babinski, M., Liu, D., & Fanning, C. (2009). Neoproterozoic glacial dynamics revealed by provenance of diamictites of the bebedouro formation, são francisco craton, central eastern brazil. *Terra Nov*, *21*(5), 375–385,. doi: 10.1111/j.1365-3121.2009.00893.x.
Fonseca, A., Novo, T., Nachtergaele, S., Fonte-Boa, T., Ranst, G., & Grave, J. (2021). Differential phanerozoic evolution of cratonic and non-cratonic lithosphere from a thermochronological perspective: São francisco craton and marginal orogens (brazil. *Gondwana Res*, *93*, 106–126,. doi: 10.1016/j.gr.2021.01.006.
Fonseca, A., Piffer, G., Nachtergaele, S., Ranst, G., Grave, J., & Novo, T. (2020). Devonian to permian post-orogenic denudation of the brasília belt of west gondwana: insights from apatite fission track thermochronology. *J. Geodyn*, *137*(March), 101733,. (p.) doi: 10.1016/j.jog.2020.101733.
Font, E., Rapalini, A. E., Tomezzoli, R. N., Trindade, R. I. F., & Tohver, E. (2012). Episodic remagnetizations related to tectonic events and their consequences for the south america polar wander path. *Geological Society, London, Special Publications*, *371*(1), 55-87. Retrieved from `https://www.lyellcollection.org/doi/abs/10.1144/SP371.7` doi: 10.1144/SP371.7
Font, E., Trindade, R., & Nédélec, A. (2005). Detrital remanent magnetization in haematite-bearing neoproterozoic puga cap dolostone, amazon craton: A rock magnetic and sem study. *Geophys. J. Int*, *163*(2), 491–500,. doi: 10.1111/j.1365-246X.2005.02776.x.
Font, E., Trindade, R., & Nédélec, A. (2006). Remagnetization in bituminous limestones of the neoproterozoic araras group (amazon craton): Hydrocarbon maturation, burial diagenesis, or both? *J. Geophys. Res. Solid Earth*, *111*(6), 1–17,. doi: 10.1029/2005JB004106.

Franceschinis, P., Rapalini, A., Escayola, M., & Piceda, C. (2019). Paleogeographic and tectonic evolution of the pampia terrane in the cambrian: New paleomagnetic constraints. *Tectonophysics*, *779*, 228386,. doi: 10.1016/j.tecto.2020.228386.

Fruit, D., Elmore, R. D., & Halgedahl, S. (1995). Remagnetization of the folded belden formation, northwest colorado. *Journal of Geophysical Research: Solid Earth*, *100*(B8), 15009-15023. Retrieved from `https://agupubs.onlinelibrary.wiley.com/doi/abs/10.1029/95JB00045` doi: https://doi.org/10.1029/95JB00045

Gaucher, C., Boggiani, P., Sprechmann, P., Sial, A., & Fairchild, T. (2003). Integrated correlation of the vendian to cambrian arroyo del soldado and corumbá groups (uruguay and brazil): palaeogeographic, palaeoclimatic and palaeobiologic implications. *Precambrian Res*, *120*(3–4), 241–278,. doi: 10.1016/S0301-9268(02)00140-7.

Ge, K., Williams, W., Nagy, L., & Tauxe, L. (2021). Models of maghematization: Observational evidence in support of a magnetic unstable zone. *Geochemistry, Geophys. Geosystems*, *22*(3), 1–12,. doi: 10.1029/2020GC009504.

Geiss, C., Egli, R., & Zanner, C. (2008). Direct estimates of pedogenic magnetite as a tool to reconstruct past climates from buried soils. *J. Geophys. Res*, *113*(B11), 11102,. doi: 10.1029/2008JB005669.

Golovanova, I. V., Danukalov, K. N., Salmanova, R. Y., Levashova, N. M., Parfiriev, N. P., Sergeeva, N. D., & Meert, J. G. (2023, jul). Magnetic field hyperactivity during the early Neoproterozoic: A paleomagnetic and cyclostratigraphic study of the Katav Formation, southern Urals, Russia. *Geoscience Frontiers*, *14*(4), 101558. Retrieved from `https://www.sciencedirect.com/science/article/pii/S1674987123000257https://linkinghub.elsevier.com/retrieve/pii/S1674987123000257` doi: 10.1016/j.gsf.2023.101558

Goscombe, B., Foster, D., Gray, D., & Wade, B. (2018). The evolution of the damara orogenic system: A record of west gondwana assembly and crustal response. In S. Siegesmund, B. S., O. M., & O. P. (Eds.), *Geology of southwest gondwana* (p. 303–352). Springer.

Grotzinger, J. P., & James, N. P. (2000). Precambrian carbonates: evolution of understading. In J. P. Grotzinger & N. P. James (Eds.), *Carbonate sedimentation and diagenesis in the evolving precambrian world* (pp. 3–20). Tulsa, Oklahoma, U.S.A: Society for Sedimentary Geology.

Guacaneme, C., Babinski, M., Paula-Santos, G., & Pedrosa-Soares, A. (2017). C, o, and sr isotopic variations in neoproterozoic-cambrian carbonate rocks from sete lagoas formation (bambuí group), in the southern são francisco basin, brazil. *Brazilian J. Geol*, *47*(3), 521–543,. doi: 10.1590/2317-4889201720160126.

Guimarães, G., Pierosan, R., & Ruiz, A. (2017). Geologia e petrologia do granito são vicente na região do parque estadual Águas quentes, estado de mato grosso, brasil. *Geol. USP. Série Científica*, *17*(3), 29,. doi: 10.11606/issn.2316-9095.v17-426.

Gunasekaran, S., & Anbalagan, G. (2007). Thermal decomposition of natural dolomite. *Bull. Mater. Sci*, *30*(4), 339–344,. doi: 10.1007/s12034-007-0056-z.

Haldar, S., & Tišljar, J. (2014). Sedimentary rocks. *Introduction to Mineralogy and Petrology*, *3*(C), 121–212.

Harrison, R., Muraszko, J., Heslop, D., Lascu, I., Muxworthy, A., & Roberts, A. (2018). An improved algorithm for unmixing first-order reversal curve diagrams using principal component analysis. *Geochem. Geophys. Geosyst*, *19*, 1595–1610,.

Henderson, C., Cressey, G., & Redfern, S. (1995). Geological applications of synchrotron radiation. *Radiat. Phys. Chem*, *45*(3), 459–481,. doi: 10.1016/0969-806X(95)92799-5.

Heslop, D. (2020). An automatic model selection-based machine learning framework to estimate forc distributions. *J. Geophys. Res. Solid Earth*, *125*(10), 1–16,. doi: 10.1029/2020JB020418.

Hirt, A. M., Banin, A., & Gehring, A. U. (1993, 12). Thermal generation of ferromagnetic minerals from iron-enriched smectites. *Geophysical Journal International*, *115*(3), 1161-1168. Retrieved from `https://doi.org/10.1111/j.1365-246X.1993.tb01518.x` doi: 10.1111/j.1365-246X.1993.tb01518.x

Hrouda, F. (2011). Models of frequency-dependent susceptibility of rocks and soils revisited and broadened. *Geophys. J. Int*, *187*(3), 1259–1269,. doi: 10.1111/j.1365-246X.2011.05227.x.

Hrouda, F., Pokorný, J., Ježek, J., & Chadima, M. (2013). Out-of-phase magnetic susceptibility of rocks and soils: A rapid tool for magnetic granulometry. *Geophys. J. Int*, *194*(1), 170–181,. doi: 10.1093/gji/ggt097.

Hu, G., Dam-Johansen, K., Wedel, S., & Hansen, J. (2006). Decomposition and oxidation of pyrite. *Prog. Energy Combust. Sci*, *32*(3), 295–314,. doi: 10.1016/j.pecs.2005.11.004.

Hu, J., Zhang, Y., Jia, D., Muxworthy, A., Selby, D., & Li, Y. (2023). Combining paleomagnetic and re-os isotope data to date hydrocarbon generation and accumulation processes. *Journal of Geophysical Research: Solid Earth*, *128*(2). Retrieved from `https://doi.org/10.1029/2022JB025955` doi: 10.1029/2022JB025955

Huang, W., Lippert, P., Jackson, M., Dekkers, M., Zhang, Y., Li, J., ... Hinsbergen, D. (2017). Remagnetization of the paleogene tibetan himalayan carbonate rocks in the gamba area: Implications for reconstructing the lower plate in the india-asia collision. *Journal of Geophysical Research: Solid Earth*, *122*, 808–825. Retrieved from `https://doi.org/10.1002/2016JB013662` doi: 10.1002/2016JB013662

Huggett, J. M. (2005). Sedimentary Rocks — Clays and Their Diagenesis. In *Encyclopedia of geology* (pp. 62–70). Elsevier. Retrieved from `https://linkinghub.elsevier.com/retrieve/pii/B0123693969003117` doi: 10.1016/B0-12-369396-9/00311-7

Jaboyedoff, M., Bussy, F., Kübler, B., & Thelin, P. (2001). Illite 'crystallinity' revisited. *Clays Clay Miner*, *49*(2), 156–167,. doi: 10.1346/CCMN.2001.0490205.

Jackson, M. (1990). Diagenetic sources of stable remanence in remagnetized paleozoic cratonic carbonates: a rock magnetic study. *J. Geophys. Res*, *95*(B3), 2753–2761,. doi: 10.1029/JB095iB03p02753.

Jackson, M., & Sun, W. (1992). The rock magnetic fingerprint of chemical remagnetization in midcontinental paleozoic carbonates. *Geophys. Res. Lett*, *19*(8), 781–784,.

Jackson, M., & Swanson-Hysell, N. (2012). Rock magnetism of remagnetized carbonate rocks: Another look. *Geol. Soc. Spec. Publ*, *371*(1), 229–251,. doi: 10.1144/SP371.3.

Jiao, W., Li, Y., Yang, Z., & Liu, J. (2019). A widespread early mesozoic remagnetization in south china. *Journal of Geophysical Research: Solid Earth*, *124*, 88–103. Retrieved from `https://doi.org/10.1029/2018JB016707` doi: 10.1029/2018JB016707

Júnior, G., Nogueira, A., Neto, E., Moura, C., Araújo, B., & Reis, F. (2016). Organic matter in the neoproterozoic cap carbonate from the amazonian craton, brazil. *J. South Am. Earth Sci*, *72*, 7–24,. doi: 10.1016/j.jsames.2016.07.012.

Kars, M., Aubourg, C., Pozzi, J., & Janots, D. (2012). Continuous production of nanosized magnetite through low grade burial. *Geochemistry, Geophys. Geosystems*, *13*(8), – ,. doi: 10.1029/2012GC004104.

Karunadasa, K., Manoratne, C., Pitawala, H., & Rajapakse, R. (2019). Thermal decomposition of calcium carbonate (calcite polymorph) as examined by in-situ high-temperature x-ray powder diffraction. *J. Phys. Chem. Solids*, *134*(May), 21–28,. doi: 10.1016/j.jpcs.2019.05.023.

Kennedy, M. J., Pevear, D. R., & Hill, R. J. (2002). Mineral surface control of organic carbon in black shale. *Science*, *295*(5555), 657-660. Retrieved from `https://www.science.org/doi/abs/10.1126/science.1066611` doi: 10.1126/science.1066611

Kloprogge, J. T., Komarneni, S., & Amonette, J. E. (1999). Synthesis of smectite clay minerals: A critical review. *Clays and Clay Minerals*, *47*(5), 529–554. doi: 10.1346/CCMN.1999.0470501

Kübler, B. (1964). Les argiles indicateurs de métamorphisme. *Rev. Inst. Français du Pétrole*, *29*, 1096–1113,.

Kübler, B. (1967). La cristallinité de l'illite et les zones tout À fait supérieures du métamorphisme. In *Etages tectoniques, colloque de neuchâtel* (p. 105–121).

Kübler, B. (1968). Evaluation quantitative du métamorphisme par cristallinité de l'illite. *Bull. Cent. Rech. Pau SNPA*, *2*, 385–397,.

Kübler, B. (1990). 'cristallinité' de l'illite et mixed-layer: Brève révision. *Schweitzerische Mineral. Petrophische Mitteilungen*, *70*, 89–93,.

Labus, M. (2020). Pyrite thermal decomposition in source rocks. *Fuel*, *287*, 119529,. doi: 10.1016/j.fuel.2020.119529.

Lanson, B., Sakharov, B. A., Claret, F., & Drits, V. A. (2009). Diagenetic smectite-to-illite transition in clay-rich sediments: A reappraisal of x-ray diffraction results using the multi-specimen method. *American Journal of Science*, *309*(6), 476–516. doi: 10.2475/06.2009.03

Lascu, I., Einsle, J., Ball, M., & Harrison, R. (2018). The vortex state in geologic materials: A micromagnetic perspective. *J. Geophys. Res. Solid Earth*, *123*(9), 7285–7304,. doi: 10.1029/2018JB015909.

Leahy, J., & Colwell, R. (1990). Microbial degradation of hydrocarbons in the environment. *Microbiological Reviews*, *54*(3), 305–315.

Lennie, A., England, K., & Vaughan, D. (1995). Transformation of synthetic mackinawite to hexagonal pyrrhotite; a kinetic study. *Am. Mineral*, *80*(9–10), 960–967,. doi: 10.2138/am-1995-9-1012.

Levi, S. (2007). Magnetization, Chemical Remanent (CRM). In D. Gubbins & E. Herrero-Bervera (Eds.), *Encyclopedia of geomagnetism and paleomagnetism* (pp. 580–588). Dordrecht: Springer Netherlands. Retrieved from `https://doi.org/10.1007/978-1-4020-4423-6_190` doi: 10.1007/978-1-4020-4423-6_190

Liu, Q., Roberts, A. P., Larrasoaña, J. C., Banerjee, S. K., Guyodo, Y., Tauxe, L., & Oldfield, F. (2012). Environmental magnetism: Principles and applications. *Reviews of Geophysics*, *50*(4). doi: https://doi.org/10.1029/2012RG000393

Lowrie, W. (1990). Identification of ferromagnetic minerals in a rock by coercivity and unblocking temperature properties. *Geophys. Res. Lett*, *17*(2), 159–162,. doi: 10.1029/GL017i002p00159.

Machel, H. (2001). Bacterial and thermochemical sulfate reduction in diagenetic settings — old and new insights. *Sediment. Geol*, *140*(1–2), 143–175,. doi: 10.1016/S0037-0738(00)00176-7.

Martín-Hernández, F., & Hirt, A. (2003). The anisotropy of magnetic susceptibility in biotite, muscovite and chlorite single crystals. *Tectonophysics*, *367*(1–2), 13–28,. doi: 10.1016/S0040-1951(03)00127-6.

Matamoros-Veloza, A. (2018). A highly reactive precursor in the iron sulfide system. *Nat. Commun*, *9*(1), 3125,. doi: 10.1038/s41467-018-05493-x.

Maxbauer, D., Feinberg, J., & Fox, D. (2016). Max unmix: A web application for unmixing magnetic coercivity distributions. *Comput. Geosci*, *95*, 140–145,. doi: 10.1016/j.cageo.2016.07.009.

McCabe, C., & Elmore, R. (1989). The occurrence and origin of late paleozoic remagnetization in the sedimentary rocks of north america. *Reviews of Geophysics*, *27*, 471–494. doi: 10.1029/RG027i004p00471

McCabe, C., Sassen, R., & Saffer, B. (1987). Occurrence of secondary magnetite within biodegraded oil. *Geology*, *15*(1), 7. Retrieved from `https://doi.org/10.1130/0091-7613(1987)15` doi: 10.1130/0091-7613(1987)15

McCabe, C., Voo, R., Peacor, D., Scotese, C., & Freeman, R. (1983). Diagenetic magnetite carries ancient yet secondary remanence in some paleozoic sedimentary carbonates. *Geology*, *11*, 221–223. Retrieved from `https://doi.org/10.1130/0091-7613(1983)11` doi: 10.1130/0091-7613(1983)11

Merdith, A. S., Williams, S. E., Collins, A. S., Tetley, M. G., Mulder, J. A., Blades, M. L., ... Müller, R. D. (2021, mar). Extending full-plate tectonic models into deep time: Linking the Neoproterozoic and the Phanerozoic. *Earth-Science Reviews*, *214*, 103477. doi: 10.1016/j.earscirev.2020.103477

Miller, J., & Kent, D. (1988). Regional trends in the timing of alleghanian remagnetization in the appalachians. *Geology*, *16*, 588–591.

Misi, A., Azmy, K., Kaufman, A., Oliveira, T., Sanches, A., & Oliveira, G. (2014). Review of the geological and geochronological framework of the vazante sequence, minas gerais, brazil: Implications to metallogenic and phosphogenic models. *Ore Geol. Rev*, *63*, 76–90,. doi: 10.1016/j.oregeorev.2014.05.002.

Misi, A., & Kyle, J. (1994). Upper proterozoic carbonate stratigraphy, diagenesis, and stromatolitic phosphorite formation, irece basin, bahia, brazil. *J. Sediment. Res. A Sediment. Petrol. Process*(2), 299–310,. doi: 10.1306/d4267d84-2b26-11d7-8648000102c1865d.

Misi, A., & Veizer, J. (1998). Neoproterozoic carbonate sequences of the una group, irecê basin, brazil: chemostratigraphy, age and correlations. *Precambrian Res*, *89*(1–2), 87–100,. doi: 10.1016/S0301-9268(97)00073-9.

Mohriak, W., & Fainstein, R. (2012). Phanerozoic regional geology of the eastern brazilian margin. In *Regional geology and tectonics: Phanerozoic passive margins, cratonic basins and global tectonic maps* (p. 222–282). Elsevier.

Morad, S. (1978). Feldspars in sedimentary rocks. In *Sedimentology* (p. 452–457). Berlin, Heidelberg: Springer.

Moreira, D., Uhlein, A., Dussin, I., Uhlein, G., & Misuzaki, A. (2020). A cambrian age for the upper bambuí group, brazil, supported by the first u-pb dating of volcaniclastic bed. *J. South Am. Earth Sci*, *99*(January), 102503,. (p.) doi: 10.1016/j.jsames.2020.102503.

Muxworthy, A., & Dunlop, D. (2002). First-order reversal curve (forc) diagrams for pseudo-single-domain magnetites at igh temperature. *Earth Planet. Sci. Lett*, *203*(1), 369–382,. doi: 10.1016/S0012-821X(02)00880-4.

Mählmann, R., & Frey, M. (2012). Standardisation, calibration and correlation of the kübler-index and the vitrinite/bituminite reflectance: an inter-laboratory and field related study. *Swiss J. Geosci*, *105*(2), 153–170,. doi: 10.1007/s00015-012-0110-8.

Nagata, T. (1961). *Rock Magnetism.* Tokyo: Maruzen Company Ltd.

Nagy, L. (2017). Stability of equidimensional pseudo–single-domain magnetite over billion-year timescales. *Proc. Natl. Acad. Sci. U. S. A*, *114*(39), 10356–10360,. doi: 10.1073/pnas.1708344114.

Nagy, L., Williams, W., Tauxe, L., & Muxworthy, A. (2019). From nano to micro: Evolution of magnetic domain structures in multidomain magnetite. *Geochemistry, Geophys. Geosystems*, *20*(6), 2907–2918,. doi: 10.1029/2019GC008319.

Nagy, L., Williams, W., Tauxe, L., Muxworthy, A., & Ferreira, I. (2019). Thermomagnetic recording fidelity of nanometer-sized iron and implications for planetary magnetism. *Proc. Natl. Acad. Sci*, *116*(6), 1984–1991,. doi: 10.1073/pnas.1810797116.

Néel, L. (1955). Some theoretical aspects of rock-magnetism. *Advances in Physics*, *4*(14), 191–243. Retrieved from `https://doi.org/10.1080/00018735500101204` doi: 10.1080/00018735500101204

Ning, J., Zheng, Y., Brown, B., Young, D., & Nesic, S. (2015). Construction and verification of pourbaix diagrams for hydrogen sulfide corrosion of mild steel. *NACE - Int. Corros. Conf. Ser*(5507), 1–19,.

Nogueira, A., & Riccomini, C. (2006). O grupo araras (neoproterozóico) na parte norte da faixa paraguai e sul do craton amazônico, brasil. *Rev. Bras. Geociências*, *36*(4).

Nogueira, A., Riccomini, C., Sial, A., Moura, C., & Fairchild, T. (2003). Soft-sediment deformation at the base of the neoproterozoic puga cap carbonate (southwestern amazon craton, brazil): Confirmation of rapid icehouse to greenhouse transition in snowball earth. *Geology*, *31*(7), 613–616,. doi: 10.1130/0091-7613(2003)031

Oliveira, L., Gonçalves, M., & Tella, V. (2014). *Projeto sirius: a nova fonte de luz síncrotron brasileira.*

Ormerod, R. (2001). Surface chemistry: Electron yield spectroscopy. In *Encyclopedia of materials* (p. 9006–9008). Science and Technology, Elsevier.

Parry, L. (1982). Magnetization of immobilized particle dispersions with two distinct particle sizes. *Phys. Earth Planet. Inter*, *28*(3), 230–241,. doi: 10.1016/0031-9201(82)90004-8.

Patarachao, B. (2019). Xrd analysis of illite-smectite interstratification in clays from oil sands ores. *Adv. X-ray Anal*, *62*(C), 22–31,.

Paula-Santos, G., Babinski, M., Kuchenbecker, M., Caetano-Filho, S., Trindade, R., & Pedrosa-Soares, A. (2015). New evidence of an ediacaran age for the bambuí group in southern são francisco craton (eastern brazil) from zircon u–pb data and isotope chemostratigraphy. *Gondwana Res*, *28*(2), 702–720,. doi: 10.1016/j.gr.2014.07.012.

Pavlov, V., & Gallet, Y. (2005). A third superchron during the early paleozoic. *International Union of Geological Sciences*, *28*. doi: 10.18814/epiiugs/2005/v28i2/001

Pedrosa-soares, A. (2007). Orógeno araçuaí: síntese do conhecimento 30 anos após almeida 1977. *Geonomos*, *15*(1), 1–16,. Retrieved from `https://doi.org/10.18285/geonomos.v15i1.103.` (doi:) doi: 10.18285/geonomos.v15i1.103.

Pedrosa-Soares, A. (2020). O orógeno araçuaí à luz da geocronologia: um tributo a umberto cordani. In A. November, W. Teixeira, & B. Neves (Eds.), *Geocronologia e evolução tectônica do continente sul-americano: a contribuição de umberto giuseppe cordani* (1st ed., p. 250–272). São Paulo: Solaris Edições Culturais.

Pedrosa-Soares, A., Cordani, U., & Nutman, A. (2000). Constraining the age of neoproterozoic glaciation in eastern brazil: first u-pb (shrimp) data of detrital zircons. *Rev. Bras. Geociências*, *30*.

Pedrosa-Soares, A., Noce, C., Wiedemann, C., & Pinto, C. (2001). The araçuaí-west-congo orogen in brazil: An overview of a confined orogen formed during gondwanaland assembly. *Precambrian Res*, *110*(1–4), 307–323,. doi: 10.1016/S0301-9268(01)00174-7.

Penner-Hahn, J. (2003). X-ray absorption spectroscopy. In *Comprehensive coordination chemistry* (Vols. II, vol. 2, p. 159–186). Elsevier.

Phillips, E. J. P., Lovley, D. R., & Roden, E. E. (1993). Composition of non-microbially reducible fe(iii) in aquatic sediments. *Applied and Environmental Microbiology*, *59*(8), 2727-2729. Retrieved from `https://journals.asm.org/doi/abs/10.1128/aem.59.8.2727-2729.1993` doi: 10.1128/aem.59.8.2727-2729.1993

Piceda, C., Franceschinis, P., Escayola, M., & Rapalini, A. (2018). Paleomagnestism of the santa victoria group in the mojotoro range, salta: Contributions to the paleogeographic position of pampia in early paleozoic [paleomagnetismo del grupo santa victoria en la sierra de mojotoro, salta: Aportes a la reconstrucción pal. *Rev. la Asoc. Geol. Argentina*, *75*(4), 518–532,. Retrieved from `https://revista.geologica.org.ar/raga/article/view/134.` (Online]. Available:)

Pike, C., Roberts, A., Dekkers, M., & Verosub, K. (2001). An investigation of multi-domain hysteresis mechanisms using forc diagrams. *Phys. Earth Planet. Inter*, *126*(1–2), 11–25,. Retrieved from `https://doi.org/10.1016/S0031-9201(01)00241-2.` doi: 10.1016/S0031-9201(01)00241-2.

Piquer, C., Laguna-Marco, M., Roca, A., Boada, R., Guglieri, C., & Chaboy, J. (2014). Fe k-edge x-ray absorption spectroscopy study of nanosized nominal magnetite. *J. Phys. Chem*, *118*(2), 1332–1346,. doi: 10.1021/jp4104992.

Potter, D., Corbett, P., Barclay, S., & Haszeldine, R. (2004). Quantification of illite content in sedimentary rocks using magnetic susceptibility - a rapid complement or alternative to x-ray diffraction. *J. Sediment. Res*, *74*(5), 730–735,. doi: 10.1306/021304740730.

Pourbaix, M. (1974). *Atlas of Eletrochemical Equilibria in Aqueous Solutions* (1st ed., Vol. 2). Houston: National Association of Corrosion Engineers. doi: 1

Pullaiah, G., Irving, E., Buchan, K., & Dunlop, D. (1975). Magnetization changes caused by burial and uplift. *Earth Planet. Sci. Lett*, *28*(1), 133–143,. doi: 10.1177/001139217502300101.

Ravel, B. (2013). Xas-education, examples, fes2. In *Transmission scan of fes2.* Retrieved from `https://github.com/bruceravel/XAS-Education/blob/06b144d1a3418c3f1ddec2454167d62f58f1f256/Examples/FeS2/fes2_rt01_mar02.xmu` (accessed Oct. 10, 2022).)

Ravel, B., & Newville, M. (2005). Athena , artemis , hephaestus : data analysis for x-ray absorption spectroscopy using ifeffit. *J. Synchrotron Radiat*, *12*(4), 537–541,. doi: 10.1107/S0909049505012719.

Riccomini, C., Nogueira, A., & Sial, A. (2007). Carbon and oxygen isotope ge ochemistry of ediacaran outer platform carbonates, paraguay belt, central brazil. *An. Acad. Bras. Cienc*, *79*(3), 519–527,. doi: 10.1590/s0001-37652007000300012.

Rickard, D. (1995). Kinetics of fes precipitation: Part 1. competing reaction mechanisms. *Geochimica et Cosmochimica Acta*, *59*(21), 4367-4379. Retrieved from `https://www.sciencedirect.com/science/article/pii/001670379500251T` doi: https://doi.org/10.1016/0016-7037(95)00251-T

Rickard, D., & Luther, G. (2007). Chemistry of iron sulfides. *Chem. Rev*, *107*(2), 514–562,. doi: 10.1021/cr0503658.

Roberts, A. (2011). Magnetotactic bacterial abundance in pelagic marine environments is limited by organic carbon flux and availability of dissolved iron. *Earth Planet. Sci. Lett*, *310*(3–4), 441–452,. doi: 10.1016/j.epsl.2011.08.011.

Roberts, A. (2015). Magnetic mineral diagenesis. *Earth-Science Reviews*, *151*, 1–47. Retrieved from `http://dx.doi.org/10.1016/j.earscirev.2015.09.010` doi: 10.1016/j.earscirev.2015.09.010

Roberts, A. (2022). Unlocking information about fine magnetic particle assemblages from first-order reversal curve diagrams: Recent advances. *Earth-Science Rev*, *227*(January), 103950,. (p.) doi: 10.1016/j.earscirev.2022.103950.

Roberts, A., Florindo, F., Chang, L., Heslop, D., Jovane, L., & Larrasoaña, J. (2013). Magnetic properties of pelagic marine carbonates. *Earth-Science Rev*, *127*, 111–139,. doi: 10.1016/j.earscirev.2013.09.009.

Roberts, A., Heslop, D., Zhao, X., & Pike, C. (2014). Understanding fine magnetic particle systems through use of first-order reversal curve diagrams. *Rev. Geophys*, *52*(4), 557–602,. doi: 10.1002/2014RG000462.

Roberts, A., Pike, C., & Verosub, K. (2000). First-order reversal curve diagrams: A new tool for characterizing the magnetic properties of natural samples. *J. Geophys. Res. Solid Earth*, *105*(B12), 28461–28475,. doi: 10.1029/2000jb900326.

Rochette, P., Ménard, G., & Dunn, R. (1992, 02). Thermochronometry and cooling rates deduced from single sample records of successive magnetic polarities during uplift of metamorphic rocks in the Alps (France). *Geophysical Journal International*, *108*(2), 491-501. Retrieved from `https://doi.org/10.1111/j.1365-246X.1992.tb04630.x` doi: 10.1111/j.1365-246X.1992.tb04630.x

Rodrigues, J. (2008). *Proveniência de sedimentos dos grupos canastra, ibiá, vazante e bambuí - um estudo de zircões detríticos e idades modelo sm-nd.* Universidade de Brasília.

Sacek, V. (2014). Drainage reversal of the amazon river due to the coupling of surface and lithospheric processes. *Earth Planet. Sci. Lett*, *401*, 301–312,. doi: 10.1016/j.epsl.2014.06.022.

Santana, A., Chemale, F., Scherer, C., Guadagnin, F., Pereira, C., & Santos, J. (2021). Paleogeographic constraints on source area and depositional systems in the neoproterozoic irecê basin, são francisco craton. *J. South Am. Earth Sci*, *109*(February 2020). doi: 10.1016/j.jsames.2021.103330.

Schreiner, W. (2002). Paramagnetic anisotropy of a natural kaolinite and its modification by chemical reduction. *J. Magn. Magn. Mater*, *241*(2–3), 422–429,. doi: 10.1016/S0304-8853(01)00480-2.

Shi, Q., & Wu, J. (2021). Review on sulfur compounds in petroleum and its products: State-of-the-art and perspectives. *Energy & Fuels*, *35*(18), 14445–14461,. doi: 10.1021/acs.energyfuels.1c02229.

Shulman, G., Yafet, Y., Eisenberger, P., & Blumberg, W. (1976). Observations and interpretation of x-ray absorption edges in iron compounds and proteins. *Proc. Natl. Acad. Sci. U. S. A*, *73*(5), 1384–1388,. doi: 10.1073/pnas.73.5.138.

Stacey, F., & Banerjee, S. K. (1974). *The Physical Principles of Rock Magnetism.* Elsevier. Retrieved from `https://linkinghub.elsevier.com/retrieve/pii/001282527490110X`

Stamatakos, J., Hirt, A., & Lowrie, W. (1996). The age and timing of folding in the central appalachians from paleomagnetic results. *GSA Bulletin*, *108*, 815–829.

Strehlau, J., Hegner, L., Strauss, B., Feinberg, J., & Penn, R. (2014). Simple and efficient separation of magnetic minerals from speleothems and other carbonates. *J. Sediment.*

Res, *84* (11), 1096–1106,. doi: 10.2110/jsr.2014.89.

Szczerba, M., Kłapyta, Z., & Kalinichev, A. (2014). Ethylene glycol intercalation in smectites. molecular dynamics simulation studies. *Appl. Clay Sci*, *91–92*, 87–97,. doi: 10.1016/j.clay.2014.02.014.

Sánchez-Bettucci, L., & Rapalini, A. (2002). Paleomagnetism of the sierra de las animas complex, southern uruguay: its implications in the assembly of western gondwana. *Precambrian Res*, *118* (3–4), 243–265,. doi: 10.1016/S0301-9268(02)00114-6.

Tauxe, L., Banerjee, S., Butler, R., & van der Voo, R. (2018). *Essentials of paleomagnetism: Third web edition.* UC Press. Retrieved from `https://earthref.org/MagIC/books/Tauxe/Essentials/`

Tauxe, L., Mullender, T., & Pick, T. (1996). Potbellies, wasp-waists, and superparamagnetism in magnetic hysteresis. *J. Geophys. Res. Solid Earth*, *101* (B1), 571–583,. Retrieved from `https://doi.org/10.1029/95JB03041.` doi: 10.1029/95JB03041.

Tedeschi, M. (2016). The ediacaran rio doce magmatic arc revisited (araçuaí-ribeira orogenic system, se brazil. *J. South Am. Earth Sci*, *68*, 167–186,. Retrieved from `https://doi.org/10.1016/j.jsames.2015.11.011.` doi: 10.1016/j.jsames.2015.11.011.

Temporim, F., Bellon, U., Domeier, M., Trindade, R., & Agrella-filho, M. (2021). Constraining the cambrian drift of gondwana with new paleomagnetic data from post-collisional plutons of the araçuaí orogen, se brazil. *Precambrian Res*, *359* (December 2020), 106212,. (p.) doi: 10.1016/j.precamres.2021.106212.

Tohver, E., D'Agrella-Filho, M., & Trindade, R. (2006). Paleomagnetic record of africa and south america for the 1200-500 ma interval, and evaluation of rodinia and gondwana assemblies. *Precambrian Res*, *147* (3–4), 193–222,. doi: 10.1016/j.precamres.2006.01.015.

Tohver, E., Trindade, R., Solum, J., Hall, C., Riccomini, C., & Nogueira, A. (2010). Closing the clymene ocean and bending a brasiliano belt: Evidence for the cambrian formation of gondwana, southeast amazon craton. *Geology*, *38* (3), 267–270,. doi: 10.1130/G30510.1.

Tohver, E., Weil, A., Solum, J., & Hall, C. (2008). Direct dating of carbonate remagnetization by 40ar/39ar analysis of the smectite – illite transformation. *Earth Planet. Sci. Lett*, *274*, 524–530,. doi: 10.1016/j.epsl.2008.08.002.

Tolentino, H. (2017). CarnaÚba: The coherent x-ray nanoprobe beamline for the brazilian synchrotron sirius/lnls. *J. Phys. Conf. Ser*, *849*, 012057,. doi: 10.1088/1742-6596/849/1/012057.

Tolentino, H. (2021). X-ray microscopy developments at sirius-lnls: first commissioning experiments at the carnauba beamline. In *X-ray nanoimaging: Instruments and methods v* (p. 6,). doi: 10.1117/12.2596496.

Torsvik, T. (2012). Phanerozoic polar wander, palaeogeography and dynamics. *Earth-Science Rev*, *114* (3–4), 325–368,. doi: 10.1016/j.earscirev.2012.06.007.

Torsvik, T., & Cocks, L. (2013). Gondwana from top to base in space and time. *Gondwana Res*, *24* (3–4), 999–1030,. doi: 10.1016/j.gr.2013.06.012.

Trindade, R., D'Agrella-Filho, M., Babinski, M., Font, E., & Brito, B. (2004). Paleomagnetism and geochronology of the bebedouro cap carbonate : evidence for continental-scale cambrian remagnetization in the são francisco craton , brazil. *Precambrian Res*, *128*, 83–103,. doi: 10.1016/j.precamres.2003.08.010.

Trindade, R., Font, E., D'Agrella-Filho, M., Nogueira, A., & Riccomini, C. (2003). Low-latitude and multiple geomagnetic reversals in the neoproterozoic puga cap carbonate, amazon craton. *Terra Nov*, *15* (6), 441–446,. doi: 10.1046/j.1365-3121.2003.00510.x.

Trindade, R., & Macouin, M. (2007, mar). Palaeolatitude of glacial deposits and palaeogeography of Neoproterozoic ice ages. *Comptes Rendus Geoscience*, *339* (3-4), 200–211. Retrieved from `https://www.sciencedirect.com/science/article/pii/S1631071307000338https://linkinghub.elsevier.com/retrieve/pii/S1631071307000338` doi: 10.1016/j.crte.2007.02.006

Tucker, M. (2001). *Sedimentary petrology. an introduction to the orgin of sedimentary rocks.* Blackwell Science Ltd.

Vauchez, A., Hollanda, M., Monié, P., Mondou, M., & Egydio-Silva, M. (2019). Slow cooling and crystallization of the roots of the neoproterozoic araçuaí hot orogen (se brazil): Implications for rheology, strain distribution, and deformation analysis. *Tectonophysics*, *766*(October), 500–518,. doi: 10.1016/j.tecto.2019.05.013.

Wang, Y. (2022). Micromagnetic modeling of a magnetically unstable zone and its geological significances. *J. Geophys. Res. Solid Earth*, *127*(9), 1–14,. doi: 10.1029/2022JB024876 .

Wiedemann, C., Medeiros, S., Ludka, I., Mendes, J., & Costa-de Moura, J. (2002). Architecture of late orogenic plutons in the araçuaí-ribeira fold belt, southeast brazil. *Gondwana Res*, *5*(2), 381–399,. doi: 10.1016/S1342-937X(05)70730-9.

Wohlfarth, E., & Tonge, D. (1957). The remanent magnetization of single domain ferromagnetic particles. *Philos. Mag*, *2*(23), 1333–1344,. doi: 10.1080/14786435708243210.

Woods, S. D., Elmore, R. D., & Engel, M. H. (2002). Paleomagnetic dating of the smectite-to-illite conversion: Testing the hypothesis in jurassic sedimentary rocks, skye, scotland. *Journal of Geophysical Research: Solid Earth*, *107*(B5), EPM 2-1-EPM 2-10. Retrieved from https://agupubs.onlinelibrary.wiley.com/doi/abs/10.1029/2000JB000053 doi: https://doi.org/10.1029/2000JB000053

Xu, Y., Tan, X., Li, S., Li, Y., Ran, B., Han, Y., ... Ma, Z. (2022). Paleomagnetism of the greater indian passive margin sediments from the upper cretaceous succession: Evidence for long-delayed remagnetizations and implication for the india-asia collision. *Journal of Asian Earth Sciences*, *229*, 105165. Retrieved from https://doi.org/10.1016/j.jseaes.2022.105165 doi: 10.1016/j.jseaes.2022.105165

Yamashita, H. (2003). Xafs analysis and applications to carbons and catalysts. In *Carbon alloys: Novel concepts to develop carbon science and technology* (p. 189–209). Elsevier Ltd.

Zhao, H., Cao, Y., Sit, S., Lineberry, Q., & Pan, W. (2012). Thermal characteristics of bitumen pyrolysis. *J. Therm. Anal. Calorim*, *107*(2), 541–547,. doi: 10.1007/s10973-011-1590-x.

Zhu, J., Zeng, Z., & Li, W. (2021). K-edge xanes investigation of fe-based oxides by density functional theory calculations. *J. Phys. Chem. C*, *125*(47), 26229–26239,. doi: 10.1021/acs.jpcc.1c08461.

Zumaquero, E., Gilabert, J., Díaz-Canales, E., Gazulla, M., & Gómez-Tena, M. (2021). Study on sulfide oxidation in a clay matrix by the hyphenated method. *Minerals*, *11*(10), 1121,. doi: 10.3390/min11101121.

Zunino, F., & Scrivener, K. (2022). Oxidation of pyrite (fes2) and troilite (fes) impurities in kaolinitic clays after calcination. *Mater. Struct*, *55*(1), 9,. doi: 10.1617/s11527-021-01858-9.